Royal Netherlands
Meteorological Institute
Ministry of Infrastructure
and Water Management

TROPOMI ATBD of the Aerosol Layer Height

TROPOMI

sentinel-5p

document number	:	S5P-KNMI-L2-0006-RP
authors	:	M. de Graaf, J.F. de Haan, A.F.J. Sanders and M. Sneep
CI identification	:	CI-7430-ATBD_Aerosol_Layer_Height
issue	:	2.6.0
date	:	2023-10-20
status	:	In preparation

Document approval record

	digital signature
Prepared:	
Checked:	
Approved PM:	
Approved PI:	

Document change record

issue	date	item	comments
0.0.1	2012-09-10	All	Initial version.
0.0.2	2012-09-25	All	Updated with feed from KNMI Level-2 team.
0.1.0	2012-09-27	-	Released for first review by Level-2 Working Group.
0.1.1	2012-11-16	All	Updated with feedback from aerosol science verification team. Document number changed from S5P-KNMI-L2-0115-RP to S5P-KNMI-L2-0006-RP.
0.2.0	2012-11-16	-	Released for first review by ESA.
0.2.1	2013-06-04	All	Section Absorbing Aerosol Index moved to separate ATBD (S5P-KNMI-L2-0008-RP). Added error analysis. Completed and revised other sections.
0.3.0	2013-06-04	-	Released for Level-2 Working Group.
0.3.1	2013-06-21	All 10	Updated with feedback from aerosol science verification team (no major changes). Added application to GOSAT spectra (Section 10).
0.5.0	2013-06-21	-	Released for external science review.
0.5.1	2013-11-29	 6.4.1 9.9	Updated with feedback from external science reviewers. Clarified text on ignoring polarization in Section 6.4.1. Added paragraph on fluorescence to Section 8.9. Minor other clarifications throughout the text.
0.9.0	2013-11-29	-	Released for external science review.
0.9.1	2014-04-15	4 10 4.7,11	Section Instrument (Section 4) moved to separate ATBD (S5P-KNMI-L2-0010-RP). Revised and completed Section 10; section renamed to Application to GOME-2 spectra. Updated Section 4.7 and Section 11.
0.10.0	2014-04-15	-	Released for Critical Design Review.
0.10.1	2014-09-30	7 5.3.3	Revised Section 7 Added paragraph to Section 5.3.3. Several minor clarifications throughout the text.
0.11.0	2014-09-30	-	Released for review by ESA.
0.11.1	2015-09-04	7 6.2,7.3.3	Updated pixel selection with description of VIIRS cloud mask. Added remark on alternative surface albedo climatologies. Several minor changes throughout the text.
0.13.0	2015-09-04	-	Limited release to S5P Validation Team.
0.13.1	2016-01-29	4.2,4.5-6, 5.3,5.5, 6.2 11	Updated sections on algorithm heritage, algorithm overview, development risks, the atmospheric model, the instrument model and the state vector composition. Main changes: surface albedo removed from state vector, reduction of fit window to 758–762 nm, interpretation of Aerosol Layer Height parameter, other conclusions from recent GOME-2 and SCIAMACHY case studies included in the ATBD. Updated conclusion and outlook. Several minor changes throughout the text.

issue	date	item	comments
1.0.0	2016-01-29	-	Public release.
1.0.1	2019-06-24	5	Update forward model with neural network estimate of O_2 A band reflectances. First validation and verifcation.
1.1.0	2019-09-30	-	Public release.
1.1.1	2020-12-11	5.1.1 5.1.5 7.3	Update of VIIRS CF definition Redefined pixel selection criteria. Update of timeliness including VCM Several minor clarifications throughout the text.
2.0.0	2020-06-24	4 9	Minor updates Removed obsolete
2.2.0	2021-07-05	-	Public release
2.4.0	2022-04-08	5.2.4.4 5.3.2 6.3.2	Update of the surface reflectance to S5P DLER
2.6.0	2023-10-20	all 4.5	Introduction of surface fitting Removed numerous obsolete and duplicate information

Contents

List of Tables

List of Figures

1 Introduction

1.1 Identification

This document, identified as S5P-KNMI-L2-0006-RP, is the Algorithm Theoretical Basis Document (ATBD) for the Tropospheric Monitoring Instrument's (TROPOMI) Aerosol Layer Height (ALH) product. It is part of a series of ATBDs describing the TROPOMI Level-2 products.

1.2 Purpose and objective

The purpose of this document is to describe the current implementation and the theoretical basis of the Aerosol Layer Height algorithm. The document is maintained during the development phase and the lifetime of the data product. Updates and new versions are foreseen if there are changes to the algorithm.

1.3 Document overview

Section 2 lists applicable and reference documents within the Sentinel-5 Precursor (S5P) / TROPOMI project as well as electronic references. Section 3 gives a list of terms, abbreviations and symbols that are specific for this document. Section 4, section 5 and section 5.3 describe the forward model and retrieval method, respectively. Section 6 discusses the operational algorithm's feasibility. Section 7 provides an extensive error analysis. Section 8 presents a validation plan for the Aerosol Layer Height product. Section 9 provides a general conclusion and outlook. Finally, Section 12 lists references to peer-reviewed papers and other scientific publications.

1.4 Acknowledgements

The authors would like to thank the following persons for useful discussions: Maarten Sneep, Gijs Tilstra, Ofelia Vieitez, Piet Stammes, Arnoud Apituley and Pepijn Veefkind.

2 Applicable and reference documents

2.1 Applicable documents

[AD1] OMI Geolocation Review.
source: KNMI; **ref:** TN-OMIE-KNMI-729; **issue:** 1.0; **date:** 2004-04-05.

[AD2] Science Requirements Document for TROPOMI. Volume I: Mission and Science Objectives and Observational Requirements.
source: KNMI, SRON; **ref:** RS-TROPOMI-KNMI-017; **issue:** 2.0.0; **date:** 2008-10-30.

2.2 Reference documents

[RD1] Terms, definitions and abbreviations for TROPOMI L01b data processor.
source: KNMI; **ref:** S5P-KNMI-L01B-0004-LI; **issue:** 3.0.0; **date:** 2013-11-08.

[RD2] Terms and symbols in the TROPOMI Algorithm Team.
source: KNMI; **ref:** S5P-KNMI-L2-0049-MA; **issue:** 1.0.0; **date:** 2015-07-16.

[RD3] S5P/TROPOMI Science Verification Report.
source: IUP; **ref:** S5P-IUP-L2-ScVR-RP; **issue:** 2.1; **date:** 2015-12-22.

[RD4] TROPOMI Instrument and Performance Overview.
source: KNMI; **ref:** S5P-KNMI-L2-0010-RP; **issue:** 0.10.0; **date:** 2014-03-15.

[RD5] S5P-NPP Cloud Processor ATBD.
source: RAL Space; **ref:** S5P-NPPC-RAL-ATBD-0001; **issue:** 1.0.0; **date:** 2016-02-12.

[RD6] DISAMAR: Determining Instrument Specifications and Analyzing Methods for Atmospheric Retrieval, User Manual.
source: KNMI; **ref:** RP-TROPOMI-KNMI-104; **issue:** -; **date:** 2012-02-08.

[RD7] DISAMAR. Determining Instrument Specifications and Analyzing Methods for Atmospheric Retrieval. Algorithm description and background information.
source: KNMI; **ref:** RP-TROPOMI-KNMI-066; **issue:** 2.2.1; **date:** 2011-05-19.

[RD8] Calibration analysis report for TROPOMI UVN instrument spectral response function.
source: KNMI; **ref:** S5P-KNMI-OCAL-0124-RP; **issue:** 0.1.0; **date:** 2015-10-01.

[RD9] DISAMAR: Determining Instrument Specifications and Analyzing Methods for Atmospheric Retrieval, Algorithms and background.
source: KNMI; **ref:** RP-TROPOMI-KNMI-066; **issue:** -; **date:** 2012-01-24.

[RD10] DISAMAR: Determining Instrument Specifications and Analyzing Methods for Atmospheric Retrieval, Line Mixing and Collision Induced Absorption for the O2 A-band.
source: KNMI; **ref:** RP-TROPOMI-KNMI-???; **issue:** -; **date:** 2012-01-24.

[RD11] D. P. Dee, S. M. Uppala, A. J. Simmons *et al.*; The ERA-Interim reanalysis: configuration and performance of the data assimilation system. *Quarterly Journal of the Royal Meteorological Society*; **137** (2011) (656), 553; 10.1002/qj.828. URL https://rmets.onlinelibrary.wiley.com/doi/abs/10.1002/qj.828.

[RD12] K. Chance and R.L. Kurucz; An improved high-resolution solar reference spectrum for earth's atmosphere measurements in the ultraviolet, visible, and near infrared. *Journal of Quantitative Spectroscopy and Radiative Transfer*; **111** (2010) (9), 1289; 10.1016/j.jqsrt.2010.01.036.

[RD13] Wavelength calibration for S5P L2 data processors.
source: KNMI; **ref:** S5P-KNMI-L2-0126-TN; **issue:** 1.0.0; **date:** 2015-09-11.

[RD14] TROPOMI ATBD of the directionally dependent surface Lambertian-equivalent reflectivity.
source: KNMI; **ref:** S5P-KNMI-L3-0301-RP; **issue:** 1.2.0; **date:** 2004-04-05.

[RD15] Preparing elevation data for Sentinel 5 precursor.
source: KNMI; **ref:** S5P-KNMI-L2-0121-TN; **issue:** 2.0.0; **date:** 2015-09-11.

[RD16] Sentinel-5 precursor/TROPOMI Level 2 Product User Manual Aerosol Layer Height.
source: KNMI; **ref:** S5P-KNMI-L2-0022-MA; **issue:** 2.6.0; **date:** 2023-09-26.

[RD17] Algorithm theoretical basis document for the TROPOMI L01b data processor.
source: KNMI; **ref:** S5P-KNMI-L01B-0009-SD; **issue:** 6.0.0; **date:** 2015-09-22.

[RD18] Quarterly Validation Report of the Copernicus Sentinel-5 Precursor Operational Data Products #20: April 2018 – August 2023.
source: MPC; **ref:** S5P-MPC-IASB-ROCVR-13.01.00-20211217; **issue:** 20.00.01; **date:** 2023-08-18.

[RD19] URL https://mpc-vdaf.tropomi.eu.

2.3 Electronic references

[ER1] URL http://www.cfa.harvard.edu/hitran/.

[ER2] URL https://www.tensorflow.org.

[ER3] URL http://www.esa-aerosol-cci.org.

3 Terms, definitions and abbreviated terms

Terms, abbreviations and symbols that are used within the TROPOMI Level-2 project are described in [RD1]. and [RD2]. Terms, definitions and abbreviated terms that are specific for this document can be found below. More in [AD1]

3.1 Terms and definitions

accuracy	systematic error component
height	vertical height, either in units of hPa (pressure) or in units of km (altitude)
hyperspectral imager	imager with large number of spectral channels, often at high spectral resolution (better than about 0.5-1 nm), e.g. GOME-2
multispectral imager	imager with a number of spectral channels (typically 30-50) that are generally not contiguous and have coarser spectral resolution (2-10 nm), e.g. MODIS

3.2 Acronyms and Abbreviations

UVAI	UV Aerosol Index
AERONET	Aerosol Robotic Network
AEROPRO	Aerosol Profile Retrieval Concept Development and Validation for Sentinel-4
ALH	Aerosol Layer Height
ATBD	Algorithm Theoretical Basis Document
AVHRR	Advanced Very High Resolution Radiometer
CALIOP	Cloud-Aerosol Lidar with Orthogonal Polarisation
CALIPSO	Cloud-Aerosol Lidar and Infrared Pathfinder Satellite Observation
CIA	collision-induced absorption
CPU	central processing unit
DISAMAR	Determining Instrument Specifications and Analyzing Methods for Atmospheric Retrieval
DLR	Deutsches Zentrum für Luft- und Raumfahrt
DLER	Directional Lambertian-equivalent reflectivity
DWD	Deutscher Wetterdienst
EarthCARE	Earth Clouds, Aerosols and Radiation Explorer
ECMWF	European Centre for Medium-Range Weather Forecasts
EARLINET	European Aerosol Research Lidar Network
ERA	ECMWF Reanalysis
FRESCO	Fast Retrieval Scheme for Clouds from the Oxygen A Band
FWHM	full width at half maximum
GALION	GAW Atmospheric Lidar Observation Network
GMES	Global Monitoring of the Environment and Security
GOME	Global Ozone Monitoring Experiment
HG	Henyey-Greenstein
HITRAN	High Resolution Transmission
HSRL	High Spectral Resolution Lidar
IASI	Infrared Atmospheric Sounding Interferometer
IUP	Institut für Umweltphysik
JPL	Jet Propulsion Laboratory
KNMI	Koninklijk Nederlands Meteorologisch Instituut

LABOS	layer-based orders of scattering
LBL	Line-by-line
LER	Lambertian-equivalent reflectivity
LM	line mixing
MERIS	Medium Resolution Imaging Spectrometer
MetOp	Meteorological Operational Satellite
MISR	Multi-Angle Imaging Spectroradiometer
MLS	mid-latitude summer
MODIS	Moderate Resolution Imaging Spectroradiometer
MTG-S	Meteosat Third Generation - Sounder
NIR	near infrared
NN	neural network
NSIDC	National Snow & Ice Data Center
OMI	Ozone Monitoring Instrument
PMD	Polarisation Measurement Devices
POLDER	Polarization and Directionality of the Earth's Reflectance
RAA	relative azimuth angle
S5P	Sentinel-5 Precursor
SACURA	Semi-Analytical Cloud Retrieval Algorithm
SCIAMACHY	Scanning Imaging Absorption Spectrometer for Atmospheric Cartography
SNR	signal-to-noise ratio
Suomi-NPP	Suomi National Polar-orbiting Partnership
SWIR	shortwave infrared
SZA	solar zenith angle
TROPOMI	Tropospheric Monitoring Instrument
UV	ultraviolet
UVIS	ultraviolet-visible
UVN	ultraviolet-visible-near infrared
VCM	VIIRS cloud mask
VIIRS	Visible / Infrared Imaging Radiometer Suite
VIS	visible
VZA	viewing zenith angle

3.3 Symbols

ω_0	single scattering albedo [-]
τ_0	aerosol or cloud optical thickness [-]
α	Ångström coefficient [-]
g	asymmetry parameter [-]
p_{mid}	aerosol mid pressure [hPa]
z_{mid}	aerosol mid altitde [km]
p_{top}	aerosol top pressure [hPa]
Δp	pressure thickness [hPa]
p_{s}	surface pressure [hPa]
z_{s}	surface altitude (above reference surface) [km]
A_{s}	surface albedo [-]
F_{s}	surface (fluorescence) emission [ph. cm^{-2} s^{-1} nm^{-1} sr^{-1}]

R	Reflectance [sr^{-1}]
I	Radiance [ph. cm^{-2} s^{-1} nm^{-1} sr^{-1}]
E_0	Irradiance [ph. cm^{-2} s^{-1} nm^{-1}]

4 Introduction to Aerosol Layer Height product

4.1 Product description

The Tropospheric Monitoring Instrument features a new aerosol product that is dedicated to retrieval of the height of tropospheric aerosols. Before the launch of TROPOMI, daily global observations of aerosol height were not available on an operational basis. Aerosol profiles were provided by active sensors, particularly by ground-based lidar systems or by the space-borne Cloud-Aerosol Lidar with Orthogonal Polarisation (CALIOP), and aerosol layer height by multi-angle sensors, most notably Multi-Angle Imaging SpectrRadiometer (MISR). Active sensors have a high vertical resolution, but CALIOP and MISR observe in narrow tracks only. However, passive sensors, such as TROPOMI, can cover the entire earth in a single day.

The TROPOMI Aerosol Layer Height product focuses on retrieval of vertically localized aerosol layers in the troposphere, such as sea salt, industrial pollution and absorbing aerosols such as desert dust, biomass burning aerosol and volcanic ash plumes. The height of such layers is retrieved for cloud-free conditions. Height information for aerosols in the free troposphere is particularly important for aviation safety. Scientific applications include radiative forcing studies, long-range transport modeling and studies of cloud formation processes. Aerosol height information also helps to interpret the UV Aerosol Index (UVAI) in terms of aerosol absorption as the index is strongly height-dependent.

Retrieval of aerosol height is based on absorption by oxygen in the A band. The O_2 A band is located in the near-infrared wavelength range between about 759 and 770 nm. It is a highly structured line absorption spectrum with strongest absorption lines occurring between 760 and 761 nm. The absorption band spans a wide range of absorption optical thicknesses. At some wavelengths, photons do not reach the lower levels of the atmosphere.

Figure 1 shows simulated reflectance spectra at TROPOMI's anticipated instrument specifications (as

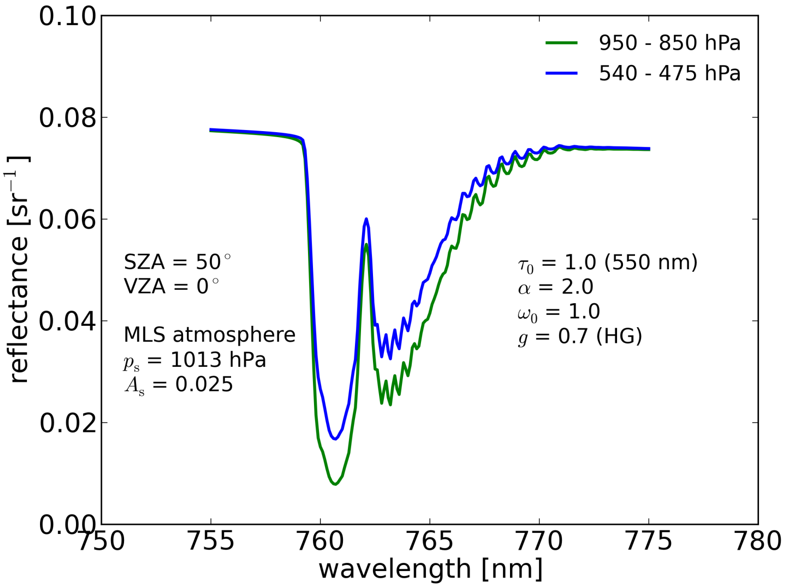

Figure 1: Simulated reflectance spectra of the O_2 A band at a spectral resolution (FWHM) of 0.5 nm for a scene containing a representative aerosol layer. The aerosol layer is between 950 and 850 hPa (green line) or between 540 and 475 hPa (blue line). The 1-σ measurement errors on reflectance are smaller than the width of the plotting lines: anticipated signal-to-noise ratios for these spectra (based on [59]) are about 645 in the continuum and 302 and 207 in the deepest part of the O_2 A band assuming pure shot noise. The solar zenith angle is 25° and the viewing direction is nadir. The aerosol optical thickness τ_0 at 550 nm is 1.0, the Ångström coefficient α is 2.0, the single scattering albedo is 1.0, and the phase function is a Henyey-Greenstein function with asymmetry parameter g of 0.7. Spectra were simulated with a temperature profile corresponding to the mid-latitude summer (MLS) atmosphere, a surface pressure of 1013 hPa and a constant ground surface albedo of 0.025.

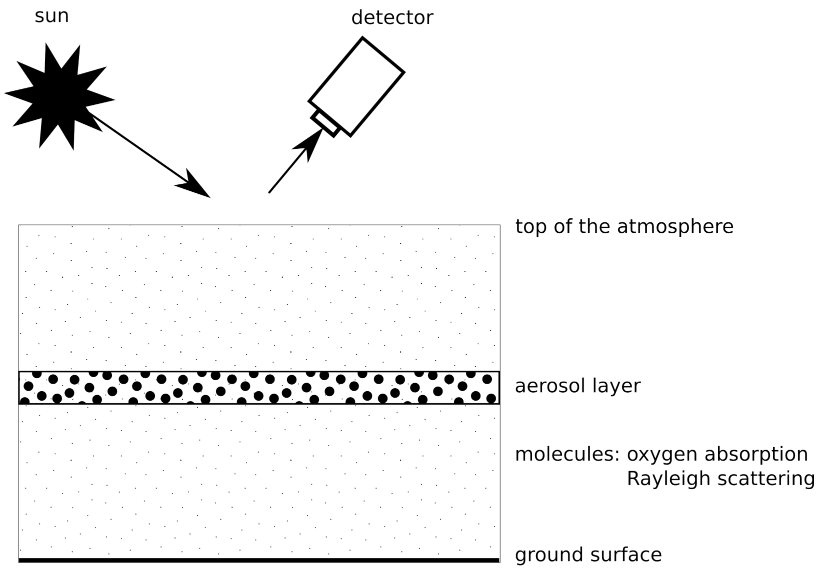

Figure 2: Schematic depiction of the atmosphere and typical TROPOMI satellite configuration for retrieval of Aerosol Layer Height. The Rayleigh scattering optical thickness at the O_2 A band is ~0.02
.

described in [59]) for an aerosol layer at two different pressures. The difference between the two spectra provides the aerosol pressure signal. The baseline fit window for the Aerosol Layer Height algorithm extends from 758 nm (continuum) to 770 nm. For more recent TROPOMI instrument specifications, see . A schematic depiction of the satellite configuration for observations of the O_2 A band with TROPOMI is given in Figure 2.

4.2 Heritage

Aerosol Layer Height is the latest addition of operational Level-2 products for TROPOMI, first released in 2019. Heritage products for an operational aerosol profile retrieval based on hyperspectral measurements of the oxygen A band do not exist. However, a new effective aerosol layer height product has been released from the Korean Geostationary Environment Monitoring Spectrometer (GEMS), launched in 2020 [38], providing temporal information (at one hour resolution) of aerosol layer height over Asia for the first time. Furthermore, ALH has been experimentally retrieved from the Sentinel-3/OLCI instrument for two cases [24].

The Aerosol Layer Height algorithm can be applied to measurement series from the Scanning Imaging Absorption Spectrometer for Atmospheric Cartography (SCIAMACHY; [3]) and the Global Ozone Monitoring Experiment-2 (GOME-2). A first case study of ALH retrieval with GOME-2 measurements has been published as [45]. Aerosol Layer Height retrievals were performed for a number of aerosol scenes covering various aerosol types, both elevated and boundary layer aerosols and land and sea surfaces. The retrieval results were evaluated with lidar measurements. A follow-up study applied the TROPOMI ALH algorithm to desert dust outbreaks off the West African coast observed with SCIAMACHY. Within the TROPOMI project also a scientific verification study of the prototype algorithm has been performed. An independent ALH verification algorithm from the Institute of Environmental Physics (IUP, Bremen, Germany) and the prototype ALH algorithm from KNMI were applied to the case of a volcanic ash plume near Iceland observed with GOME-2 (chapter 14 in [RD3]). Retrieval results were intercompared and evaluated with plume heights retrieved with MISR (stereoscopic retrieval). The main conclusions from these studies have been included in this ATBD as much as possible. TROPOMI Aerosol Layer Height algorithm will serve as the ALH heritage algorithm for the future Sentinel–4 and Sentinel–5 missions [23], which make hyperspectral observations of the O_2 A band as well.

Early papers investigating the O_2 A band for aerosol retrieval are by Badayev and Malkevich (1978)[2] and Gabella et al. (1999) [2] and [16]. Corradini and Cervino (2006) [8] present a simulation study of retrieval of the extinction profile for SCIAMACHY instrument characteristics with all other parameters (e.g. aerosol and surface properties) being assumed in retrieval. Actual case studies exploiting hyperspectral O_2 A band measurements have been performed by Koppers and Murtagh (1997) [31] for GOME data, and by Kokhanovsky and Rozanov (2010) [30] and Sanghavi et al. (2012) [48] for SCIAMACHY data. Koppers and Murtagh (1997) retrieve surface albedo simultaneously with aerosol optical thickness and height distribution, while in the retrievals proposed by Kokhanovsky and Rozanov (2010) and Sanghavi et al. (2012) the surface albedo basically is a model parameter (i.e. surface albedo not fitted). A retrieval setup similar to Kokhanovsky and Rozanov (2010) is being extended to GOME-2 case studies [33]. Sensitivity studies to consolidate instrument requirements for O_2 A band aerosol retrieval include studies by Siddans et al. (2007) [49] and Hasekamp and Siddans (2009) [19] for Sentinel–4/5, and by Hollstein et al. (2012) [21] for the Earth Explorer 8 mission Fluorescence Explorer (FLEX). Dubuisson et al. (2009) [14] present a method to retrieve the altitude of aerosol plumes over ocean from the ratio of reflectances in the two O_2 A band channels of the Medium Resolution Imaging Spectrometer (MERIS) and the Polarization and Directionality of the Earth's Reflectance (POLDER) instrument. Finally, the work by Van Diedenhoven et al. (2005) [56] show that retrieved apparent surface pressure (i.e. retrieved surface pressure when ignoring aerosol scattering) with SCIAMACHY depends systematically on aerosol parameters. This illustrates in yet another way that the O_2 A band contains aerosol information available for retrieval.

Absorption by oxygen in the A band has been used in operational cloud retrieval for the GOME instruments (Fast Retrieval Scheme for Clouds from the Oxygen A Band (FRESCO) [28]) and for SCIAMACHY (Semi-Analytical Cloud Retrieval Algorithm (SACURA)[42]). There are indications that the FRESCO cloud retrieval algorithm may also provide information on aerosols in case of optically thick aerosol layers (Wang et al., 2012) [60]. However, FRESCO uses a Lambertian surface to model cloud layers, which may be an inaccurate approximation for aerosol layers since typical aerosol layers have significant transmission. The forward model of the Aerosol Layer Height algorithm is developed specifically for retrieval of aerosol height.

Finally, the O_2 A band is often used for an atmospheric scattering correction as part of more convolved trace gas retrieval algorithms (e.g. [37] [5]; [40]; [61]).

4.3 Product requirements

Science requirements for the Aerosol Layer Height product are described in [AD2]. The target requirement on the accuracy and precision of retrieved Aerosol Layer Height is 0.5 km or 50 hPa. The threshold requirement on accuracy and precision is 1 km or 100 hPa. A minimum aerosol optical thickness for which these requirements should be met is not specified. Note that an accuracy and precision requirement is defined for retrieved aerosol height but not for retrieved aerosol optical thickness.

Furthermore, the Aerosol Layer Height product will be delivered in near real-time, which means that Level-2 data should be available within three hours after observation.

4.4 Overview of the retrieval algorithm

The Aerosol Layer Height algorithm presently has the following key features:

- Spectral fit estimation of reflectance across the O_2 A band (wavelengths ~758–770 nm) using a neural network;
- Retrieval method based on Optimal Estimation;
- Main fit parameters: aerosol layer mid pressure (p_{mid}); aerosol optical thickness (τ_0); Surface albedo in continuum below and beyond the O_2 A band.
- Error estimates provided from the optimal estimation framework;
- Assumed aerosol profile: single uniform scattering layer with a fixed geometric thickness.

The aerosols are assumed to be confined to a single layer with a fixed geometric difference between top and bottom of the layer, and with a constant aerosol volume extinction coefficient and aerosol single scattering albedo within the layer. This parameterization is most suited for aerosol profiles that are dominated by a single, optically thick aerosol layer. The product's name explicitly refers to this particular profile parameterization. The reported height parameter is the mid pressure of the layer defined as the sum of top pressure and bottom pressure divided by two. The aerosol layer mid pressure (p_{mid}) is converted into an aerosol layer mid altitude (z_{mid}) using an appropriate temperature profile. In addition to aerosol layer mid pressure, aerosol optical thickness is reported for wavelengths of the O_2 A band (i.e. at 760 nm). The Aerosol Layer Height product contains error estimates as well as other relevant diagnostics so that the user can evaluate the retrieval result.

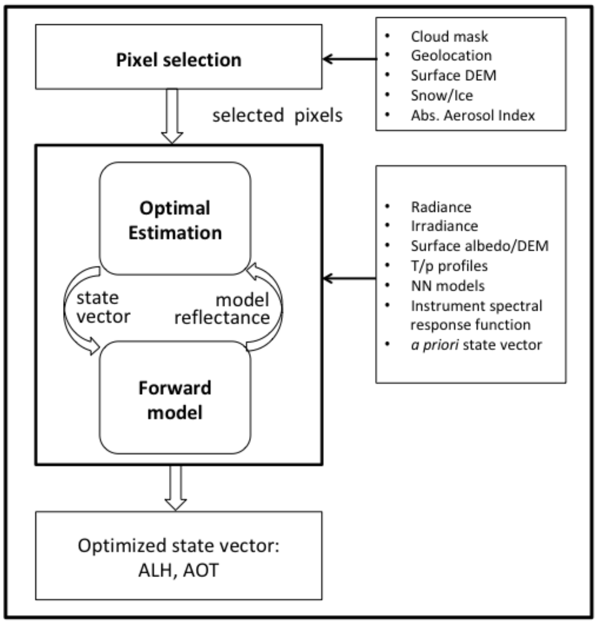

Figure 3: Flow chart for the Aerosol Layer Height retrieval algorithm.

A basic flow chart of the algorithm is given in Figure 3. Calibrated radiances, irradiances and their associated measurement errors are the main inputs for the algorithm. Cloud contaminated pixels are excluded first. Additionally, pixels covered by snow or (sea) ice or in the sunglint region are excluded from analysis as well. However, in order to process pixels that contain thick plumes of aerosols that may be mistaken for clouds, pixels are selected based on the UV Aerosol Index (UVAI). High UVAI values indicate elevated absorbing aerosol plumes, like desert dust plumes and smoke plumes, which are often screened by cloud filters. To avoid this, all pixels with a sufficiently high UVAI are included for processing. Dynamic input data further comprise meteorological data. Static input includes oxygen absorption parameters, a high-resolution solar irradiance spectrum, slit functions for the radiance and irradiance, and surface altitude (digital elevation model). Finally, a surface albedo climatology is used to provide *a priori* values for retrieval.

Aerosol optical properties show a large variation in time and space. However, the forward model used in the operational retrieval assumes a single, average aerosol model (e.g. single scattering albedo ω_0 of 0.95 and Henyey-Greenstein phase function with asymmetry parameter g of 0.7). Sensitivity analyses for the Aerosol Layer Height algorithm (Section 7) and experiments with GOME–2 spectra [46] have shown that a single, fixed aerosol model is sufficient for a reasonably accurate (i.e. compared to science requirements) retrieval of aerosol pressure, which is the primary objective of this product. The retrieved aerosol optical thickness holds for this aerosol model only and should be considered an effective quantity.

Development of the operational Aerosol Layer Height algorithm is ongoing work. In this document, the most recent implementation of the operational algorithm is described. Updates and new versions of the ATBD are foreseen during the lifetime of the product when there are significant changes to the algorithm. The current implementation of the algorithm is based on a neural network forward model and an optimal estimation scheme in the retrieval. A detailed description of the Aerosol Layer Height retrieval algorithm is given in Section 5.2 and Section 5.3. The sensitivity analyses presented in Section 7 illustrate the algorithm's expected performance and provide further support to the choices made in the design of the algorithm.

4.5 Updates

Versions 1.x of the AER_LH processor processed a limited set of pixels with absorbing aerosols only, using the UVAI product. The development of a very fast NN forward model allowed global, near-real time (NRTI) processing of the TROPOMI ALH product. Degradation of the UVAI product and the availability of an accurate VIIRS cloud mask (VCM), led to the development of a global AER_LH processor which processed all cloud-free scenes to also include scattering aerosols, active since version 2.2.0. The degradation of the UVAI signal prior to version 2.2.0 yielded an increasingly smaller number of selected pixels with absorbing aerosols. Although the degradation is corrected for in version 2.2.0, the selection by UVAI has been abandoned. In Figure 4 the

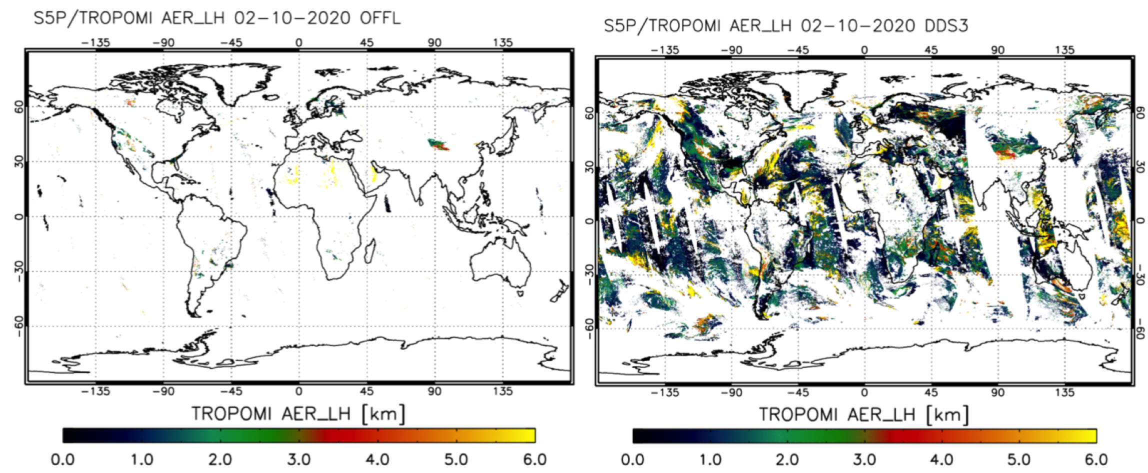

Figure 4: Difference in coverage due to the selection of only pixels with a UVAI index >1 (left panel) compared to all cloud-free pixels (right panel).

large change in pixel selection is shown between version 1.x (left) and version 2.x (right) data.

The VIIRS cloud mask is not available in NRTI, therefore the FRESCO cloud product is used in NRTI. In Figure 5 the change between the pixels masked by the NRTI cloud mask and the OFFL cloud mask is shown for an orbit on 21 Sept. 2019. See section 5.1.1 for details on the cloud masks. The higher number of pixels that need to be processed have a consequence on the timeliness of the processor, which is described in section 6.1.

In version 2.4.0 the surface albedo database changed from the initial GOME-2 LER database [53] to a surface albedo database determined from five years of TROPOMI minimum reflectance [52]. Furthermore, the fitted aerosol layer height changed from a fixed pressure difference to a fixed thickness in altitude to avoid very large geometrical thicknesses at higher altitudes.

The latest release 2.6.0. includes the fitting of the surface albedo values into the optimal estimation retrieval scheme. The previous versions have shown that over bright surfaces, the ALH is often biased low (towards the surface), which can be explained by the large contribution of the surface to the TOA signal. A recent test with synthetic test cases covering a large number of surface albedo values showed that including the surface albedo in the optimal estimation fit considerably improves the ALH in most cases, see Figure 15. Based on these results, the neural network was retrained to include the fitting of the surface albedo, which also means computing the Jacobians for the surface albedo.

In addition, a small but important change was the dependence on cloud mask information from SNPP/VIIRS in the offline (OFFL) data stream. The availability of VIIRS data is now checked on a pixel-by-pixel basis instead of per orbit, to avoid data losses due to partial available orbits that led to missing ALH in entire orbits

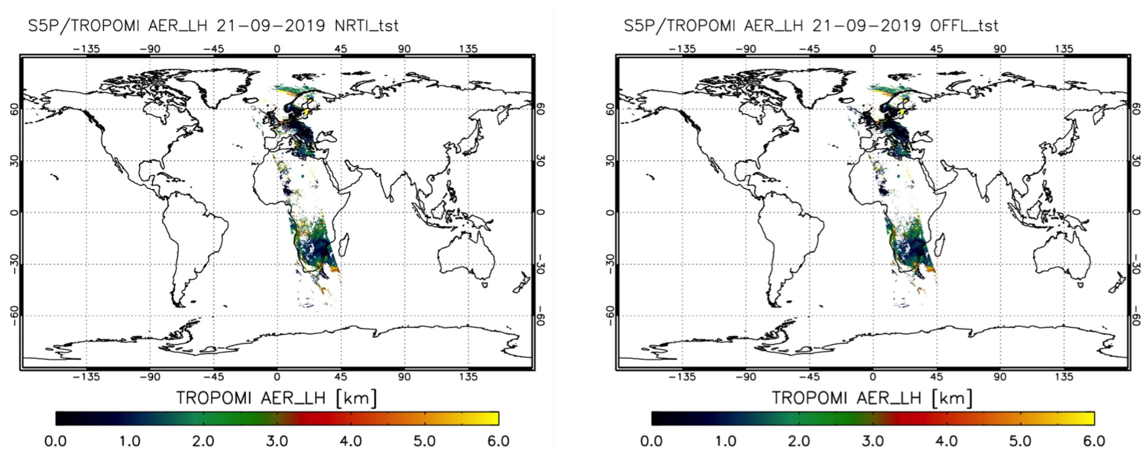

Figure 5: Difference in cloud masking between the NRTI processor (using FRESCO as a cloud mask) and the OFFL cloud processor (using VIIRS as a cloud mask).

before. The fallback in case of unavailable VIIRS cloud mask data remains FRESCO cloud mask in all cases.

4.6 Developments

Another way of improving the results over land would be to include the O_2 B band. Although the O_2 B band is weaker than the O_2 A band, this absorption band has a different and generally much weaker dependence on the surface albedo. Furthermore, co-registration errors are relatively small [RD4]. Good results from the combination of the O_2 B band and the O_2 A band were recently shown in [7]. However, inclusion of the O_2 B band in the operational algorithm is currently not foreseen.

The cloud screening is an important aspect of the ALH retrieval, since clouds have a strong impact on the results. The current OFFL cloud screening is based on the SNPP/VIIRS cloud maks, which has an excellent cloud detection algorithm, based on sophisticated detection methods and a high spatial resolution. However, the dependence on a satellite flying in formation with S5P, managed by a different agency and an instrument which is approaching the end of its lifetime, introduces risks which have recently led to data delay and may lead to data loss which should be avoided. Therefore, a cloud mask based on TROPOMI measurements aided with a VIIRS cloud mask-trained NN is considered to replace the current dynamic cloud mask from VIIRS.

4.7 Terminology

The deviation of a measured or calculated value from its true value is called the *error*. The error has a random and a systematic component. Throughout this document, a distinction is made between the *precision* and the *accuracy* of a retrieved parameter. These terms are defined as follows:

- Precision: This term refers to the random error component. A measure for the precision is the standard deviation (σ) of the fit parameter's (*a posteriori*) distribution. A large standard deviation indicates a poor precision.
- Accuracy: This term refers to the systematic error component. A measure for the accuracy is the bias defined as the fit parameter's (*a posteriori*) expected value minus its true value. A large bias indicates a poor accuracy.

Furthermore, within the context of the Optimal Estimation retrieval method, the terms *a priori error* and *a posteriori error* of a state vector element are often used. Both errors specifically refer to the random error component (1-σ error). The term *measurement noise* similarly refers to the random error component of the measurement error. The measurement error, however, may comprise other error terms as well, such as *calibration errors*.

The term *forward model* indicates the model that is used to calculate reflectance spectra. Its main use is in the retrieval procedure (inversion) in which modeled reflectance spectra are fitted to actual measurements. In this case, the forward model is called the *forward model for retrieval*. In the operational processor this step is comprised of a fast neural network estimation of the spectra. In the sensitivity studies in this ATBD, this step comprised of line-by-line calculation by DISAMAR, when actual measurements are replaced by simulated measurements. The forward model used for these simulations is called the *forward model for simulation*. We restrict the use of the term simulation to simulation of measurements or retrievals with DISAMAR when performing sensitivity analyses.

Finally, the effect of systematic errors on retrieval can be investigated by introducing differences between parameters in the forward model for simulation and the forward model for retrieval (*model biases*). Typically, the forward model for simulation is more complex and comprehensive than the forward model for retrieval. For example, the forward model for simulation may include a phase function from Mie calculations to describe the angular dependence of scattering by aerosols, whereas the forward model for retrieval always uses the neural network, trained with the same aerosol model.

5 Algorithm description

5.1 Spatial data selection

Aerosol Layer Height is retrieved for cloud-free pixels outside the sun glint region, not covered by snow and ice. To include thick plumes of aerosols possibly mistaken for clouds, all pixels with sufficiently high UV aerosol index are included in the analysis, regardless of their cloud amount, except for cirrus clouds.

5.1.1 Cloud mask

A cloud mask for the off-line processing and reprocessing modes is based on observations by VIIRS aboard Suomi-NPP [RD5]. VIIRS is a multispectral imager that is well suited for the detection of clouds, particularly of clouds at high altitude such as cirrus. S5P flies in formation with Suomi-NPP and observes within approximately 5 min from Suomi-NPP's overpass. Observations by VIIRS are re-gridded to the TROPOMI observation grid and a cloud mask is constructed for four different definitions of the TROPOMI field-of-view (FoV) [RD5], illustrated in Fig. 6.

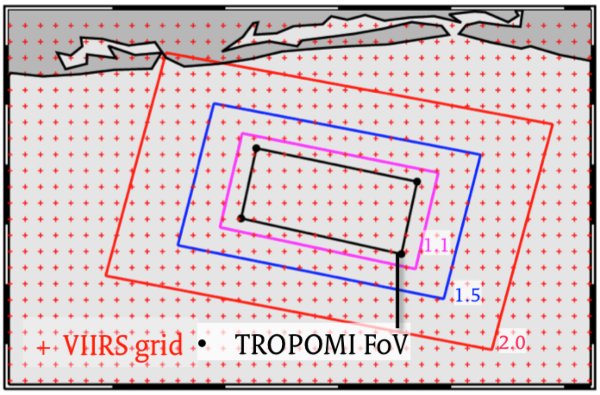

Figure 6: Schematic representation of the different Field-of-Views (FoVs) as defined for the SNPP-VIIRS cloud mask for TROPOMI measurements. The smallest FoV (black) corresponds to the TROPOMI footprint with the corner point defined as the midpoints between the centers of the FoV. The others FoVs are larger (corresponding to 1.1, 1.5 and twice the amount of energy contained in the FoV), for users to increasingly filter more clouds, including those in neighbouring pixels.

The standard VIIRS Cloud Mask determines a cloud classification for every VIIRS ground pixel based on a set of threshold tests using radiances in the visible, near-infrared, shortwave infrared and thermal infrared wavelength range. VIIRS pixels are eventually classified as confidently clear, probably clear, probably cloudy or confidently cloudy. The VIIRS cloud mask for TROPOMI gives the number of VIIRS pixels with a particular cloud classification for each definition of the FoV. There there are four numbers of confidently clear pixels ($N_{\mathrm{c.clr}}$), four numbers of probably clear pixels ($N_{\mathrm{p.clr}}$), four numbers of probably cloudy pixels ($N_{\mathrm{p.cld}}$) and four numnbers of probably cloudy pixels ($N_{\mathrm{p.cld}}$), adding up to the total number of pixels for each definition of the FoV.

The cloud fraction (cf) used for the aerosol layer height algorithm closely follows the definition implemented by the methane retrieval algorithm [20]. Accurate cloud screening is important for methane retrieval as well and the development of the VIIRS cloud mask for TROPOMI is mainly driven by this requirement. It is defined as

$$\mathrm{cf} = \frac{N_{\mathrm{c.cld}} + N_{\mathrm{p.cld}}}{N_{\mathrm{c.cld}} + N_{\mathrm{p.cld}} + N_{\mathrm{c.clr}} + N_{\mathrm{p.clr}}} \tag{1}$$

for the smallest FoV. The VIIRS cloud mask for TROPOMI also contains the mean and the standard deviation of radiances for the VIIRS pixels within a TROPOMI field-of-view.

A dedicated cirrus test using the 1.38 μm channel is part of the standard VIIRS Cloud Mask, but thin cirrus may still be missed as illustrated in [RD5]. For ALH, detection of thin cirrus is important and next to using the VIIRS cloud classifications re-gridded to the TROPOMI grid, a separate threshold test to the mean radiance at 1.38 μm is also applied.

The cloud mask from VIIRS is not available in near real-time (NRTI). Cloud masking for the NRTI processing mode are taken from the FRESCO algorithm. FRESCO cloud parameters are aalso a fallback for the off-line processing stream in case the VIIRS cloud mask is unavailable.

5.1.2 Snow or ice covered pixels

In case of drifting sea ice or land temporarily covered with snow or ice, the true surface albedo substantially deviates from its climatological value. Actual snow or ice cover is provided by the National Snow & Ice Data Center (NSIDC) and ECMWF, which is used to exclude those pixels.

5.1.3 Sunglint

The strongest violation of the Lambertian approximation for the reflectivity of the ground surface occurs for surfaces exhibiting specular reflection of direct sunlight. Oceanic pixels for which the viewing geometry is such that sunglint is to be expected are excluded from analysis. A minimum sunglint angle of 18° is applied, with the sunglint angle α defined as

$$\cos\alpha = \cos\theta_0 \cos\theta + \sin\theta_0 \sin\theta \cos(\phi - \phi_0) \tag{2}$$

in which θ_0 is the solar zenith angle, θ the viewing zenith angle and $\phi - \phi_0$ the relative azimuth angle.

5.1.4 Pixels containing aerosol

Only cloud-free pixels are selected for processing using the screening described above. However, thick plumes of especially volcanic ash, pyrocumulus smoke plumes and desert dust may sometimes be mistaken for clouds. Particularly detection of the first case is important in near real-time processing for aviation safety. Therefore, pixels that contain elevated absorbing aerosols indicated by a UVAI$>$1.0 are included in the analysis. Calculation of this index is a very fast operation. In this way, all aerosols in cloud free scenes and all absorbing aerosols in possible cloud scenes will be processed. Flags are set to indicate this selection mechanism.

5.1.5 Pixel selection scheme

Below, the currectly implemented scheme that selects the pixels for ALH retrieval is described. Note that selection steps 7 and 8 are not available for near real-time processing.

Process pixels for which the following criteria are met:

1. Solar zenith angle is smaller than 75° .
2. For pixels over water, sun glint angle is larger than 18° .
3. Standard deviation of elevation inside pixel is smaller than 300 m.
4. Pixel is completely land OR completely water.
5. Pixel does not contain snow / ice according to dynamic input (NSIDC or ECMWF) AND climatological surface albedo at VIS wavelength is smaller than 0.5.
6. FRESCO effective cloud fraction is smaller than 0.04, except if UVAI is larger than 1.0.
7. VIIRS cloud fraction (cf) as defined in Eq 1 is smaller than 0.02, except if UVAI is larger than 1.0. This selection step is not available for near real-time processing.
8. VIIRS cirrus reflectance (1.38 μm) within TROPOMI nominal NIR field-of-view is smaller than threshold T1. This selection step is not available for near real-time processing.
9. The absolute value of the difference between the scene albedo at 380 nm from the UVAI calculation and the climatological surface albedo at 380 nm is smaller than a particular threshold. This difference threshold is the maximum of an absolute value (0.05) and a relative value (25% of the climatological surface albedo at 380 nm). This is a first test to filter out clouds.

5.2 Forward model

This section provides a detailed description of the current implementation of the forward model for the Aerosol Layer Height retrieval algorithm. The forward model is based on a neural network (NN) trained to estimate the irradiances, radiances and their derivatives with respect to ALH and AOT in the O_2 A band wavelength window and the surface albedo in the continuum near the O_2 A band. This approach replaces the original line-by-line computation done with the Radiative Transfer Model (RTM) "Determining Instrument Specifications and Analyzing Methods for Atmospheric Retrieval" (DISAMAR) [RD6], [RD7], which was used to develop and test the ALH algorithm. The NN implementation improves the forward computation speed by several orders, which makes it possible to retrieve ALH for all TROPOMI pixels on a near-real time basis. The NN implementation reduces the accuracy of the ALH, but several tests (see section 8) show that the reduction is limited. The neural network was trained with spectra simulated with DISAMAR, and all the test results described in this ATBD are valid also for the NN forward model implementation.

5.2.1 Overview

The forward model calculates reflectances for an atmosphere in which Rayleigh scattering, gas absorption, and scattering and absorption by aerosol and clouds can take place. The atmosphere is bounded from below by a reflecting and possibly emitting ground surface. The monochromatic reflectance R at the top-of-atmosphere at a wavelength λ is defined as [RD2]

$$R(\lambda) = \frac{\pi I(\lambda)}{\mu_0 E_0(\lambda)}, \tag{3}$$

where $I(\lambda)$ is the radiance at the top-of-atmosphere at wavelength λ, E_0 is the solar irradiance at the top-of-atmosphere at wavelength λ, perpendicular to the direction of the incident sunlight, and μ_0 the cosine of the solar zenith angle. The RTM-calculated high-resolution reflectance spectrum is convolved with the instrument's spectral response function (ISRF, [RD8]), to obtain reflectances $R(\lambda_i)$ at the instrument's spectral resolution,

$$R(\lambda_i) = \frac{\pi I(\lambda_i)}{\mu_0 E_0(\lambda_i)}, \tag{4}$$

where λ_i is the central wavelength at the i^{th} spectral point on the sensor, and $I(\lambda_i)$ and $E_0(\lambda_i)$ are the measured radiance and irradiance for that spectral point, respectively.

5.2.2 Radiative transfer model

Monochromatic (high-resolution) reflectances are calculated in DISAMAR with the layer-based orders-of-scattering (LABOS) method. This is a variant of the doubling-adding method (e.g. [11], [22]) in which the adding of the different layers is replaced by orders of scattering for the atmospheric layers.

The atmosphere is first divided into homogeneous layers. Reflection and transmission properties for individual layers are calculated using the doubling method. The orders-of-scattering method is then used to calculate the internal radiation field and the field at the top of the atmosphere. The order of scattering refers to the number of times radiation has been scattered by atmospheric layers instead of atmospheric volume elements. Within a single layer, however, many scattering events can take place. LABOS is more efficient than both the adding method and the classical orders-of-scattering method. A detailed description of this method is given in [RD9].

The settings for the radiative transfer calculations used in the NN model are currently:

- Multiple scattering is taken into account, as this can be significant inside aerosol layers.
- Polarization is ignored, as this substantially reduces computation time. Approximate calculations using scalar radiative transfer will introduce errors due to polarizing aerosols and multiply Rayleigh scattered light. A sensitivity analysis using the 'Fine mode weakly absorbing' aerosol model (Section 7.6.2) has shown that the effect on retrieved aerosol mid pressure is typically much smaller than about 20 hPa. It is in principle possible to include polarization in radiative transfer calculations with DISAMAR .
- Inelastic scattering (rotational Raman scattering) is not implemented. The effect on the O_2 A band reflectance is small (e.g. [58]; [50]), particularly for a nadir-viewing instrument such as TROPOMI. A preliminary sensitivity analysis has shown that the effect on retrieved parameters is much smaller than the effect of other model errors so that we can ignore rotational Raman scattering.

- The atmosphere is assumed to be plane-parallel, but a correction for the attenuation of direct incident sunlight in a spherical atmosphere is made if the solar zenith angle is 60° or larger [6].
- Ten Gaussian points (twenty streams) are used to integrate over the polar angle of the Henyey-Greenstein phase function with an asymmetry parameter g of 0.7.

5.2.2.1 Derivatives of reflectance

Derivatives of the reflectance with respect to the fit parameters direct the iterative solution searching (see Eq. 11) and determine the *a posteriori* error covariance matrix (see Eq. 9 below). In DISAMAR, special attention is given to the derivatives. All derivatives, except those for wavelength calibration, are calculated in a semi-analytical manner using reciprocity (equivalent to the adjoint method; e.g. [32]), to enable fast and accurate calculations. In the NN forward model, the derivatives havce to computed from models that have to be trained seperately. Therefore, in the current set-up, the NN forward model consists of five models, one for the reflectance and four for derivatives with respect to aerosol layer height, aerosol optical thickness, and surface alebedo at two wavelengths.

Accurate derivatives are particularly important for the Aerosol Layer Height retrieval, since errors in the aerosol optical thickness and surface albedo are highly correlated. The correlation coefficient can be well above 0.9 and convergence becomes problematic in case of highly correlated fit parameters.

5.2.2.2 Oxygen absorption cross section

A study by De Haan [RD10] has shown that using O_2 line parameters from the most recent HITRAN database [ER1] and assuming a simple Voigt profile for the shape of the absorption line is not sufficient for a reasonably accurate retrieval of aerosol properties. The most prominent issues concern inclusion of line mixing (LM) and collision-induced absorption (CIA) into the absorption cross section. Sensitivity analyses in [RD10] show that ignoring LM and CIA leads to significant biases in retrieval of aerosol properties, much more than in retrieval of cloud properties.

At present, DISAMAR includes first-order line mixing and collision-induced absorption by O_2-O_2 and O_2-N_2 according to [54] and [55]. The former HITRAN 2008 database was replaced by a database from Jet Propulsion Laboratory (JPL), which have slightly more accurate line parameters [55].

Based on data published in Tran and Hartmann (2008) [55], De Haan [RD10] estimates the uncertainty in the improved model for collision-induced absorption and line mixing to be of the order of 20%. He shows that significant biases in retrieved aerosol height remain in that case for optically thin aerosol layers close to the surface. For example, an aerosol layer with τ_0 of 0.2 at 850 hPa over vegetated land shows a bias of approximately 100 hPa, while retrieval for layers closer to the surface does not converge. In Section 7, the effect of spectroscopic uncertainties on retrieval of aerosol height is further investigated.

5.2.3 The Neural Network forward model

In total, 3980 absorption lines have been identified in the oxygen A band to retrieve ALH with sufficient accuracy. Line-by-line (LBL) monochromatic calculation of TOA reflectance, and its derivatives with respect to z_p and τ, on such a high resolution wavelength grid requires approximately 20–30 seconds to complete on a computer equipped with Intel®Xeon®CPU E3-1275 v5 at a clock speed of 3.60 GHz. In an iterative (OE) framework, the retrieval of z_p takes between 3–6 iterations, depending on the amount of aerosol information available in the observed spectra, which controls the derivatives that drive the OE. With a monochromatic forward RTM this would mean a severe limitation of the number of processable pixels, since the computation time for one pixel is very much larger than the measurement time. E.g. for the TROPOMI ALH processor, a time frame of approximately half an hour is available to process a number of 1.4 million spectra. Obviously, LBL computations are unsuitable for the necessary high-speed processing of spectra. To reduce the computational time required for retrieving z_p, a neural network forward model was implemented to predict the radiances and derivatives in the forward model step.

A neural network (NN) model was trained using the Tensorflow™ module developed at Google®[ER2], which is freely available and readily usable. However, the implementation of the NN into the ALH optimal estimation scheme was build independently, to facilitate the interface between the NN and the operational retrieval algeorithm. The current architecture of the NN-augmented operational ALH processor includes five types of NN models, one estimating the top of atmosphere sun-normalised radiance, two estimating the

Table 1: Scene-dependent input model parameters for the NN model.

Parameter class	**Model Parameters**	**Remarks**	limits
Geometry	Solar zenith angle (θ_0)	feature vector	0–75°
	Solar azimuth angle (ϕ_0)	feature vector	-180–180°
	Viewing zenith angle (θ)	feature vector	full swath
	Viewing azimuth angle (ϕ)	feature vector	-180–180°
Aerosol parameters	Aerosol fraction	fixed	1.0
	Single scattering albedo (ω)	fixed	0.95
	Aerosol optical thickness (τ)	feature vector	0.0–15.0
	Aerosol mid pressure (p_{mid})	feature vector	100–1020 hPa
	Aerosol layer thickness (p_{thick})	fixed	50 hPa
	Scattering phase function	fixed	Henyey-Greenstein
	asymmetry factor (g)	fixed	0.7
	Ångström exponent (Å)	fixed	0.0
Meteorological parameters	Temperature	feature vector	temperature at z_{p}
Surface parameters	Surface pressure (p_s)	feature vector	520–1048.5 hPa
	Surface reflectance model	LER	
	Surface albedo (A_s)	feature vector	$2.0 \cdot 10^{-7}$ – 0.70

derivatives of the reflectance with respect to z_{aer} (in hPa^{-1}), and τ, and two estimating the derivatives with respect to the surface albedo at two wavelengths in the continuum below and beyond the O_2 A band.
All five neural network models share the same input model parameters, listed in Table 1. When the parameter is part of the NN feature space, the parameter is listed in the so-called feature vector, while parameters that are constant for all NN trainings are called fixed. E.g. aerosol fraction is set to 1.0 for the entire NN space, since pixels are assumed to be cloud-free and entirely aerosol-filled. Typical parameters to vary are the solar-satellite geometry, meteorological and surface parameters, which should span all possibilities that are encountered in the measurements as best as possible. Histograms of the varied parameters in the NN training are plotted in Figure 7. Since the various aerosol parameters (the aerosol single scattering albedo, scattering phase function, asymmetry factor and Ångström exponent), are fixed in the operational ALH retrieval algorithm, they are fixed in the NN training as well.

Generally, the required training data size increases with increasing non-linearity between input an output layers in a neural network. Once the input model parameters in Table 1 have been gathered, the RTM calculates TOA sun-normalised radiance and the derivative of reflectance with respect to aerosol and surface parameters. This is, by far, the most time consuming step, since each model run requires LBL computations. For TROPOMI, a training set of 1,000,000 samples was found to produce sufficiently accurate results. The solar-satellite geometry for this training set was determined from a random S5P orbit, the meteorological parameters were derived from the 2017 60-layer ERA-Interim Reanalysis data [RD11], and aerosol and surface parameters were generated randomly.

There are 5 NN models for ALH, all consisting of 4 files, with a total size of 9.1Mb.

5.2.4 NN configuration and training

To train the NN and to test the training, the generated spectra were randomly split in a 0.85:0.15 ratio. One part was used to the train the NN, while the other part was used to test the trained NN. In Figure 8 an example of a LBL-generated and an NN-generated Sun-normalised radiance spectrum is shown.

The influence of the atmosphere on the TOA reflectance is characterised using an atmosphere-surface model, consisting of, at least, these relevant components: (1) surface reflectance, (2) surface pressure, (3) temperature profile, (4) aerosol model, (5) aerosol profile, and (6) oxygen absorption.

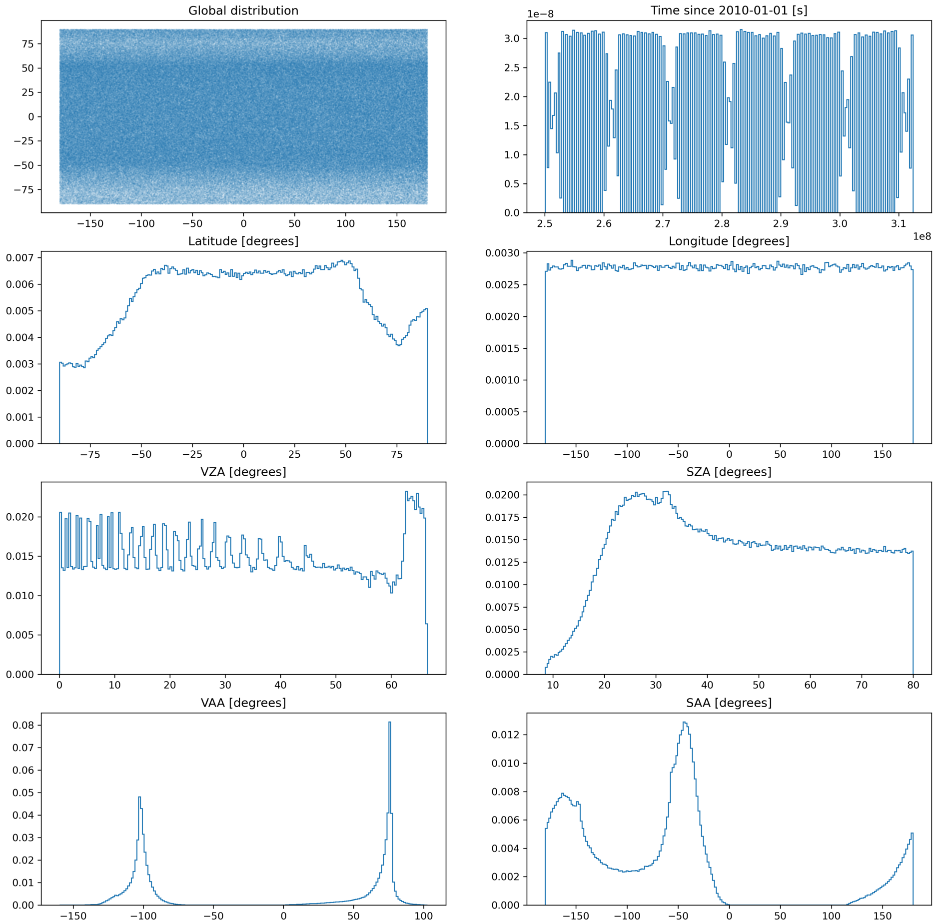

Figure 7: Overview and histograms of the parameters varied in the NN training.

5.2.4.1 High-resolution solar irradiance model

The solar irradiance spectrum is based on [RD12]. The near-infrared wavelength region of this spectrum has a full width at half maximum (FWHM) of 0.04 nm and is oversampled by a factor of four, while the rest of the spectrum is equal to the high-resolution solar reference spectrum described in [RD12]. Differences between the two spectra in the ALH fit window are less than 0.2%.

5.2.4.2 Instrument model

The instrument model for retrieval contains radiance and irradiance slit functions for the convolution of high-resolution radiance spectra, irradiance spectra and derivatives. Furthermore, it contains various instrumental effects that can be applied to the (ir)radiance spectra.

5.2.4.3 Wavelength calibration

The wavelength calibration for the radiance spectra is part of the Level-2 processor and is performed in a separate step before the main Level-2 retrievals take place. Since the ALH algorithm relies heavily on the correct placement of absorption lines, and shifts of 0.002 nm already yield a strong degradation of the end

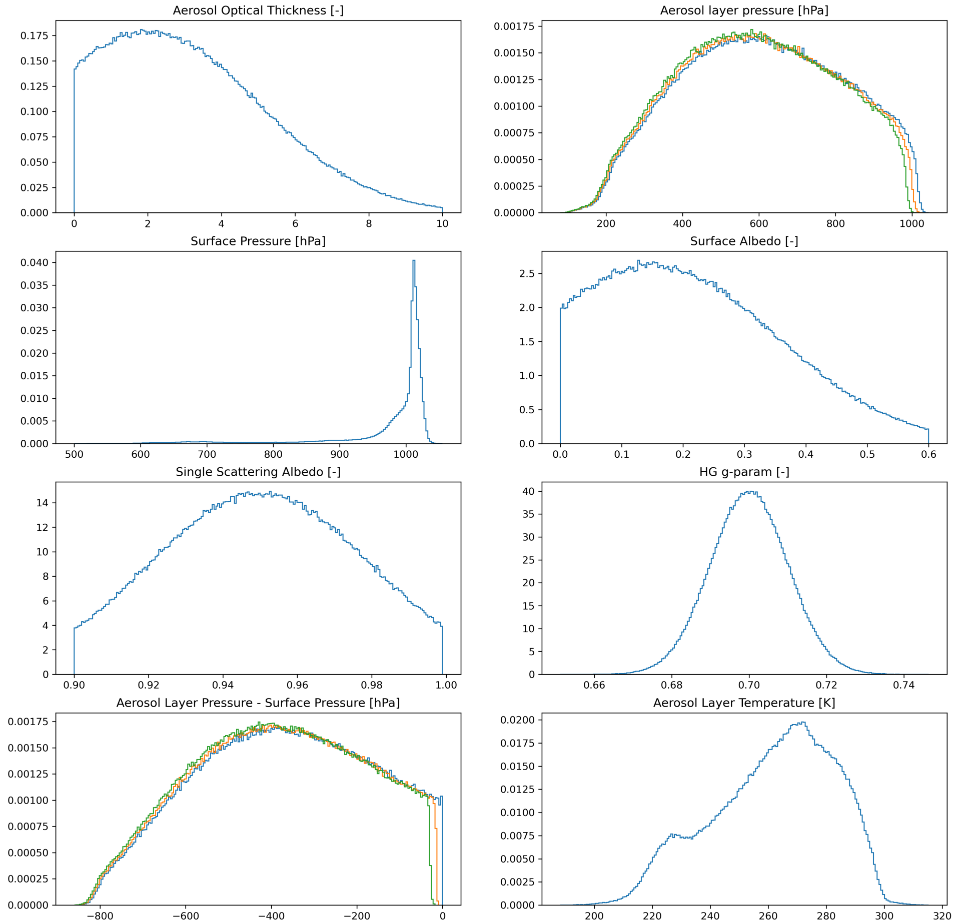

Figure 7: **Cont.** Histograms of parameters varied in the NN training.

result, both the irradiance and radiance wavelength grids will be fitted to Fraunhofer lines in the 758–770 nm wavelength range. The Aerosol Layer Height algorithm focuses on cloud-free scenes, and wavelength offsets due to inhomogeneous illumination of the slit from clouds in the field of view can be expected to be minimal. Therefore, a wavelength calibration, which is normally non-linear [RD13], can be kept linear for the ALH algorithm, using a wavelength offset $\delta\lambda$ only, in a fit window between 758 and 770 nm. Changes due to ozone absorption can be ignored.

The offsets $\delta\lambda$ are determined using an optimal estimation fit, starting with a shift of zero. The shift is at most one third of the spacing of the wavelength grid.

The wavelength calibration has to be performed before the optimal estimation is started, because the forward model expects calibrated radiances and irradiances.

5.2.4.4 Surface reflection

The ground surface is modeled as an isotropically reflecting (Lambertian) surface. Spectral variation in the reflectivity of the ground surface across the O_2 A band exists for vegetated land and deserts [29]. In the forward model, a linear wavelength dependence of the surface albedo is assumed to account for this variation. The albedo is specified at two wavelength nodes (the edges of the fit window at 758 and 770 nm) and other values are found by linear interpolation.

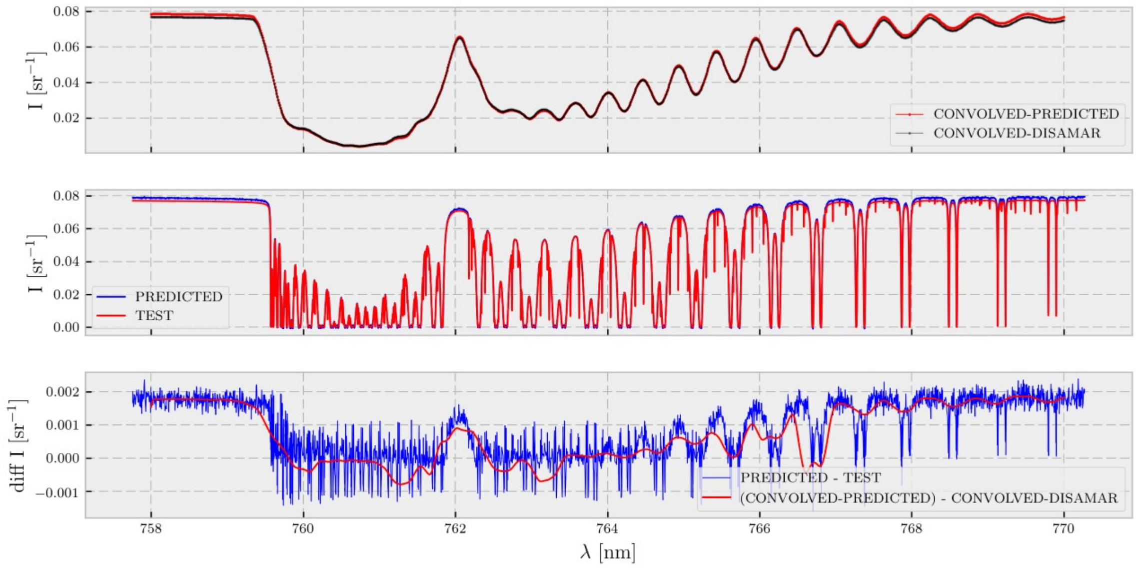

Figure 8: Example of the Sun-normalised radiance spectrum in the Oxygen-A band as computed by the RTM and by the NN model. The top panel shows the spectra after convolution with the S5P slit function, the middle panel shows a comparison between the high resolution spectra, and the bottom show the difference between the LBL and NN spectra, for the high resolution and convoluted spectra.

Accurate climatological albedo values are important for a proper retrieval of the aerosol layer height. Inaccuraccies, over land particularly, lead to biased or non-convergent retrievals (Section 7.7). Currently, the TROPOMI Directional Lambertian Equivalent Reflectivity (DLER) database version 2.0 is used [RD14] as input, built at the native TROPOMI 3.5 km x 5.6 km resolution. The current TROPOMI DLER climatology has monthly nodes at 0.125 x 0.125 degrees, which replaces the previous GOME-2 LER database at 0.25 x 0.25 degrees resolution. Directional LER values showed non-convergent results over many (land) areas. The reason is a higher value of the surface reflectence due to the directionality, which, as a result of inaccuracies in the surface reflectance values, can become larger than the true surface reflectence. In this case, the fitted aerosol optical thickness in the retrieval becomes negative, and a aerosol layer height cannot be found. To avoid these situations, the non-directional LER value, which is determined by the lowest surface reflectances in a particular month for cloud free scenes, is used to ensure a positive aerosol optical thickness in the fitting procedure as much as possible.

With the introduction of version 2.6.0 the LER values are used as *a priori* values in the optimal estimation fit.

5.2.4.5 Aerosol model

An aerosol layer is modeled as a layer of particles with an associated aerosol optical thickness (τ_0). The ratio of scattering and absorption is controlled by the single scattering albedo (ω_0). The phase function $P(\theta)$ describes the angular distribution of scattered light, which is modeled using a Henyey-Greenstein function, given by

$$P_{HG} = \frac{1-g^2}{(1+g^2-2g\cos\theta)^{3/2}} \tag{5}$$

where g is the asymmetry parameter and θ the scattering angle. A single, average aerosol model is assumed in the operational algorithm, with average values for the single scattering albedo (0.95) and asymmetry parameter (0.7) in this wavelength range for all main aerosol types as found in long-term Aerosol Robotic Network (AERONET) observations [13].

The error analyses in Section 7.6 show that if the assumed aerosol model deviates from the true aerosol type, biases in retrieved aerosol pressure generally remain relatively small, particularly when the surface albedo is a fit parameter. Retrieved aerosol optical thickness and surface albedo, however, show significant biases in response to model biases in single scattering albedo and phase function. Retrieved values for these two parameters should therefore be understood as effective quantities.

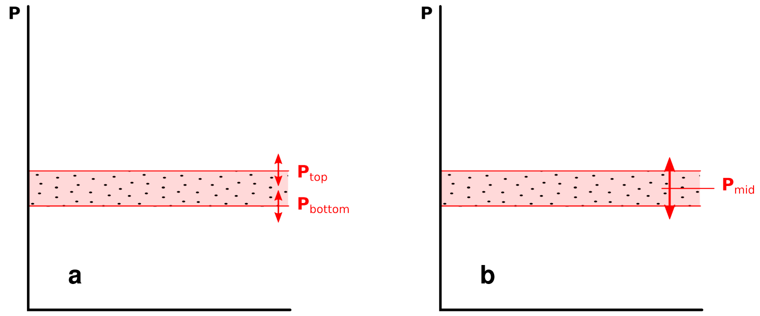

Figure 9: Aerosol profile parameterization for the TROPOMI Aerosol Layer Height product. (a) The baseline profile parameterization assumes an elevated layer with a fixed geometric difference between top and bottom of the layer. Internally, the optimal estimation routines fits the the top and bottom pressures, which are converted in each step to a fixed thickness assuming hydrostatic equilibrium. (b) The reported pressure is the layer's mid pressure. This mid presure is converted to a height and reported as the layer's mid height above the geoid.

5.2.4.6 Aerosol profile

Although the O_2 A band is a strong line absorption spectrum that spans a large range of absorption optical thicknesses, it contains limited aerosol profile information (e.g. [19]; [49]; [8]; cf. [9]). Therefore, the aerosol profile is defined as a single layer with a fixed geometrical thickness. In the forward model, the atmosphere is divided into a small number of pressure intervals that do not overlap. These intervals may be aerosol-free and cloud-free, or contain aerosol or clouds with a certain aerosol / cloud fraction. Aerosol or cloud properties of only one atmospheric interval can be fitted. In the aerosol layer, the aerosols are assumed to be uniformly distributed with a constant aerosol volume extinction coefficientm and aerosol single scattering albedo, and an aerosol fraction of one (Figure 9a). The optimal estimation routines fits the the top and bottom pressures, which are converted in each step to a fixed thickness assuming hydrostatic equilibrium (sect. 5.2.4.7). Ultimately, the layer's mid pressure is retrieved, which is converted to a height and additiionally reported as the layer's mid height above the geoid (Figure 9a), which is approximately the average sea level.

5.2.4.7 Height variable

Pressure is the independent height variable in the algorithm. Given a pressure grid and associated temperatures and the surface altitude, the altitude grid is calculated assuming hydrostatic equilibrium

$$z_i = z_s + \int_{\ln(p_i)}^{\ln(p_s)} H(T)\, d\ln(p) \tag{6}$$

where z_i is the altitude corresponding to pressure level p_i, z_s is the altitude at the surface, p_s is the surface pressure. The integration variable is $\ln(p)$, the natural logarithm of the pressure. The integration interval runs from $\ln(p_i)$ to $\ln(p_s)$. The scale height $H(p)$, in meter, is

$$H(T) = \frac{RT(p)}{g(p)M} \tag{7}$$

where R is the universal gas constant, $8.3144621\,\mathrm{JK^{-1}mol^{-1}}$, M is the mean molecular weight of air, $28.964 \cdot 10^{-3}\,\mathrm{kg\ mol^{-1}}$, dry air only. $T(p)$ is the temperature at pressure level p in Kelvin, and $g(p)$ is the gravitational acceleration in $\mathrm{ms^{-2}}$. Note that the gravitational acceleration $g(z)$ is given in terms of the altitude above the geoid, which means that the altitude grid can only be calculated iteratively. The initial altitude grid used for the gravitational acceleration assumes a fixed scale height H of 8300 m. A repeated gauss integration using 2 gaussian division points is used on each interval $[\ln(p_i+1), \ln(p_i)]$ and the values at the division points are obtained using cubic spline interpolation on $\ln(p)$ and T.

An atmospheric layer with a fixed geometric thickness has different pressure differences at different heights. In the algorithm, the layer top and bottom altitudes are computed from the layer mid height and the fixed layer thickess, and converted into layer top pressure and bottom pressure at each iteration. The pressures are fitted and the layer mid height is computed from the retrieved layer mid pressure.

5.2.4.8 Temperature-pressure profiles

Temperature profiles are determined from the European Centre for Medium-Range Weather Forecasts (ECMWF) pressure fields at a $1^\circ \times 1^\circ$ grid, interpolated to the satellite grid.

5.2.4.9 Surface pressure

Surface pressure are determined from the same ECMWF temperature-pressure fields as above, interpolated to the satellite grid.

5.3 Algorithm description: Retrieval method

This section provides a description of the retrieval method for the Aerosol Layer Height retrieval algorithm and it discusses *a priori* information for its main fit parameters.

5.3.1 Optimal Estimation

The retrieval method is based on the Optimal Estimation procedure [41]. The implementation of Optimal Estimation in DISAMAR is described in [RD9].

Optimal Estimation is a form of regularization that constrains the least-squares solution by a priori knowledge. The cost function that is minimized is given by

$$\chi^2 = [\mathbf{y} - \mathbf{F}(\mathbf{x},\mathbf{b})]^T \mathbf{S}_\varepsilon{}^{-1} [\mathbf{y} - \mathbf{F}(\mathbf{x},\mathbf{b})] + (\mathbf{x} - \mathbf{x_a})^T \mathbf{S_a}{}^{-1} (\mathbf{x} - \mathbf{x_a}), \tag{8}$$

where $\mathbf{y}$ is the vector of measured reflectance, which contains values for the different wavelengths; $\mathbf{F}(\mathbf{x},\mathbf{b})$ is the vector of calculated reflectances, which is also called the forward model; $\mathbf{x}$ is the state vector containing the parameters that are fitted; $\mathbf{b}$ is the vector containing the model parameters; is the error covariance matrix of the measurement; $\mathbf{x_a}$ is the a priori state vector; and $\mathbf{S_a}$ is the error covariance matrix associated with the a priori state vector.

An important advantage of the Optimal Estimation formalism is that it provides a proper error analysis. Minimization of χ^2 gives the retrieved state vector: the associated (*a posteriori*) error covariance matrix is given by

$$\hat{\mathbf{S}} = (\mathbf{K}^T \mathbf{S}_\varepsilon \mathbf{K} + \mathbf{S_a}{}^{-1})^{-1}. \tag{9}$$

where $\mathbf{K}$ is the matrix of derivatives (evaluated at in Eq. 8),

$$K_{ij} = \frac{dF_i}{dx_j}. \tag{10}$$

Note that matrix $\mathbf{K}$ provides the derivatives of measured reflectance, i.e. high-resolution derivatives after appropriate convolution with the slit functions.

Generally, the forward model is non-linear so that minimization of the cost function has to be solved iteratively. In the ALH retrieval it is implemented using te the Gauss-Newton method. The update of the state vector during iteration is given by

$$\mathbf{x}_{n+1} = \mathbf{x_a} + (\mathbf{K_n}{}^T \mathbf{S}_\varepsilon{}^{-1} \mathbf{K_n} + \mathbf{S_a}{}^{-1})^{-1} \mathbf{K_n}{}^T \mathbf{S}_\varepsilon{}^{-1} [\mathbf{y} - \mathbf{F}(\mathbf{x_n}) + \mathbf{K_n}(\mathbf{x_n} - \mathbf{x_a})], \tag{11}$$

where $\mathbf{x_n}$ are subsequent iterates of the state vector or linearization points of the forward model. Hence, $\mathbf{K_n}$ is the derivative matrix evaluated at $\mathbf{x_n}$. In some cases exceptions are made. For example, when the change in the state vector is very large, the update is reduced. Also, if elements of the state vector are assigned non-physical values (e.g. negative surface albedo) they are reset to physical values. The iteration is typically started with $\mathbf{x_1} = \mathbf{x_a}$.

A χ^2-minimum has been found and the fit has converged if during iteration the state vector's update is small compared to the expected precision. An appropriate measure for the size of the update is

$$d_n^2 = (\mathbf{x_{n+1}} - \mathbf{x_n})^T \mathbf{S_n}{}^{-1} (\mathbf{x_{n+1}} - \mathbf{x_n}), \tag{12}$$

where is $\mathbf{S_n}$ the *a posteriori* covariance matrix for the n^{th} iteration. If $d_n{}^2$ becomes smaller than a predefined threshold, iteration is stopped, and $\mathbf{x_{n+1}}$ and $\mathbf{S_n}$ become $\hat{\mathbf{x}}$ and $\hat{\mathbf{S}}$, respectively. The convergence criterion is typically equal to the number of state vector elements *m*. It is important to note here that a convergence test only ensures that a local minimum has been reached. It does not ensure that the minimum is actually the correct solution (global minimum). A test for convergence should therefore be supplemented by an evaluation of the actual value of χ^2 (a high value would indicate a non-global minimum), inspection of the residual spectrum or a check of the consistency of retrieval results with neighboring pixels.

5.3.2 State vector elements and *a priori* information

In the current implementation of the Aerosol Layer Height retrieval algorithm, the state vector contains the elements printed in bold in Table 2. Other parameters which are known to influence the accuracy of the ALH are also given in Table 2, with typical *a priori* values and errors. However, implementation is not currently foreseen.

Table 2: State vector elements and typical *a priori* values and errors for the Aerosol Layer Height retrieval algorithm. In the current implementation, the state vector contains the parameters printed in bold.

State vector element	*a priori value*	*a priori* error (1σ)	Remark
Aerosol mid pressure p_{mid}	800 hPa	500 hPa	Alternative profile parameterizations (5.3.8) are optional.
Aerosol optical thickness (τ_0)	0.2	1.0	At 760 nm
Surface albedo ($\mathrm{A_s}$) at 758 nm **Surface albedo ($\mathrm{A_s}$) at 770 nm**	climatology	0.2	TROPOMI LER
Surface pressure (p_s)	ECMWF	3 hPa	
Temperature offset ΔT	0 K	3 K	Offset to the *a priori* ECMWF temperature profile
Fluorescence emission (F_s) at 758 nm Fluorescence emission (F_s) at 770 nm	0.0 0.0	$1.0{\cdot}10^{12}$ ph. $\mathrm{cm^{-2}}$ $\mathrm{s^{-1}}$ $\mathrm{nm^{-1}}$ $\mathrm{sr^{-1}}$ $1.0{\cdot}10^{12}$ ph. $\mathrm{cm^{-2}}$ $\mathrm{s^{-1}}$ $\mathrm{nm^{-1}}$ $\mathrm{sr^{-1}}$	Over vegetated land only.
Stray light	0%	1%	Additive radiance offset defined as a percentage of the radiance at 758 nm

6 Feasibility

6.1 Timeliness

The Aerosol Layer Height product has a near real-time requirement.

A test was performed to assess the computation time spent by the ALH processor with a NN implemented in the forward model, using one day of TROPOMI data, shown in Fig. 10. On this day a severe dust storm can be found over the Atlantic Ocean, producing a large number of pixels with sufficiently high TROPOMI AAI. Furthermore, more high AAI hotspots can be identified around the globe. This means many pixels have to processed by the AER_LH processor during this day, which can be considered a normal, but more than average load for the ALH processor.

32% of the pixels were selected for processing this day, and 90.5% of the selected pixels were succesfully processed (actually yielding an ALH), and only 9.5% failed due to retrieval error or warnings. The total time spent on the retrieval was about 4 hours, which yields an average processing time (of the entire day) of 0.0246 s per selected pixel, with 32 parallel processors. This includes initialisation, and also the non-successful pixels, which take longer to process on average, since non-convergence pixel take at most 12 iterations before they are excluded, while successful pixels can converge to an answer in 3-4 iterations.

The timeliness was tested for AER_LH for two periods: from 2019-08-04 00:04:19 UTC, orbit 9358 to 2019-08-06 01:59:19 UTC, orbit 9387, and from 2019-08-06 02:39:29 UTC, orbit 9388, to 2019-08-08 07:46:09 UTC, orbit 9419. The first period consists of 375 near-real time granules and the second period consists of 372 granules. The two periods mark the change of TROPOMI footprint sizes from 7×7 km^2 to 7×5.6 km^2.

Between these periods a transition in the operational settings to a shorter integration time (IT), from 1080 ms to 840 ms, of the TROPOMI measurements was implemented. The total processing time and the processing time per pixel were recorded during both periods and compared. Timeliness for all products are described in [51]. Figure 11 shows the results for AER_LH. No violations of the three hour near-real time timeliness were recorded for AER_LH for either 'large' pixels (1080 ms IT) and 'small' pixels (840 ms IT).

6.2 VIIRS cloud mask

The above estimates were made using the UV aerosol index as the primary criterion for selecting pixels containing (absorbing) aerosols, as defined in previous versions of this ATBD. However, with the VIIRS cloud mask as the primary selection criterion for version 2.2.0, many more pixels are allowed to be assessed, increasing the processing time for the ALH. A test was performed on 6 days in May 2020 (14–19 May 2020) to assess the runtime for the ALH processing given different settings for the VIIRS cloud mask and the FRESCO cloud mask. All available pixels in those days were processed, while the filtering was applied afterwards. The fraction of filtered pixels compared to the total was taken as the indication for the fraction of the time the ALH processor had to perform compared to the total time.

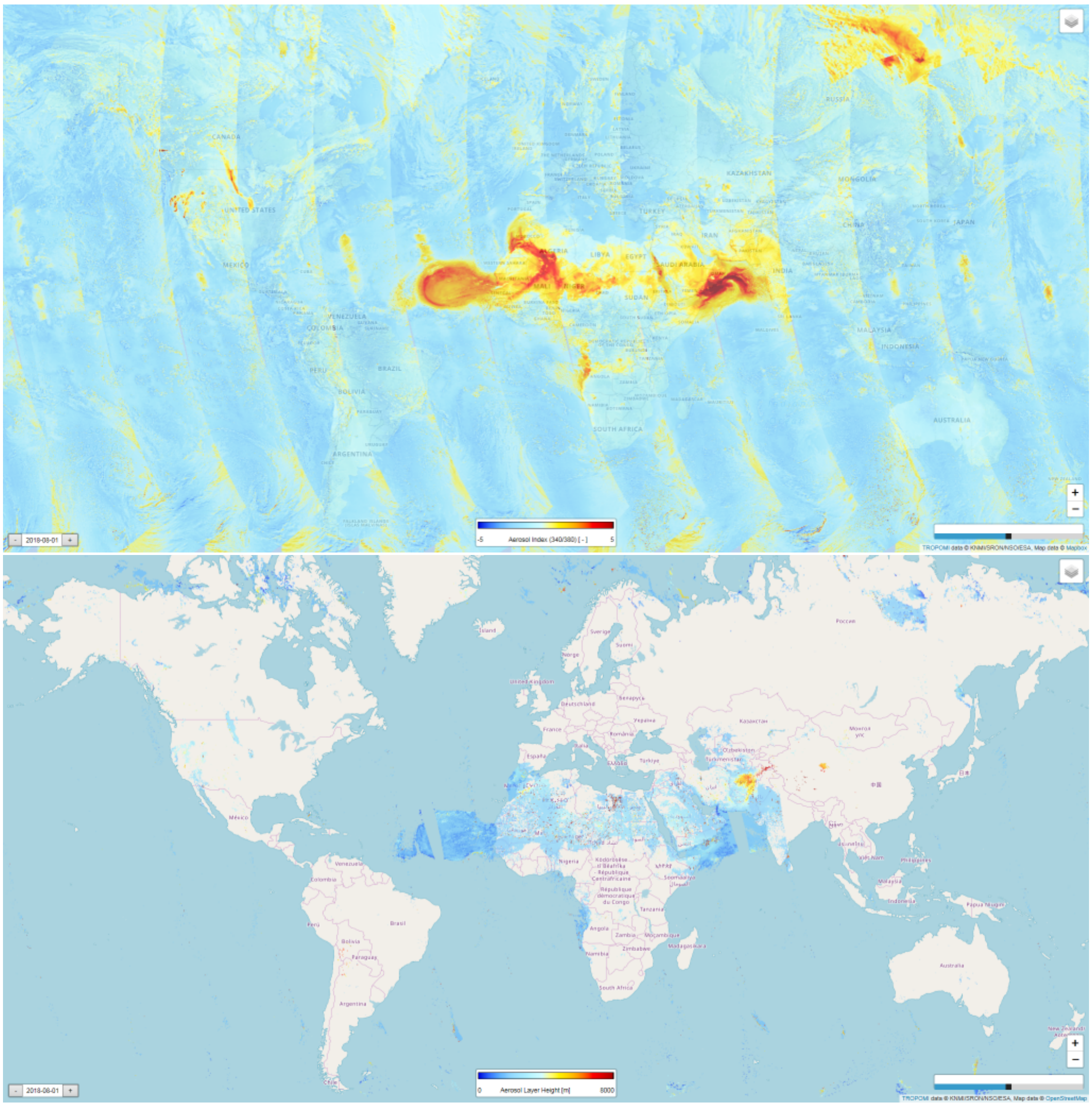

Figure 10: Top panel: TROPOMI AAI on 1 August 2018 showing a large aerosol (dust) plume over the Atlantic Ocean originating from the Sahara, and several other hotspots of high AAI from smoke and dust. Bottom panel: TROPOMI AER_LH retrieval results from an initial test run of the ALH processor with NN implemented in the forward model.

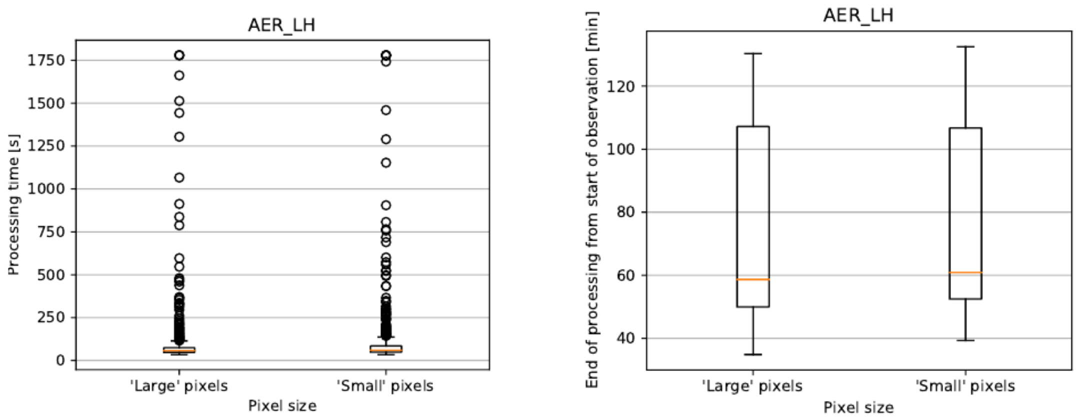

Figure 11: Timeliness of the AER_LH processor. The upper panel shows the processing time per near-real time granule. The bottom panel shows the timeliness of the end of the processing time. 'Large' pixels refer to pixels with an integration time of 1080 ms, yielding pixel sizes of 7×7 km^2 at nadir, 'small' pixels refer to an integration time of 840 ms, yielding pixel sizes of about 7×5.6 km^2.

The result is shown in Fig. 12. It shows the total number of pixels in the various orbits processed without an AAI filter (red) and the percentage of pixels selected by the algorithm v1 settings (i.e. AAI$>$ 0) in green. When the pixel selection is based on the VIIRS cloud mask (black) about 20–25% of the pixels are selected or processing. Adding the sun glint mask reduces this, while the addition of the criterion that all pixels with AAI$>$1 increases this a bit. In total up to about 20% of the total number of pixels would be selected for processing.

For the near real-time processing VIIRS cloud mask is not avialable. Therefore, cloud masking is mainly performed using FRESCO. The amount of pixels selected with FRESCO cf $<$ 0.02, AAI $>$ 1 and no sunglint is shown in Fig. 12. About 10% of the total number of pixels will be selected for processing, which is well within the requirements for the near real-time processing.

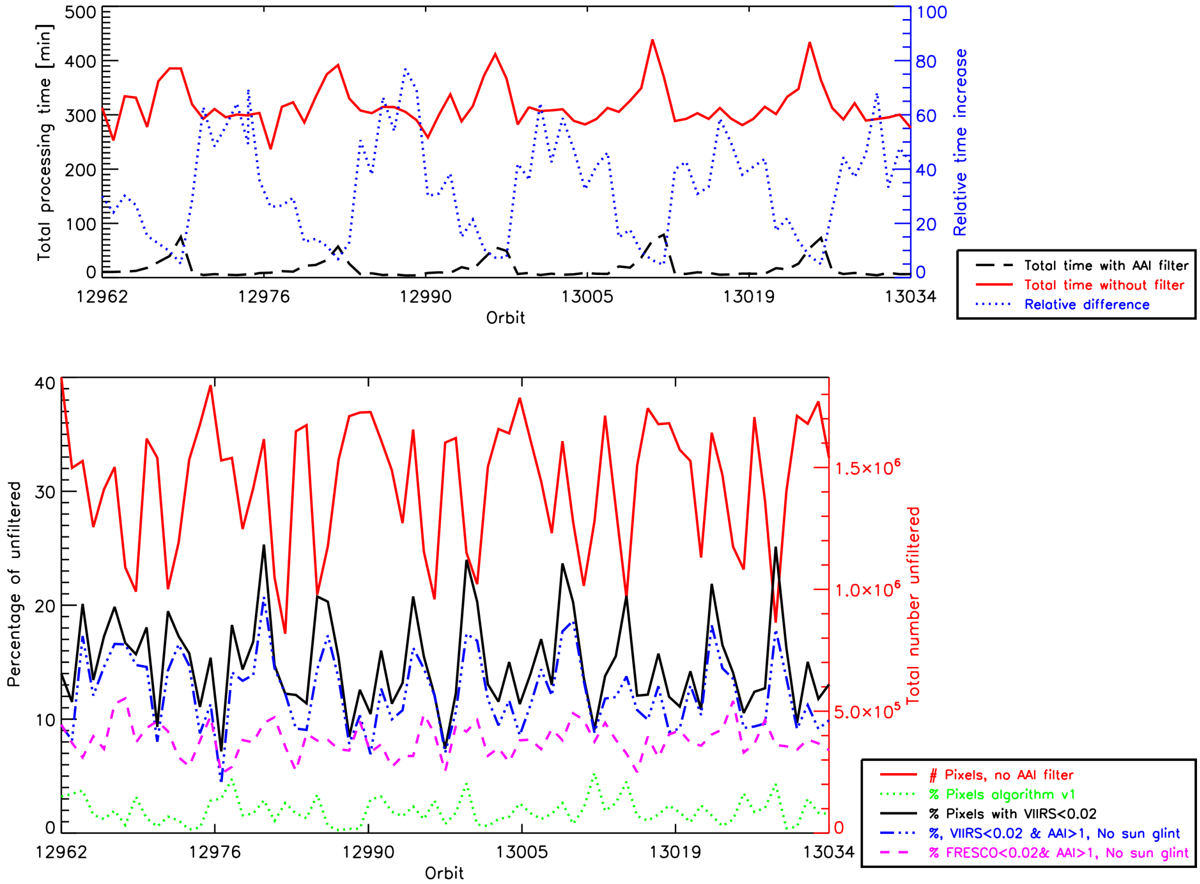

Figure 12: Timeliness of the AER_LH processor. The top panel shows the difference in time spent by the ALH processor with (black) and without (red) AAI filter in absolute time (minutes). The relative difference is shown in blue. In the bottom panel the total number of pixels is shown in red, and the fraction of pixels selected for different selection filters. In green the 'algorithm v1' refers to the ALH algorithm which selected aerosol containing pixels on the basis of an AAI $>$ 0. This resulted in a low number of pixels. In black the fraction of pixels for the VIIRS cf $<$ 0.02 is shown, which selects up to 25% of the pixels for processing. In blue the criteria of no sun glint but processing pixel with AAI$>$ 1 is added. In purple the fraction of pixels for the FRESCO effective cloud fraction $<$ 0.02 AND AAI $>$ 1 is shown.

6.3 Input data for the Aerosol Layer Height algorithm

6.3.1 TROPOMI Level-1b

The following Level-1b data are needed for the Aerosol Layer Height algorithm (Table 3):

Table 3: TROPOMI Level-1b input data.

Name/Data	Symbol	Unit	Pre-process needs	Backup if not available	Comments
Radiance data for band 6	I	mol s^{-1} m^{-2} nm^{-1} sr^{-1}	Per 3.5 km x 5.6 km nadir ground pixel.	No retrieval.	The O_2 A band is contained in band 6; product includes geolocation data.
Irradiance data	E_0	mol s^{-1} m^{-2} nm^{-1}	-	Use previous measurement.	-
Small-pixel column radiance data for band 6	I	mol s^{-1} m^{-2} nm^{-1} sr^{-1}	-	Skip cloud test that uses small-pixel column data.	So-called small-pixel column radiance data are used in the near real-time cloud mask (see Section 5.1).
Radiance data for band 4	I	mol s^{-1} m^{-2} nm^{-1} sr^{-1}	-	Skip cloud test that uses band 4 radiance data.	Radiances in the visible wavelength range are used in the near real-time cloud mask (see Section 5.1).

6.3.2 Dynamic input

Dynamic input data are summarized in Table 4 (offline) and Table 5 (nrti).

Table 4: Dynamic input data for off-line processing and reprocessing.

Name/Data	Symbol	Unit	Source	Pre-process needs	Backup if not available	Comments
Temperature profiles	$T(p_i)$	K	ECMWF	Interpolation to TROPOMI grid	Temperature profiles from TOMS version 8 ozone climatology	3-hour, $1^\circ \times 1^\circ$
Surface pressures	p_s	Pa	ECMWF	Interpolation to TROPOMI grid	Assume 1013 hPa at sea level; use digital elevation model and scale factor of 8.3 km	3-hour, $1^\circ \times 1^\circ$
Snow / ice cover	-	-	NSIDC or ECMWF	Interpolation to TROPOMI grid	TROPOMI DLER climatology	
VIIRS cloud mask	-	-	TROPOMI Level-2 support	Regridding to TROPOMI NIR grid	FRESCO L2	
UV Aerosol Index	-	-	TROPOMI Level-2	Regridding to NIR grid	Select pixel according to cloud mask	

Dynamic input for the near real-time processing mode is summarized in Table 5.

Table 5: Dynamic input data for near real-time processing.

Name/Data	Symbol	Unit	Source	Pre-process needs	Backup if not available	Comments
Temperature profiles	$T(p_i)$	K	ECMWF	Interpolation to TROPOMI grid	Temperature profiles from TOMS version 8 ozone climatology (static).	3-hour, $1^\circ \times 1^\circ$
Surface pressures	p_s	Pa	ECMWF	Interpolation to TROPOMI grid	Assume 1013 hPa at sea level; use digital elevation model and scale factor of 8.3 km	3-hour, $1^\circ \times 1^\circ$
Snow / ice cover	-	-	NSIDC or ECMWF	Interpolation to TROPOMI grid	TROPOMI DLER climatology	
Cloud mask	-	-	TROPOMI FRESCO L2	-	Skip pixel	
UV Aerosol Index	-	-	TROPOMI L-2	Regridding to NIR grid	Select pixel according to cloud mask	

6.3.3 Static input

Static input data are discussed in Section 5 and summarized in Table 6.

Table 6: Static input data.

Name/Data	Symbol	Unit	Source	Pre-process needs	Comments
TROPOMI DLER climatology	A_s	-	[53].	Collocation with TROPOMI ground pixel.	monthly, $0.25^\circ \times 0.25^\circ$
O_2 absorption parameters	-	-	Oxygen line parameters according to [54];[55]. HITRAN [ER1].	Oxygen absorption cross sections are pre-calculated and stored in look-up tables.	-
Surface altitude	z_s	m	GMTED2010[10]; preprocessing according to [RD15].	For TROPOMI ground pixel, calculate mean, standard deviation, maximum and minimum elevation.	
Slit functions for the radiance and irradiance	-	-	TROPOMI L1b product.	-	-
High-resolution solar irradiance spectrum	E_0	mol s^{-1} m^{-2} nm^{-1}	TROPOMI project reference spectrum [RD6] or [RD12].	-	-

6.4 Data product description

A single Level-2 file in the off-line processing stream contains one complete TROPOMI orbit. Such a Level-2 file contains the main groups PRODUCT and METADATA. Main data fields (on a pixel level) are stored in the PRODUCT group and its subgroup SUPPORT_DATA. The METADATA group contains a subgroup called QA_STATISTICS (quality assurance statistics). Quality assurance statistics and metadata items are data fields on an orbit level. Table 7 provides an overview of data fields in the PRODUCT group. A complete description of the data output products can be found in the Product user Manual for the ALH [RD16].

Table 7: Level-2 output data.

Name/Data	Symbol	Unit	Description	Number of Values
aerosol_mid_pressure	p_{mid}	Pa	Layer mid pressure, from layer (top + bottom)/2	1
aerosol_mid_height	z_{mid}	m	Layer mid height with a thickness of 250 m, calculated from mid pressure using the pressure-temperature profile.	1
aerosol_optical_thickness	τ_0	-	Aerosol optical thickness of the aerosol layer at 760 nm.	1
surface_albedo	A_{s}	-	Surface albedo at two wavelength nodes. Polynomial interpolation is used to determine the surface albedo at other wavelengths.	2
a_posteriori_covariance_-matrix	**S**	<various>	*A posteriori* covariance matrix of the state vector. Units of matrix elements are derived from units of state vector elements.	*[variable]*
*[variable]*_precision			Precision of *[variable]*.	*[variable]*.
latitude	-	degrees	Latitude of pixel center.	1
longitude	-	degrees	Longitude of pixel center.	1
solar_zenith_angle	-	degrees	-	1
solar_azimuth_angle	-	degrees	-	1
viewing_zenith_angle	-	degrees	-	1
viewing_azimuth_angle	-	degrees	-	1

Data types for all fields are floats. Assuming ~1 042 800 pixels per orbit and 7 state vector elements, the uncompressed size of an ALH Level-2 file for the data fields of Table 7 is ~360 MB. Since only a cloud-free fraction of the pixels is processed, compression reduces the file size considerably.

7 Error analysis

The purpose of the error analysis is to illustrate the performance of the baseline algorithm. The sensitivity analyses presented from section 7.3 onward are performed with DISAMAR and provide a benchmark for future performance optimizations of the algorithm.

7.1 Performance of the neural network forward model

In this section the forward model in the operational processor, based on the neural network (NN) is compared to a forward model as computed line-by-line by DISAMAR.

In Figure 13 the retrieval of the ALH on 9 November 2018 is shown. It depicts the situation on the west coast of the US, when severe wild fires scourged the surroundings of Paradise, Ca., and large smoke plumes were visible from VIIRS onboard Suomi/NPP, and TROPOMI. In the top-left image the smoke plume is depicted, overlaid with ALH retrievals using line-by-line (LBL) calculation from DISAMAR, which are time-consuming, and therefore not as complete as the ALH retrievals in the top-right picture, which is the same picture overlaid with NN calculation of the ALH. The bottom-left picture shows the difference between the retrievals, while the bottom-right shows a scatterplot of the differences. Clearly, the NN implementation performs very well for this case, showing only minimal differences between the retrieved mid-layer heights using different forward models.

In Figure 14 the scatterplots of the differences between the LBL ALH and NN ALH on the next two days are shown. Again, the differences introduced by the NN iplementation are limited. The largest differences are on 10 Nov. 2018, when sub-pixel clouds make the retrieval unreliable. The NN forward model treats these pixels differently than DISAMAR is some cases. Therefore, the representativeness of the NN ALH is different from the LBL ALH, because the NN will always give a solution within the trained domain, while LBL calculation may fail. However, the accuracy is not so much affected by the NN.

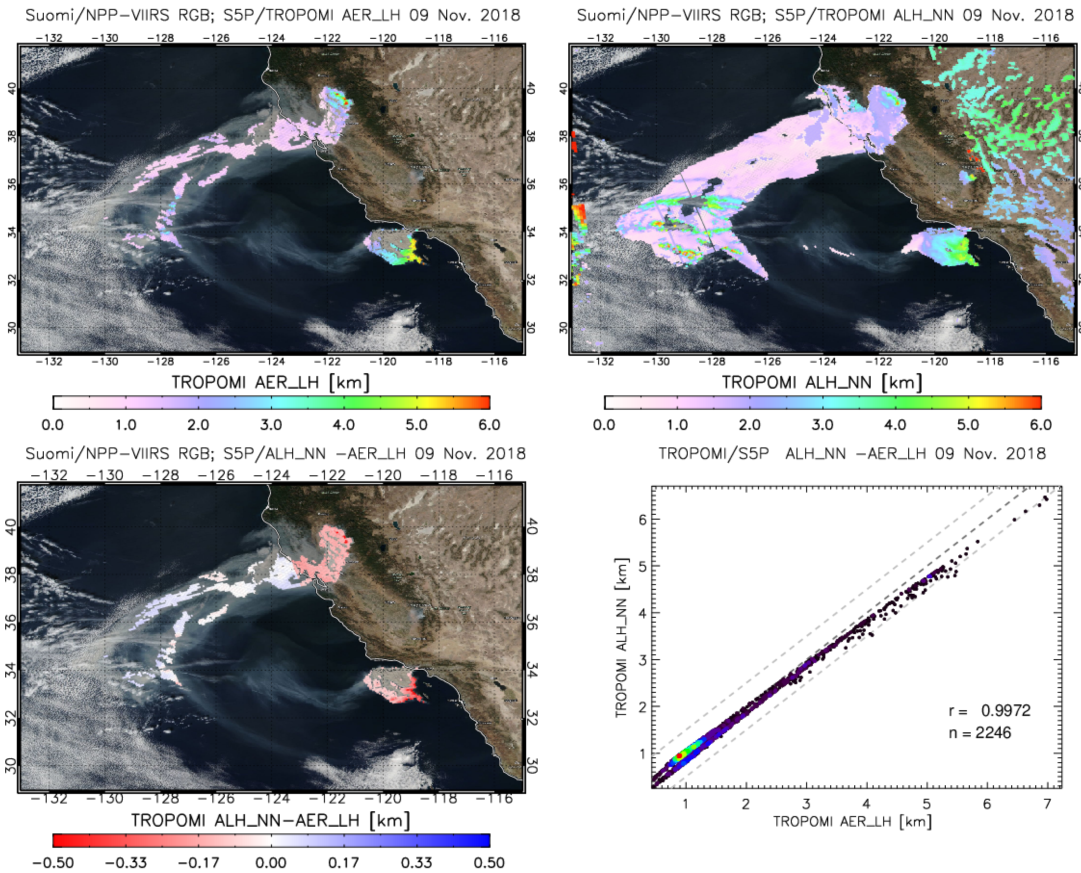

Figure 13: (top-left) Suomi/NPP VIIRS RGB on 9 Nov. 2018, overlaid with LBL ALH ; (top-right) Suomi/NPP VIIRS RGB on 9 Nov. 2018, overlaid with NN ALH; (bottom-left)Suomi/NPP VIIRS RGB on 9 Nov. 2018, overlaid with difference of NN-LBL ALH; (bottom-right) Scatterplot of NN ALH versus LBL ALH for the pixels in the left panels.

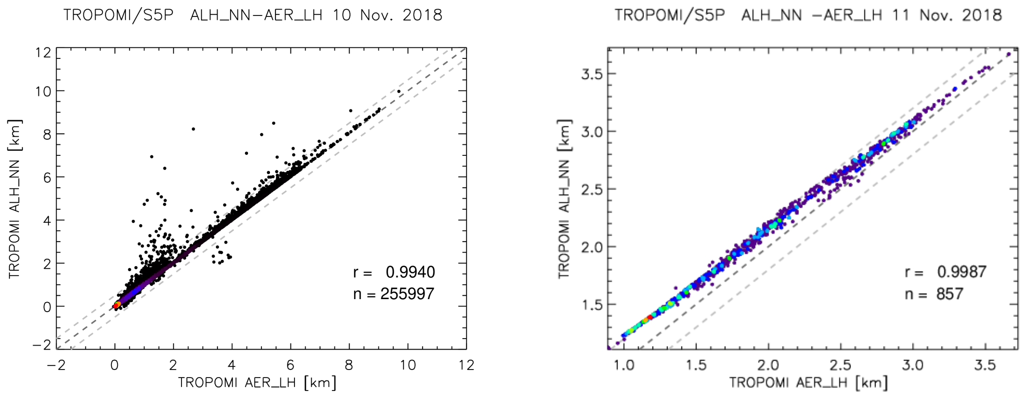

Figure 14: (left) Scatterplot of NN ALH versus LBL ALH on 10 Nov 2018 for the area in Fig 13; (right) Same as the left panel for 11 Nov. 2018.

7.2 Performance of the surface fitting

A simulation test was performed with DISAMAR to investigate the performance of including the surface albedo in the optimal estimation feature vector, see Fig. 15. In the left panel of this figure the ALH is retrieved using only aerosol layer height and aerosol optical in the feature vector, while in the right panel the same rertievals are repeated with surface albedo additionally added to the optimal estimation feature vector. The red crosses indicate the cases with AOD$>$ 0.3 and surface albedo $<$ 0.4, which should provide the best results. The blue dots represent the cases with AOD $>$ 0.3 and surface albedo $>$ 0.4, while the grey dots represent all other cases, including very low AOD and high albedo. The results are clearly improved for all cases.

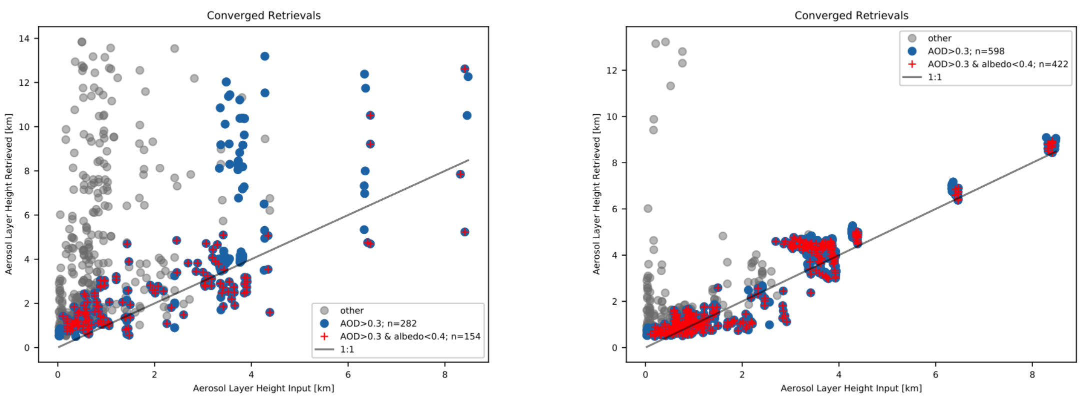

Figure 15: Retrieval of the ALH using a limited set of synthetic data with varying surface albedos, using the DISAMAR RTM (line-by-line computations). On the left the ALH is retrieved using the previous implementation (no albedo fit) and on the right the ALH is retrieved with the surface albedo included in the optimal estimation fit.

In figure 16, a real case of TROPOMI ALH is shown, retrieved on 7 Sept. 2020 over the north-west United States. A complex pattern of wild fire smoke was observed over both land and ocean, together with clouds and snow cover. Although the original aerosol layer height retrieval algorithm manages to retrieve ALH for a significant number of pixels (left panel), the results over land are limited, both in terms of number of successful retrievals as in the ALH result itself. Comparison with CALIOP (not shown) show a bias towards the surface, as is foudn for many land retrievals. Inclusion of the surface albedo in the optimal estimation scheme resulted in a large increase of successful retrievals and an increase in the retrieved altitude (right panel). Many patches over the lower altitude plumes are filled-in in the northern part of the figure, while especially the higher-altitude plumes in the cenetr are retrieved much better. These are the thicker parts the plumes and are important for a reliable algorithm.

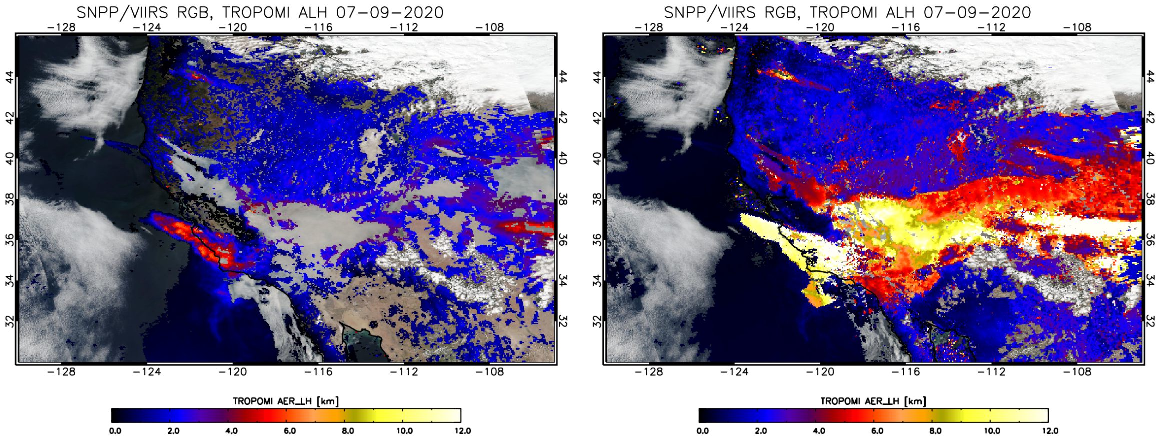

Figure 16: TROPOMI AER_LH retrieval on 7 Sept. 2020 over north-west US, using algorithm version 2.4.0 (left) and version 2.6.0 (right), overlied over an RGB image from SNPP/VIIRS on the same day.

7.3 Default settings for the error analysis

The next sections provide general sensitivities for aerosol layer height retrievals using the O_2 A band. We will first describe the default settings used in the error analysis; these settings are used unless explicitly stated otherwise.

The instrument model used in simulation and retrieval consists of anticipated instrument characteristics for TROPOMI described in Veefkind et al. (2012)[59]. Note that these instrument characteristics are slightly different from the more recent TROPOMI instrument properties described in citeRDS5P-KNMI-L2-0010-RP. The radiance and irradiance slit functions S at the O_2 A band are flat-topped functions with a full width at half maximum of 0.5 nm:

$$S(\lambda_i, \lambda) = \mathrm{const} \cdot 2^{\left(\frac{\lambda_i - \lambda}{\mathrm{FWHM}/2}\right)^4} \tag{13}$$

The constant const normalizes the slit function to unit area. The spectral sampling interval is 0.10 nm.

A noise model associates simulated reflectance spectra with noise spectra. We assume that the measurement error is dominated by shot noise. Hence, the measurement error covariance matrix is diagonal and the signal-to-noise ratio (SNR) of the radiance L is proportional to the square root of the radiance (in photons). In addition, we assume the proportionality factor to be independent of wavelength. If we know the signal-to-noise ratio for some reference radiance level L^{ref} at some reference wavelength $\lambda_i{}^{\mathrm{ref}}$, we can thus calculate the signal-to-noise ratio for any other radiance level at any other wavelength following

$$\mathrm{SNR}(L(\lambda_i)) = \mathrm{SNR}(L^{\mathrm{ref}}(\lambda_i^{\mathrm{ref}})) \cdot \sqrt{\frac{L(\lambda_i)}{L^{\mathrm{ref}}(\lambda_i^{\mathrm{ref}})}}. \tag{14}$$

The signal-to-noise ratio at 758 nm (continuum) is 500 for a reference radiance L^{ref}(758 nm) of $4.5 \cdot 10^{12}$ photons s^{-1} cm^{-2} sr^{-1} nm^{-1} and for the spectral sampling interval of 0.1 nm. The reference radiance spectrum, which is used for specification of the SNR within the Sentinel-5 and Sentinel-5 Precursor projects, corresponds to a dark scene (‘tropical dark’, meaning a pure molecular atmosphere with a surface albedo of 0.02, a solar zenith angle of 0° and a viewing zenith angle of 0°). Hence, if clouds or aerosols are present, or if the surface albedo is larger than 0.02, the actual SNR will be (much) larger than 500. Finally, we assume the signal-to-noise ratio of the irradiance to be a factor of ten higher than the signal-to-noise ratio of the radiance. Note that we do not add noise to the radiance spectra nor do we apply by default any other instrumental effects.

The temperature profile in simulation and retrieval corresponds to the mid-latitude summer atmosphere, and the ground pressure is 1013 hPa. Oxygen has a constant volume mixing ratio of 21%. Oxygen absorption cross section parameters are taken from the HITRAN 2008 database [ER1]: a Voigt profile is assumed, only the most abundant isotopologue is taken into account, and line mixing and collision-induced absorptions are ignored. We consider the following surface types

Table 8: Surface types and corresponding albedos considered in the error analysis

Surface type	Surface albedo	
	758 nm	770 nm
Sea / ocean	0.025	0.025
Vegetated land	0.20	0.25
Desert / arid land	0.30	0.35
Snow / ice	0.6	0.6

These values are in agreement with Koelemeijer et al. (2003) [29]. Fluorescence emissions for vegetated land are zero. The pressure difference between top and bottom of an aerosol layer is 20 hPa in both simulation and retrieval. Hence, a mid pressure of, for example, 800 hPa corresponds to an aerosol layer with a top and bottom pressure of 790 hPa and 810 hPa, respectively. The default aerosol model in simulation and retrieval has a single scattering albedo of 0.95, a Henyey-Greenstein phase function with asymmetry parameter of 0.7 and an Angstrom coefficient of zero. Radiative transfer settings are as described in 5.4 (e.g. polarization is ignored in simulation and retrieval).

7.4 Baseline precision of Aerosol Layer Height

First we describe the baseline precision of retrieved mid pressure and we investigate its dependence on mid pressure, aerosol optical thickness, surface albedo and observation geometry. We also show that the inversion can be problematic for specific combinations of atmospheric state and observation geometry.

Approach

For a number of atmospheric states and observation geometries, we simulate reflectance spectra of the O_2 A band at TROPOMI's resolution and we calculate corresponding noise spectra according to TROPOMI's anticipated noise model. We then use the derivatives of reflectance provided by the forward model, to propagate the measurement noise and calculate 1-σ errors in fit parameters. The state vector contains the main fit parameters p_{mid}, τ_0, A_s (758 nm) and A_s (770 nm).

In symbols this can be expressed as follows. If the forward model is linearized around the (retrieved) state for the purposes of an error analysis, we write

$$\mathbf{R} \approx \mathbf{F}(\hat{\mathbf{x}}) + \mathbf{K}(\mathbf{x} - \hat{\mathbf{x}}), \tag{15}$$

where $\mathbf{R}$ is the vector of simulated measurements. The covariance matrix describing the error in retrieved parameters due to the measurement error in $\mathbf{R}$ follows from Eq. 8-3 using rules for error propagation:

$$\hat{\mathbf{S}} = \mathbf{K}\hat{\mathbf{S}}\mathbf{K}^T \Rightarrow \hat{\mathbf{S}} = (\mathbf{K}^T\mathbf{S}^{-1}\mathbf{K})^{-1}. \tag{16}$$

Note that a column of **K** corresponds to the derivative of reflectance with respect to a particular fit parameter as a function of wavelength (Eq. 10). If certain columns of **K** become strongly linearly dependent (i.e. spectral shapes of derivatives are similar), matrix is nearly singular. Errors in corresponding parameters (diagonal elements of) become large and it will be difficult to simultaneously fit these parameters with precision levels that meet scientific user requirements. In addition, the solution is sensitive to systematic errors, such as numerical inaccuracies, model biases or calibration errors (ill-conditioning).

We are not taking into account *a priori* information here, since our aim is to investigate precision levels that can be achieved by the measurement alone. The state vector used for the present analysis indeed contains all main fit parameters for which we in practice have little *a priori* knowledge available. If more fit parameters are added to the state vector, precision levels might deteriorate, depending on the respective *a priori* errors. In the remainder of the error analysis, we will describe how precision levels change in response to adding parameters to the state vector where appropriate. The results presented in this section thus provide a description of the algorithm's baseline precision.

Results

We simulated reflectance spectra for a large range of mid pressures, optical thicknesses, surface albedos and solar zenith angles (SZAs). We also tested a number of viewing zenith angles (VZAs) and relative azimuth angles (RAAs). We used the default aerosol model ω_0 of 0.95, HG phase function with asymmetry parameter of 0.7); the aerosol layer has a pressure thickness of 20 hPa. We summarize the main findings below.

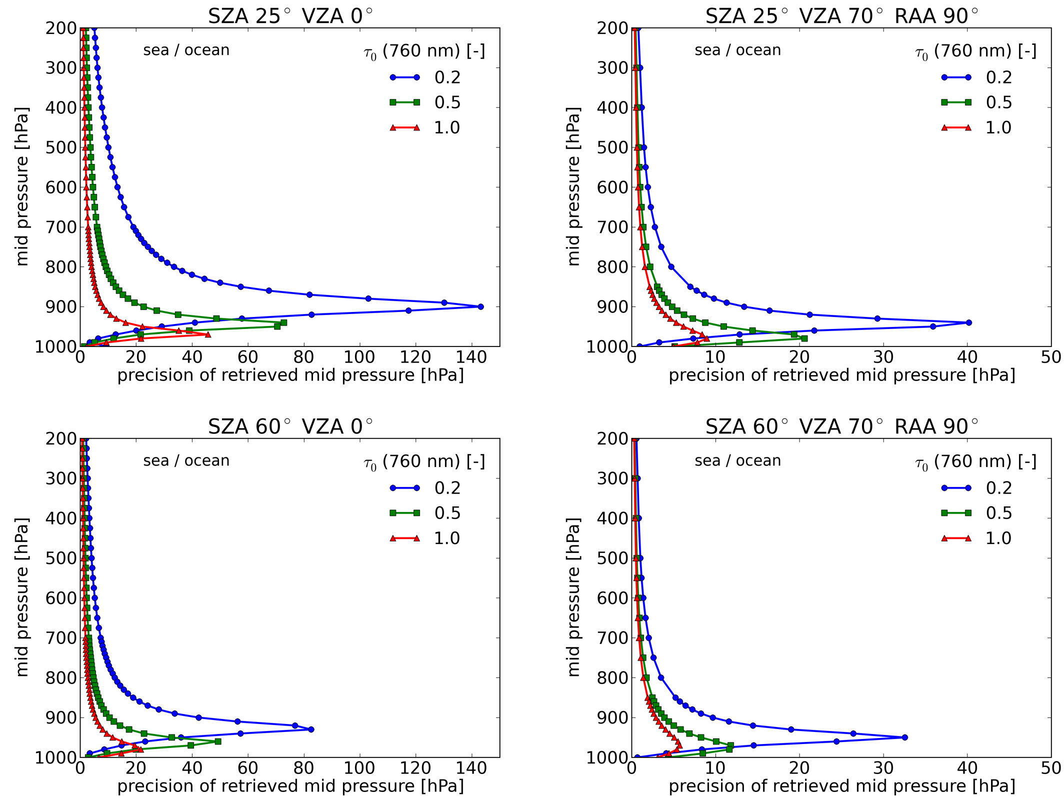

Figure 17: Precision of retrieved aerosol mid pressure as a function of mid pressure for three values of the aerosol optical thickness. Panel A shows retrieval precision for an aerosol layer over sea / ocean; Each of the four subplots in a panel corresponds to a different observation geometry: SZA 25°, VZA 0° (top left); SZA 25°, VZA 70°, RAA 90° (top right); SZA 60°, VZA 0° (bottom left); and SZA 60°, VZA 0°, RAA 90° (bottom right). Note the different scales of the x-axis.

Figures 17 and 18 illustrate the precision of retrieved mid pressure for four representative TROPOMI observation geometries. Every subplot of these figures shows precision of retrieved mid pressure as a function of mid pressure for three values of the aerosol optical thickness. Figures 17 corresponds to retrievals over sea / ocean and Figures 18 corresponds to vegetated land, respectively. The four subplots within a panel correspond to four different observation geometries: solar zenith angles of 25° and 60°, and viewing zenith angles corresponding to pixels at nadir (0°) and near the end of the swath (70°).

Overall, the figures show that the baseline precision is usually well below the TROPOMI target requirement of 50 hPa for optical thicknesses above 0.2. In incidental cases, however, precision may significantly deteriorate and increase up to 100 hPa or even above.

Precision of mid pressure generally improves with decreasing pressure (increasing altitude). At larger pressure differences between aerosol layer and ground surface, it is easier to distinguish aerosol contributions from surface contributions. Precision of mid pressure generally improves with increasing optical thickness (stronger aerosol signal). Note, however, that exceptions to these trends exist. There is no clear dependence of precision on the albedo of the surface.

Precision of mid pressure generally improves with increasing solar zenith angle. If the solar zenith angle increases, a unit area of surface receives less light (weaker aerosol signal) but path lengths through the aerosol layer are longer (stronger aerosol signal). Apparently, the latter effect dominates. Precision of mid pressure also tends to improve with increasing viewing zenith angle (longer path lengths through aerosol layer, hence stronger aerosol signal). As before, exceptions to these trends exist.

Figure 19 depicts precision of retrieved mid pressure as a function of surface albedo for three arbitrary atmospheric states and observation geometries. It illustrate once more that the inversion can become nearly singular for specific atmospheric states and observation geometries. Furthermore, aerosol retrieval is not more precise over darker (or brighter) surfaces in a general sense. This stands in contrast with conventional spectral aerosol optical thickness retrieval algorithms, which are typically less precise over land. Spectral

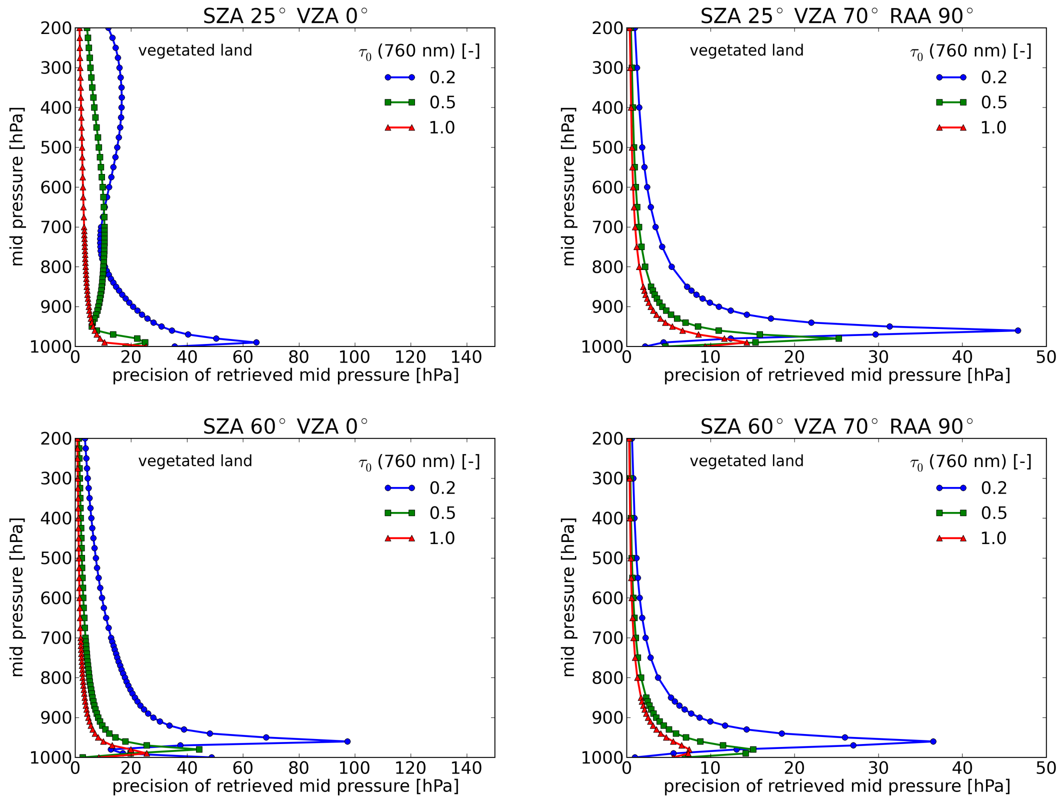

Figure 18: Precision of retrieved aerosol mid pressure as a function of mid pressure for three values of the aerosol optical thickness. Panel A shows retrieval precision for an aerosol layer over vegetated land. Each of the four subplots in a panel corresponds to a different observation geometry: SZA 25°, VZA 0° (top left); SZA 25°, VZA 70°, RAA 90° (top right); SZA 60°, VZA 0° (bottom left); and SZA 60°, VZA 0°, RAA 90° (bottom right). Note the different scales of the x-axis.

optical thickness retrievals using continuum reflectances rely heavily on external surface reflectance models or climatologies. Such reflectance models or climatologies are generally less accurate for land surfaces. Finally, it shows that it is very well possible to retrieve aerosol pressure over snow covered surfaces.

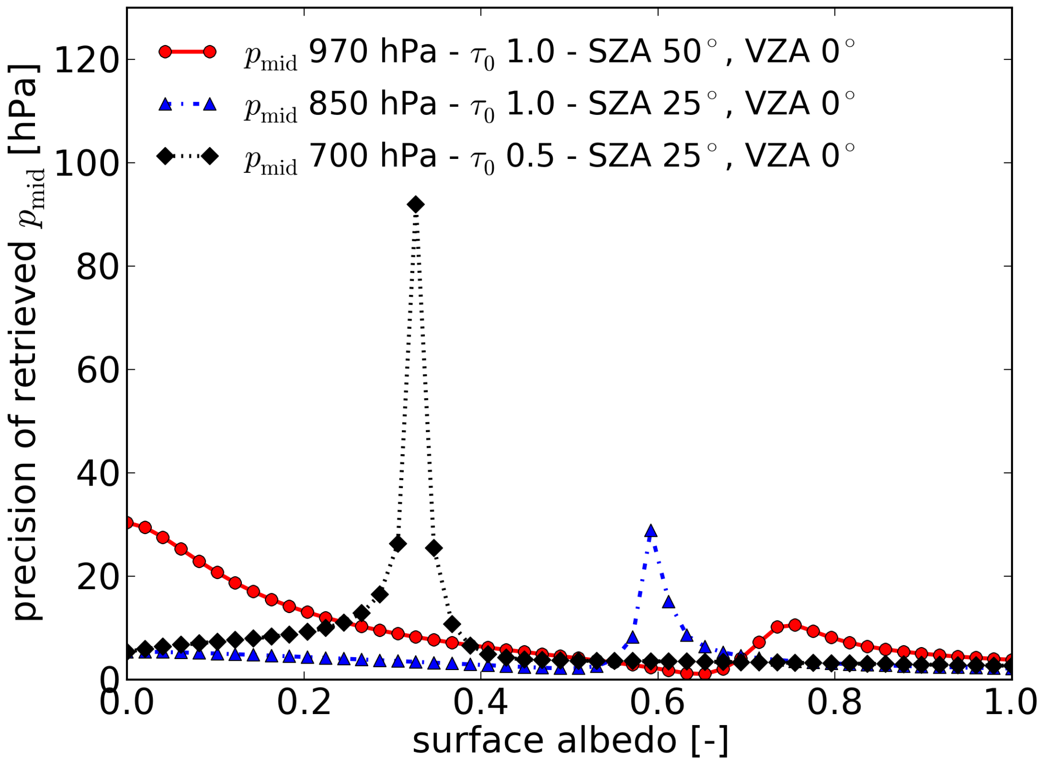

Figure 19: Precision of retrieved mid pressure as a function of surface albedo for three arbitrary atmospheric states and observation geometries.

Finally, we mention that errors in the fit parameters are usually highly correlated. To give an impression, Table 9 shows correlation coefficients between errors in all fit parameters for an aerosol layer with optical thickness of 0.5 at 800 hPa over sea / ocean and vegetated land. Although correlation coefficients can be as high as 0.999, precision of retrieved pressure is good (cf. Figures 17 and 18, bottom left plot). This conforms to the finding that the degrees of freedom for the signal for these two cases is 4.0, which is equal to the number of fit parameters. Thus, derivatives are still sufficiently linearly independent to retrieve all four parameters simultaneously. It is our experience from simulation studies that a retrieval with such high correlation coefficients is generally stable.

Table 9: Correlation coefficients between errors in fit parameters for an aerosol layer with optical thickness of 0.5 at 800 hPa over sea / ocean and vegetated land. The solar zenith angle is 60° and the viewing direction is nadir. The height variable is altitude (in km) instead of pressure (in hPa).

Correlation coefficient	Sea/Ocean	Vegetated land
$z_{\mathrm{mid}} - \tau_0$ (760 nm)	-0.9945	-0.9895
$z_{\mathrm{mid}} - A_{\mathrm{s}}$ (758 nm)	0.9929	0.9721
$z_{\mathrm{mid}} - A_{\mathrm{s}}$ (770 nm)	0.9937	0.9383
τ_0 (760 nm) – A_{s} (758 nm)	-0.9996	-0.9900
τ_0 (760 nm) – A_{s} (770 nm)	-0.9997	-0.9562
A_{s} (758 nm) – A_{s} (770 nm)	0.9991	0.9354

7.5 Convergence of retrieval and uniqueness of solution

Numerical experiments (see also Section 7.4) show that the cost function may sometimes be relatively flat or even have more than one local minimum (cf. Hollstein et al., 2012 [21], figure 19). If the cost function exhibits

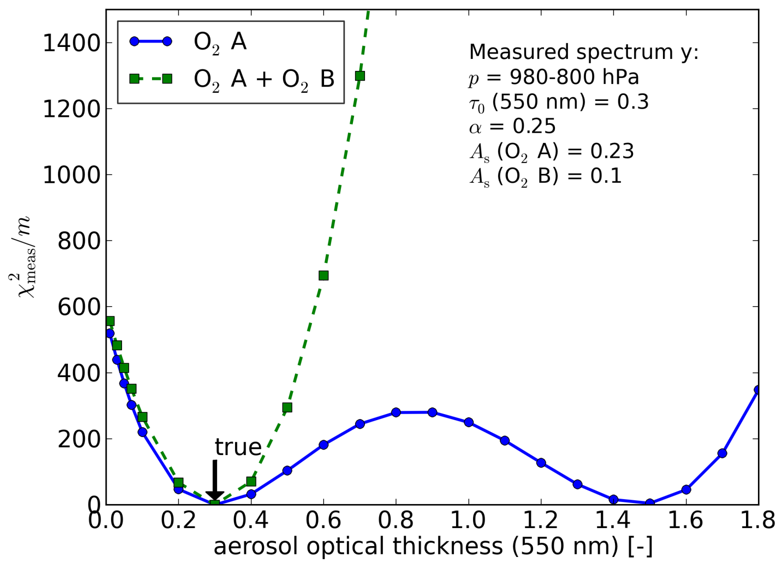

Figure 20: χ^2 of the (simulated) measurement (first term of Eq. 8) for an aerosol layer between 980 and 800 hPa with optical thickness of 0.3 at 550 nm over vegetated land. The measurement vector **y** includes the O_2 A band, or the O_2 A and B bands. Note that the surface is much brighter in the O_2 A band. The modeled spectrum **F**(**x**) differs from the measurement with respect to optical thickness. One can clearly see multiple minima in the cost function if only the O_2 A band is taken into account.

multiple minima, the solution obtained depends on the initial values and might be a wrong local minimum. A sensitivity analysis indicated that the convergence rate improves if in retrieval purely scattering aerosols (as opposed to partly absorbing aerosol, e.g. SSA of 0.95) were assumed. Local χ^2-minima, particularly for land scenes, may be removed by including the O_2 B band in the measurement vector (Figure 20).

7.6 Required knowledge of aerosol type

Retrieval of aerosol pressure from the O_2 A band requires an assumed aerosol model, because the measurement does not contain enough information to simultaneously retrieve aerosol optical properties. However, the aerosol type present in the target pixel is generally unknown and shows a large variation in time and space. In this section, we show that biases in retrieved aerosol pressure generally remain small in response to model errors in the single scattering albedo and phase function. Biases in retrieved aerosol optical thickness on the other hand are significant.

7.6.1 Single scattering albedo

Approach

First we investigate the sensitivity of retrieval to model errors in the single scattering albedo. We simulate reflectance spectra for a range of optical thicknesses and for a number of single scattering albedos, mid pressures and surface albedos. We then retrieve aerosol mid pressure assuming in retrieval a single scattering albedo of 0.95. The forward models for simulation and retrieval are the same, except for this model error in the single scattering albedo. The state vector contains the main fit parameters p_{mid}, τ_0, A_s (758 nm) and A_s (770 nm).

Results

We discuss a set of representative retrieval results. True values, *a priori* values and *a priori* errors for the fit parameters are given in Table 10. The single scattering albedo in the simulation is either 0.9 or 1.0. In both simulation and retrieval we have a single aerosol layer with a pressure thickness of 20 hPa and a Henyey-Greenstein phase function with asymmetry parameter of 0.7. The solar zenith angle is 50° and the viewing direction is nadir.

Table 10: True values, *a priori* values and *a priori* errors used in the retrieval simulations of Figure 18 investigating the sensitivity of retrieval to the assumed single scattering albedo.

Fit parameter	True value	AP value	AP error (1-σ)
p_{mid}	600 hPa 800 hPa	True	500 hPa
τ_0 (760 nm)	Range: 0.025 – 1.0	True	2.0
A_s (758 nm)-A_s (770 nm)	0.025 – 0.025 0.0 – 0.25 (vegetated land)	True	0.2

Figure 21 shows the results from these retrievals. The left and right panels correspond to the two surface albedos. We show the bias in retrieved mid pressure (first row), precision of retrieved mid pressure (second row), and the bias in retrieved optical thickness with precision indicated by error bars (third row). Note that the *x*-axis has a logarithmic scale.

One would perhaps expect retrieved aerosol parameters to be inaccurate in case of a model error in the single scattering albedo. However, we see that biases in retrieved pressure are typically very small compared to the TROPOMI target requirement on accuracy of 50 hPa. Moreover, biases tend to decrease for optically thicker aerosol layers (stronger aerosol signal). On the other hand, we see that retrieved optical thickness is biased significantly and so is retrieved surface albedo (not shown). These two fit parameters respond to a model error in the singe scattering albedo. Indeed, biases in retrieved optical thickness and surface albedo increase with increasing aerosol optical thickness.

For the vegetated land case (panel B), we see that pressure biases rapidly increase up to and sometimes even above 50 hPa in a small range of optical thicknesses between 0.1 and 0.2 and particularly for the near-surface aerosol layer. This result is not so much illustrative of the effect of a model error in the single scattering albedo. Rather, as indicated by the poor precision levels in this range, spectral shapes of the derivatives are similar and the inversion is sensitive to any model error.

A model error of 0.05 in the single scattering albedo is used to represent a typical *a priori* uncertainty. However, we have tested model errors up to 0.2 (e.g. single scattering albedo of 0.6 in the simulation and 0.8 in retrieval). Even for such a large error, the conclusions stated above hold. Hence, retrieved aerosol pressure is robust against inaccurate knowledge of the single scattering albedo. In Section 7.7 we show that it is essential in this respect that surface albedo, next to aerosol optical thickness, is a fit parameter.

We have repeated these retrieval simulations and fitted the single scattering albedo with an *a priori* error of 0.05. Overall, precision of retrieved aerosol pressure remains the same but precision of retrieved aerosol optical thickness deteriorates. In addition, we find that biases in both retrieved pressure and optical thickness remain the same. Thus, retrieval does neither improve nor deteriorate with respect to aerosol pressure when fitting the single scattering albedo. However, these preliminary investigations also indicate that the near-singular behavior for the aerosol layer with optical thickness between 0.1 and 0.2 over vegetated land is mitigated.

Fitting the single scattering albedo is implemented as an option to the baseline algorithm. Perhaps fitting the single scattering albedo will improve retrieval of aerosol optical thickness for optically thick aerosol layers (optical thickness larger than, say, 1.0).

7.6.2 Phase function

Approach

Second we investigate the sensitivity of the retrieval to model errors in the phase function. We simulate reflectance spectra using generic aerosol models that are used within the framework of the aerosol project in ESA's Climate Change Initiative program [ER3]. We test three somewhat realistic atmospheric scenarios for a range of optical thicknesses and for a number of aerosol pressures. The three scenarios are based on the 'Dust', 'Fine mode weakly absorbing' and 'Fine mode strongly absorbing' aerosol models [12]. The fourth aerosol model, 'Sea salt', is not considered here. For one scenario we retrieve top pressure instead of mid pressure, following the parameterization described in section 5.2.4.6 and illustrated in Figure9C. In retrieval we assume the Henyey-Greenstein phase function with asymmetry parameter of 0.7. To isolate the effect of a model error in the phase function, the single scattering albedo assumed in retrieval is equal to the true value. The state vector contains the main fit parameters p_{mid}, τ_0, A_s (758 nm) and A_s (770 nm).

Results

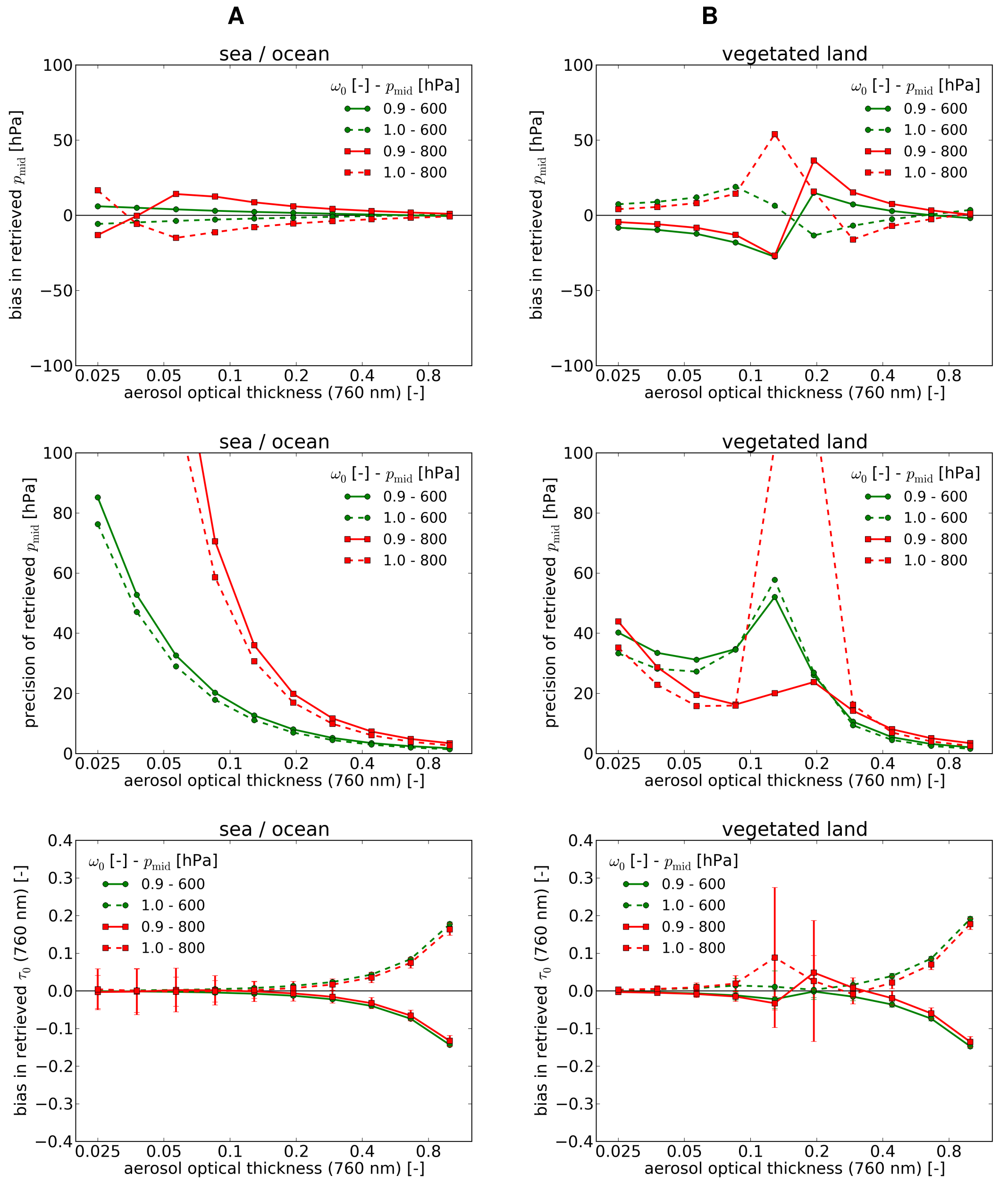

Figure 21: Effect of a model error in the single scattering albedo on retrieved mid pressure and aerosol optical thickness as a function of optical thickness. We assume a single scattering albedo of 0.95 in retrieval, while the true single scattering albedo is either 0.90 (solid lines) or 1.0 (dashed lines). The aerosol layer is located at 600 hPa (green lines) or 800 hPa (red lines). First row: bias in retrieved mid pressure; second row: precision of retrieved mid pressure; third row: bias in retrieved optical thickness with error bars indicating precision. Panel A (left column) shows retrieval simulations over sea / ocean; panel B (right column) shows retrieval simulations over vegetated land. The x-axis has a logarithmic scale.

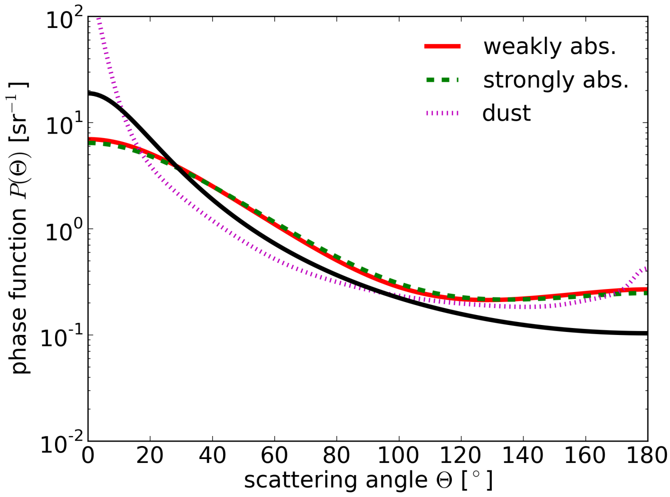

Figure 22: Phase functions for the three aerosol models used in the retrieval simulations of Figure 23. The black line corresponds to a Henyey-Greenstein phase function with asymmetry parameter of 0.7, which is used in retrieval.

Optical properties for the three aerosol models are summarized in Table 11. Figure 22 makes a comparison of the phase functions used in simulation and retrieval. The three atmospheric scenarios, and true values, *a priori* values and *a priori* errors for the fit parameters are given in Table 12. For the first two scenarios the profile consists of a single aerosol layer with a pressure thickness of 20 hPa and we are retrieving mid pressure. For the Boundary layer pollution scenario, the aerosol layer extends down to the ground surface and we are retrieving the top pressure of the aerosol layer. The solar zenith angle is 50° and the viewing direction is nadir.

Table 11: Optical properties at the O_2 A band for the three aerosol models used in the retrieval simulations of Figure 23 (based on [12]). Properties for the Dust model are based on T-matrix calculations, which are kindly provided by Oleg Dubovik and co-workers; for the other two models we performed Mie calculations.

Aerosol model	**Single scattering albedo (760 nm)**	**Asymmetry parameter**	**Normalized extinction cross section at 760 nm (w.r.t. 550 nm)**
Dust	0.97	0.71	1.05
Fine mode strongly absorbing	0.76	0.57	0.57
Fine mode weakly absorbing	0.97	0.58	0.50

Table 12: True values, *a priori* values and *a priori* errors used in the retrieval simulations of Figure 23 investigating the sensitivity of retrieval to the assumed phase function.

Scenario	Fit parameter	True value	AP value	AP error (1-σ)
'Dust over ocean'	p_{mid}	600 hPa 750 hPa 850 hPa	True	500 hPa
	τ_0(550 nm)	Range: 0.05–2.0	True	2.0
	A_s (758 nm)-A_s (770 nm)	0.025 – 0.025	True	0.2
'Biomass burning over ocean'	p_{mid}	600 hPa 750 hPa 850 hPa	True	500 hPa
	τ_0(550 nm)	Range: 0.05–2.0	True	2.0
	A_s (758 nm)-A_s (770 nm)	0.20 – 0.25 (vegetated land)	True	0.2
'Boundary layer pollution'	p_{top}	850 hPa 900 hPa 950 hPa	True	500 hPa
	τ_0(550 nm)	Range: 0.05–2.0	True	2.0
	A_s (758 nm)-A_s (770 nm)	0.20 – 0.25 (vegetated land)	True	0.2

Figure 23 shows the results from these retrievals. Each panel corresponds to one of the three scenarios. We show the bias in retrieved aerosol pressure (left) and precision of retrieved pressure (right). Note that the *x*-axis has a logarithmic scale. We remark that the effect of a model error in the phase function depends on (interactions between) the observation geometry, aerosol parameters and surface albedo. This effect is harder to generalize from a limited set of retrieval simulations than the effect of a model error in the single scattering albedo.

For the 'Dust over ocean' scenario (panel A), we see that the effect of a model error in the phase function on retrieved pressure is small, even though the phase function for the coarse mode aerosol differs most pronouncedly from the Henyey-Greenstein function (particularly in the forward scattering direction). The inversion for dark surfaces (e.g. sea / ocean) is generally well conditioned. These retrieval simulations then suggest that aerosol pressure retrieval over a dark surface is robust against inaccurate knowledge of the phase function.

The retrieval simulations for the 'Biomass burning over land' scenario (panel B) are more difficult to interpret, because the inversion is nearly singular for optical thicknesses at 550 nm between about 0.2 and 0.3. Precision is poor and retrieval is sensitive to model errors in that range. However, for optical thicknesses at 550 nm above 0.4, biases in retrieved mid pressure due to the model error in the phase function, are much smaller than the target requirement of 50 hPa. Retrieved aerosol optical thickness is biased significantly (not shown).

At first sight, the retrieval simulations for the 'Boundary layer pollution' scenario (panel C) seem to have similar results. Biases in retrieved top pressure increase in a range of optical thicknesses (around 0.8) for two out of three aerosol top pressures. However, precision of retrieved pressure in this range is good and well below the target requirement of 50 hPa. For optical thicknesses at 550 nm above around 1.3, biases in retrieved pressure are small, but biases in retrieved aerosol optical thickness are significant (not shown).

7.6.3 Conclusion

The retrieval simulations presented in this section indicate that retrieved aerosol pressure is robust to model errors in the single scattering albedo. They also suggest that retrieved aerosol pressure is robust to a model error in the phase function, particularly over dark surfaces (e.g. sea / ocean). The operational algorithm will therefore initially assume a single, average aerosol model.

We have also shown that aerosol retrieval over relatively bright land (e.g. vegetated land) can be problematic. Since vegetated land is much darker at the O_2 B band around 685 nm (the O_2 A and B bands are located on opposite sides of the so-called red-edge; e.g. [29]), including the O_2 B band in the fit may help to mitigate or remove near-singularities for vegetated land cases. Retrieval of aerosol pressure over land needs to be further investigated.

We prefer to assume a phase function in retrieval that is smooth and can serve as an approximate phase function for many aerosol types. A smooth phase function is advantageous because radiative transfer calculations are faster (less streams needed).

7.7 Role of *a priori* knowledge of the surface albedo

A surface albedo climatology, such as the MERIS BSA database [39], can provide model or *a priori* values for the surface albedo in retrieval. In this section, we show that the typical uncertainties associated with climatological values make it sometimes problematic to treat the surface albedo as a model parameter: large pressure biases and non-convergent retrievals occur. On the other hand, biases and non-convergences disappear if the surface albedo is included in the state vector. We also show that imposing a small *a priori* error in the surface albedo corresponding to the uncertainty in climatological values, does not improve precision of retrieved pressure.

Before presenting the sensitivity analysis, we first illustrate in Figure 24 that the surface albedo and aerosol optical thickness can be retrieved simultaneously from the O_2 A band. The figure shows reflectance spectra for two different combinations of optical thickness and surface albedo that yield the same reflectance in the continuum. All other parameters, including the aerosol pressure, are the same. The two cases can be distinguished from the shape of absorption: photons reflected by the surface have to pass through the atmosphere below the aerosol layer, in which additional oxygen absorption takes place.

Approach

We investigate the effect on retrieval if the true surface albedo differs from the value provided by a surface albedo climatology. We compare three types of retrieval: the surface albedo being a model parameter, the surface albedo being fitted in a retrieval constrained by the climatology, and the surface albedo being fitted in an unconstrained retrieval. These three retrieval types are summarized in Table 13. We investigate a sea / ocean case and a vegetated land case and assume that the typical random (1-σ) error in climatological albedo values is 0.01 and 0.02, respectively. (Thus, events such as incidental snow cover are not incorporated.) For simplicity, we assume in this sensitivity analysis that the surface albedo is wavelength independent. The state vector contains parameters p_{mid}, τ_0, and A_s.

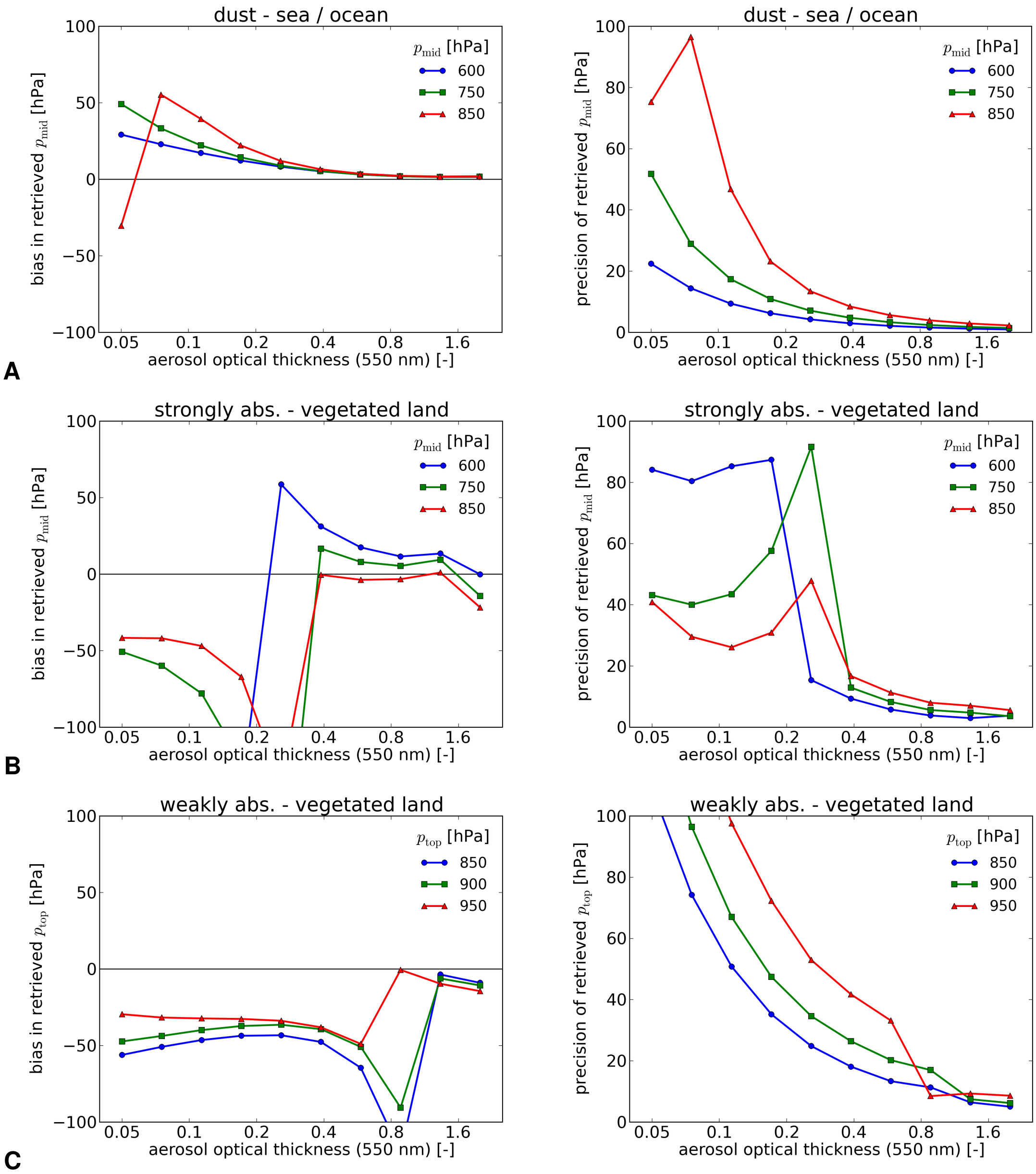

Figure 23: Effect of a model error in the phase function on retrieved aerosol pressure as a function of optical thickness for three values of aerosol pressure. Panel A (first row): 'Dust over ocean'; panel B (second row): 'Biomass burning over land'; panel C (third row): 'Boundary layer pollution'. For details of these scenarios, see the text and Table 12. In each panel, the left plot shows the bias in retrieved aerosol pressure and the right plot shows precision of retrieved pressure. We assume a Henyey-Greenstein phase function with asymmetry parameter of 0.7 in retrieval. Note that for the 'Boundary layer pollution' scenario, we assume an aerosol profile consisting of a single layer extending down to the ground surface. In this case, we retrieve the layer's top pressure p_{top}. The x-axis has a logarithmic scale.

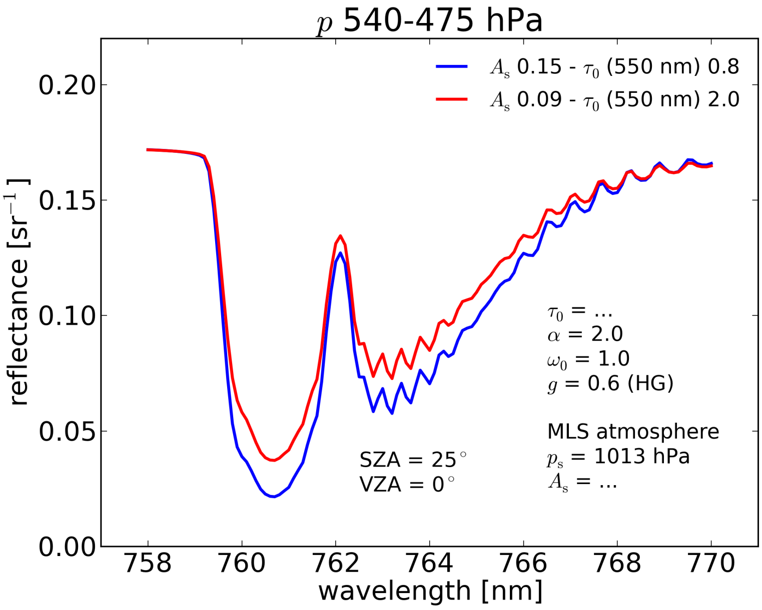

Figure 24: Reflectance spectra for two different combinations of optical thickness and surface albedo that yield the same continuum reflectance. All other parameters are the same. The aerosol layer is between 540 and 475 hPa; the single scattering albedo is 1.0; the solar zenith angle is 25° and the viewing direction is nadir. From the shape of absorption we can simultaneously fit surface albedo and aerosol optical thickness.

Table 13: *A* priori error in the surface albedo for the three types of retrieval investigating the effect of an error in climatological surface albedo values.

Retrieval type	**AP error (1-σ) in A_s**	**Comment**
'No fit A_s (σ=0.0)'	0.0	Surface albedo is a model parameter: the model value is provided by the surface albedo climatology
'Fit A_s (σ=0.01)' 'Fit A_s (σ=0.02)'	0.01 (sea/ocean) 0.02 (vegetated land)	Surface albedo is a fit parameter: the *a priori* value is provided by the surface albedo climatology and the *a priori* error is the random error associated with the climatological value
'Fit A_s (σ=0.2)'	0.2	Surface albedo is a fit parameter: measurement determines surface albedo (large *a priori* error); climatology provides starting value for the fit

Results We have tested a number of atmospheric scenarios, but show results for only two of them. The results for these scenarios are representative of all the other scenarios. Atmospheric scenarios and associated *a priori* values and errors are given in Table 14. We vary the true surface albedo within 3ω around the climatological value. In both simulation and retrieval, the aerosol layer's pressure thickness and the aerosol model have default values. The solar zenith angle is 50° and the viewing direction is nadir.

Table 14: True values, *a priori* values and *a priori* errors used in the retrieval simulations of Figure 25 investigating the sensitivity of retrieval to the assumed phase function.

Fit parameter	True value	AP value	AP error (1-σ)
p_{mid}	500 hPa 800 hPa	True	500 hPa
τ_0(760 nm)	0.2 0.5 1.0	True	2.0
A_s (760 nm)	Range: 0.025 $\pm$ 3*0.01 (sea/ocean) Range: 0.02 $\pm$ 3*0.02 (vegetated land)	0.025 0.2	Three cases: see table 8-6

Figure 25 shows results for an aerosol layer with optical thickness of 0.5 at 500 hPa over sea / ocean (panel A) and an aerosol layer with optical thickness of 0.5 at 800 hPa over vegetated land (panel B). We show the bias in retrieved aerosol pressure (left) and precision of retrieved pressure (right) as a function of the true surface albedo for each of the three retrieval types. The climatological surface albedo value that is used in retrieval (either as model value, *a priori* value or starting value), is indicated by the arrow. Missing data points indicate that retrieval does not converge.

If the surface albedo is not fitted, non-convergences and pressure biases much larger than 50 hPa occur. For example, if the true surface albedo is 0.21 while a value of 0.20 is assumed in retrieval, the aerosol layer at 800 hPa over vegetated land shows a pressure bias of 94 hPa. If the true surface albedo is 0.19, retrieval for that layer does not even converge. Note that these deviations of the true surface albedo from the model value are representative of current surface albedo climatologies. On the other hand, if the surface albedo is fitted, the non-convergent retrievals and pressure biases disappear.

Precision of retrieved pressure is the same when fitting the surface albedo with an *a priori* error corresponding to the climatological uncertainty, or when fitting the surface albedo with a relatively large *a priori* error of 0.2. This indicates that the information about the surface reflectivity contained in the measurement is so pronounced that the *a priori* information provided by a surface albedo climatology does not constrain retrieval.

So far we have focused on the question whether a surface albedo climatology improves (a posteriori) precision of retrieved pressure. However, a surface albedo climatology can also help to stabilize retrieval by providing starting values for the iterative fit procedure. The outcome of an iterative fit is particularly sensitive to the starting value in case of highly non-linear forward models or multiple minima in the cost function. A surface albedo climatology can provide starting values for the fit that are supposedly closer to the surface albedo's true values. If starting values of fit parameters are closer to their true values, the convergence rate may improve, the number of iterations may be reduced, or retrieval may more often converge to the correct (global) χ^2-minimum.

The stability of retrieval is difficult to assess in a simulation environment. However, we have done extensive experiments with GOME-2 spectra [46] so far we found that the retrieval is considerably stable. For example, for a set of 1844 SCIAMACHY pixels over sea with high UVAI values, 1835 pixels had a converging retrieval after the first attempt (the starting values were the default, constant values). We also saw in these case studies that repeated retrieval attempts with different starting values does not improve convergence substantially.

7.8 Fitting surface albedo to compensate errors in single scattering albedo

In Section 8.3 we have shown that retrieved aerosol pressure is a robust quantity with respect to the assumed single scattering albedo but retrieved aerosol optical thickness and surface albedo are not. In Section 8.4 we have discussed the various ways to treat the surface albedo in retrieval with respect to the available surface albedo climatology (Table 13). We have shown that retrieval of aerosol pressure is sometimes problematic when not fitting the surface albedo in view of anticipated uncertainties in climatological albedo values. In this section, we return to the question of the effect of model errors in the single scattering albedo on retrieval and argue that the surface albedo should be included in the state vector for yet another reason.

The purpose of this section is to show that in order for retrieved pressure to be robust against inaccurate knowledge of the single scattering albedo it actually helps when the surface albedo is a fit parameter. Simultaneously fitting aerosol optical thickness as well as the surface albedo compensates for a model error in the single scattering albedo.

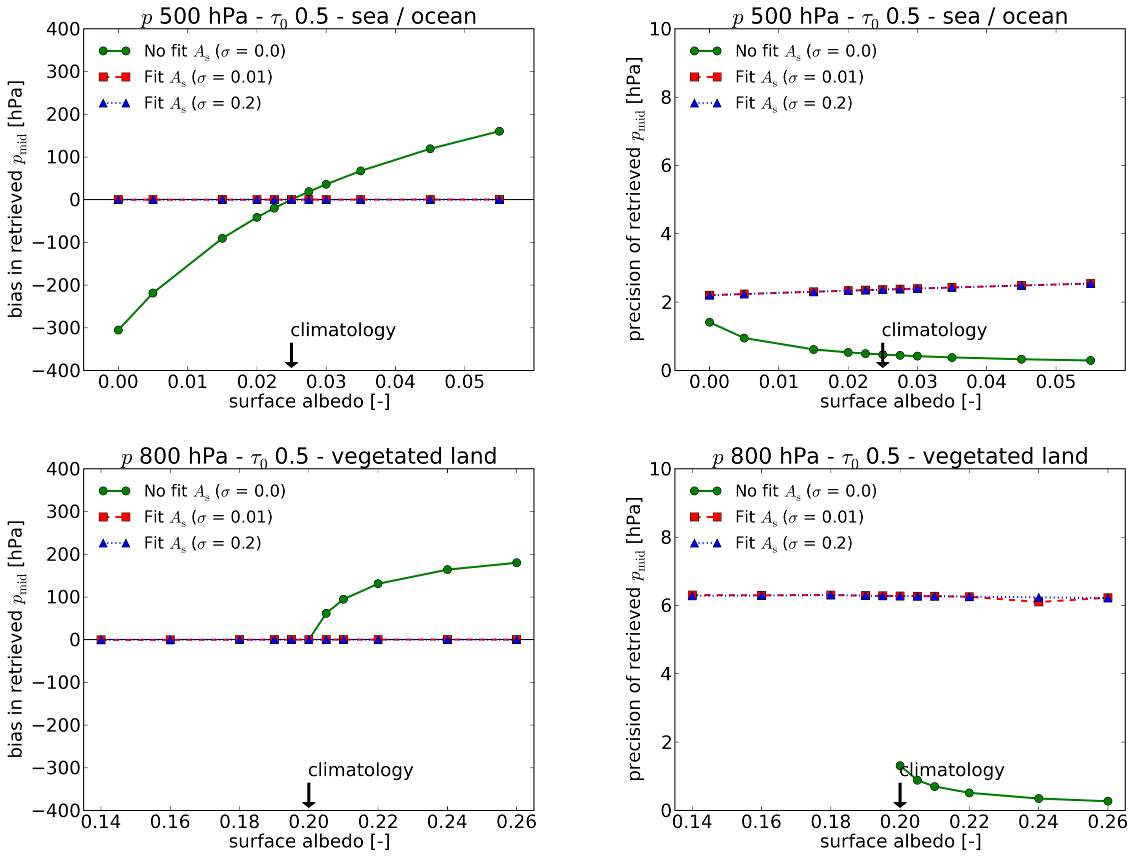

Figure 25: Effect of an error in climatological albedo values on retrieved aerosol pressure as a function of the true surface albedo for three retrieval types (Table 13). Panel A (first row): aerosol layer with optical thickness of 0.5 at 500 hPa over sea / ocean; panel B (second row): aerosol layer with optical thickness of 0.5 at 800 hPa over vegetated land. In each panel, the left plot shows the bias in retrieved aerosol pressure and the right plot shows precision of retrieved pressure. The climatological surface albedo value, which is used in retrieval, is indicated by the arrow. Missing data points indicate that retrieval does not converge.

Approach

We again investigate the effect on retrieval of a model error in the single scattering albedo, but this time we compare the three retrieval types of Table 13. The retrieval type in which the surface albedo is fitted in an unconstrained retrieval (‘Fit A_s (ω = 0.2)’) corresponds to the retrieval simulations of Section 8.3. The single scattering albedo assumed in retrieval is 0.95; the true single scattering albedo varies in a wide range between 0.80 and 1.0. For simplicity, we assume that the surface albedo is wavelength independent. The state vector contains parameters p_{mid}, τ_0, and A_s.

Results

The atmospheric scenarios and retrieval settings are the same as in the previous section (Table 14), except for the true surface albedo, which is not varied but equal to its climatological (a priori) value. We show results for two scenarios, which are representative of all the other scenarios. The solar zenith angle is 50° and the viewing direction is nadir.

Figure 26 shows the pressure bias as a function of the true single scattering albedo for an aerosol layer with optical thickness of 0.5 at 500 hPa over sea / ocean (left plot) and an aerosol layer with optical thickness of 0.5 at 800 hPa over vegetated land (right plot). The single scattering albedo assumed in retrieval is 0.95. Missing data points indicate that retrieval does not converge.

If the surface albedo is not fitted, non-convergences and pressure biases much larger than 50 hPa occur. For example, if the true single scattering albedo is 1.0 while a value of 0.95 is assumed in retrieval, the aerosol layer at 800 hPa over vegetated land shows a pressure bias of 119 hPa. If the true single scattering albedo is 0.90, retrieval for that layer does not even converge. On the other hand, if the single scattering albedo is fitted, the non-convergent retrievals disappear and pressure biases become very small. As mentioned before,

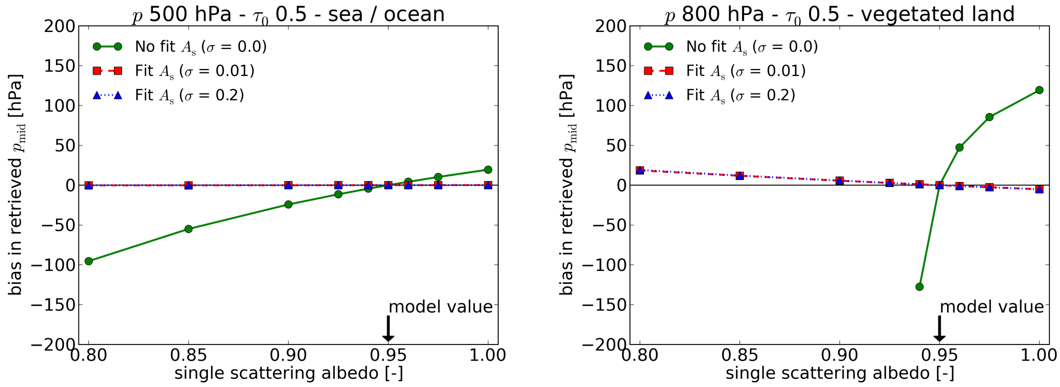

Figure 26: Effect of a model error in the single scattering albedo on the bias in retrieved pressure as a function of the true single scattering albedo for three retrieval types (Table 13). The single scattering albedo assumed in retrieval is 0.95. Left: aerosol layer with optical thickness of 0.5 at 500 hPa over sea / ocean; right: aerosol layer with optical thickness of 0.5 at 800 hPa over vegetated land. Missing data points indicate that retrieval does not converge.

retrieved aerosol optical thickness and surface albedo are biased (not shown).

Since fitting the surface albedo can compensate for typical model errors in the single scattering albedo, it is important to check whether the *a priori* error in the surface albedo is sufficiently large in this respect. The surface albedo should have enough flexibility to deviate from its true value in order to respond to model errors in aerosol optical properties. We find that even with *a priori* errors as small as 0.01 to 0.02, the retrieval can accommodate model errors in the single scattering albedo.

We have only investigated the effect of a model error in the single scattering albedo here, but we expect the conclusions stated above to also hold for model errors in the phase function.

7.9 Effect of uncertainty in *a priori* meteorological data

Temperature profiles and surface pressures are input data for the Aerosol Layer Height algorithm and they are provided by ECMWF. The purpose of this section is to show that if the temperature profile or surface pressure is not fitted, the expected uncertainties in meteorological input data can cause significant biases in retrieved aerosol pressure. On the other hand, if we include the temperature profile or surface pressure in the state vector with *a priori* errors corresponding to these expected uncertainties, we find that the decrease of precision of retrieved aerosol pressure is negligible (temperature profile) or limited (surface pressure).

7.9.1 Temperature profile

Approach

We assume that for the stable meteorological conditions that are targeted by the ALH algorithm (cloud-free pixels), a representative temperature error is 1-2 K for temperature profiles on a 1° by 1° grid. If the temperature profile is incorrect, biases in the number density and oxygen absorption cross section propagate into aerosol pressure biases.

We first investigate the effect of a temperature error on retrieved aerosol pressure by adding a temperature offset of 1, 2.5 or 5 K to the mid-latitude summer profile in the simulation while not fitting the temperature profile in retrieval. Next, we investigate retrieval precision when varying the *a priori* error in the temperature profile between 0 and 5 K. We assume a correlation length of 6 km for the *a priori* errors (i.e. starting with perfectly correlated *a priori* errors for adjacent levels the correlation coefficient drops off by a factor 1/e every 6 km). The state vector then contains fit parameters p_{mid}, τ_0, A_s(758 nm) and A_s (770 nm) in the first case, while $T(p_i)$ is added in the second case.

Results

We simulated reflectance spectra for two aerosol mid pressures (800 and 500 hPa), two aerosol optical thicknesses (0.2 and 0.5) and two surface albedos (sea / ocean and vegetated land); *a priori* errors are the usual 500 hPa, 2.0 and 0.20, respectively. The solar zenith angle is 50° and the viewing direction is nadir.

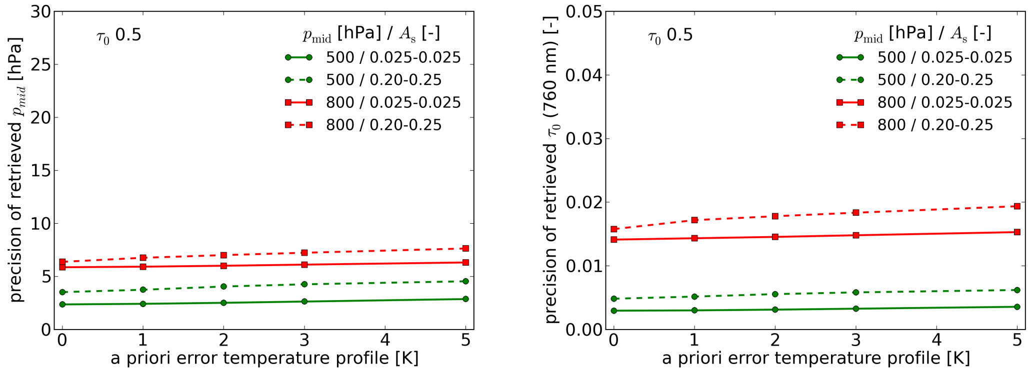

Figure 27: Precision of retrieved aerosol pressure (left plot) and optical thickness (right plot) as a function of the *a priori* error in the temperature profile. The aerosol layer has optical thickness of 0.5 and is located at 500 hPa (green lines) or 800 hPa (red lines), over sea / ocean (solid lines) or vegetated land (dashed lines). Retrieval precision shows the same behavior if the optical thickness is 0.2.

Table 15 gives retrieved aerosol mid pressures for every atmospheric scenario and for a temperature offset of 1 K if the temperature profile is not fitted. We have also tested offsets of 2.5 and 5 K, and found that pressure biases scale linearly with the temperature offset in this range (sometimes retrieval does not converge). In case of an offset of 1 K, pressure biases are of the order of a few hPa for retrievals over sea, but they increase up to 83 hPa for the aerosol layer with optical thickness of 0.2 at 800 hPa over vegetated land.

Table 15: Retrieved aerosol pressures for a number of atmospheric scenarios when an offset of 1 K is applied to the mid-latitude summer temperature profile in the simulation.

Surface albedo: A_s(758 nm)–A_s(770 nm)	Aerosol optical thickness: τ_0	Aerosol pressure: p_{mid}	Pressure bias: retrieved - true
0.025–0.025 (sea/ocean)	0.2	800 hPa	*+8 hPa*
		500 hPa	*-2 hPa*
	0.5	800 hPa	*+3 hPa*
		500 hPa	*-2 hPa*
0.2–0.25 (vegetated land)	0.2	800 hPa	*+83 hPa*
		500 hPa	*-33 hPa*
	0.5	800 hPa	*+20 hPa*
		500 hPa	*+3 hPa*

Figure 27 shows precision of retrieved aerosol pressure and optical thickness as a function of the *a priori* error in the temperature profile $T(p_i)$ for an aerosol layer with optical thickness of 0.5. The aerosol layer was at 500 or 800 hPa and over sea / ocean or vegetated land. We find that the deterioration of retrieval precision for these two parameters is negligible if the *a priori* error is increased from 0 K (temperature profile not fitted) up to 5 K. Note that we expect the uncertainty in ECMWF meteorological data to be smaller than (a 1-σ error of) 5 K. We have also verified that the pressure biases reported in Table 15 now disappear. Hence, fitting the temperature profile with an *a priori* value provided by ECMWF and a corresponding *a priori* error avoids the pressure biases described above while precision of retrieved aerosol pressure is retained.

7.9.2 Surface pressure

Approach

Salstein et al. (2008) report root-mean-square differences of 2-3 hPa between ground station observations and spatiotemporally interpolated 6-hourly 1° by 1° ECMWF surface pressures from operational analysis fields. These differences tend to be somewhat larger for high latitude and high topography regions. We take this value as a starting point for a sensitivity analysis of the effect of an error in the surface pressure.

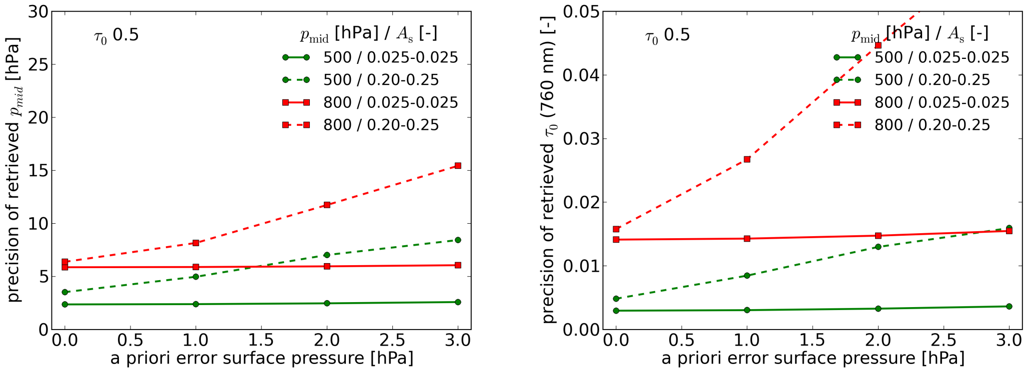

Figure 28: Precision of retrieved aerosol pressure (left plot) and optical thickness (right plot) as a function of the *a priori* error in the surface pressure. The aerosol layer has optical thickness of 0.5 and is located at 500 hPa (green lines) or 800 hPa (red lines), over sea / ocean (solid lines) or vegetated land (dashed lines). Retrieval precision shows the same behavior if the optical thickness is 0.2.

For the same atmospheric scenarios we first investigate the effect of a model error in the surface pressure by decreasing the true surface pressure by 2 and 4 hPa compared to the value of 1013 hPa assumed in retrieval. Next, we investigate retrieval precision when varying the *a priori* error in the surface pressure between 0 and 3 hPa. The state vector then contains fit parameters p_{mid}, τ_0, A_s (758 nm) and A_s (770 nm) in the first case, while P_s is added in the second case.

Results

We simulated reflectance spectra for two aerosol mid pressures (800 and 500 hPa), two aerosol optical thicknesses (0.2 and 0.5) and two surface albedos (sea / ocean and vegetated land); *a priori* errors are the usual 500 hPa, 2.0 and 0.20, respectively. The solar zenith angle is 50^{circ} and the viewing direction is nadir.

Table 16 gives retrieved aerosol mid pressures for every atmospheric scenario when there is a model bias of 2 hPa in the surface pressure. We have also tested a model bias of 4 hPa and found that pressure biases double (sometimes retrieval does not converge). In case of a model bias of 2 hPa, pressure biases are of the order of a few hPa for retrievals over sea, but they increase up to 56 hPa for the aerosol layer with optical thickness of 0.2 at 800 hPa over vegetated land.

Table 16: Retrieved aerosol pressures for a number of atmospheric scenarios when the true surface pressure is 1011 hPa while the surface pressure assumed in retrieval is 1013 hPa.

Surface albedo: A_s(758 nm)–A_s(770 nm)	**Aerosol optical thickness: τ_0**	**Aerosol pressure: p_{mid}**	**Pressure bias: retrieved - true**
0.025–0.025 (sea/ocean)	0.2	800 hPa	*+4 hPa*
		500 hPa	*+2 hPa*
	0.5	800 hPa	*+1 hPa*
		500 hPa	*+1 hPa*
0.2–0.25 (vegetated land)	0.2	800 hPa	*+56 hPa*
		500 hPa	*+43 hPa*
	0.5	800 hPa	*+10 hPa*
		500 hPa	*+7 hPa*

Figure 28 shows precision of retrieved aerosol pressure and optical thickness as a function of the *a priori* error in the surface pressure p_s for an aerosol layer with optical thickness of 0.5. The aerosol layer was at 500 or 800 hPa and over sea / ocean or vegetated land. We find that retrieval precision for these two parameters deteriorates somewhat if the *a priori* error is increased from 0 hPa (surface pressure not fitted) up to 3 hPa (surface pressure fitted). This deterioration of precision of retrieved pressure may be acceptable. However, we also find that the pressure biases in Table 16 are only partly removed when fitting surface pressure with an *a priori* error of 3 hPa (not shown). This indicates that the cost function is quite flat along the dimension of surface pressure.

7.9.3 Conclusion

Expected uncertainties in the temperature profile and surface pressure can cause significant biases in retrieved aerosol pressure. Biases due to temperature uncertainties can be avoided by fitting the temperature profile with an appropriate *a priori* error. Biases due to surface pressure uncertainties can be partly removed by fitting the surface pressure with an appropriate *a priori* error. We therefore implement fitting of the temperature profile and surface pressure as options to the baseline algorithm. Perhaps it is possible to fit the temperature profile only in the lower atmosphere or even to simply fit an offset to the *a priori* profile. Based on the sensitivity analysis, we expect ECMWF temperature profiles on a 1° by 1° grid to be sufficient for our purposes. As to surface pressure, we find that accurate *a priori* data is needed. Compared against Salstein et al. (2008) [43], our results indicate that ECMWF surface pressures should preferably be delivered on a spatial grid finer than 1° by 1°.

7.10 Aerosol pressure biases due to cloud contamination

Since retrieved aerosol pressure does not depend strongly on the assumed particle model (Section 7.6), the Aerosol Layer Height algorithm is in principle capable of retrieving the height of any scattering layer—aerosols or clouds. However, since the spectrum provides little profile information, we do not consider multi-layered aerosol / cloud profiles in our forward model. Pixels are screened for the presence of clouds (Section 5.1) and we assume in retrieval that remaining scenes are fully cloud-free and dominated by a single aerosol layer (cf. the profile parameterizations for retrieval shown in Figure 9). However, residual clouds may still be present in the target pixel after having applied a cloud mask.

In this section, we illustrate biases in retrieved aerosol pressure for two typical cases of cloud contamination: an optically thin, homogeneous cirrus cloud and a low-altitude broken cumulus cloud. We show that expected biases for cloud-contaminated scenes put strict requirements on cloud masking, which are probably difficult to meet by the TROPOMI cloud masks. It is therefore necessary to devise post-retrieval tests to further remove retrievals likely affected by cloud contamination (e.g. analysis of χ^2 or residue spectrum).

Approach

We investigate the sensitivity of retrieved aerosol pressure to the presence of a cloud layer that is not accounted for in the forward model for retrieval. In addition to the aerosol layer, the atmospheric scenarios contain either a cirrus layer between 330 and 300 hPa with cloud fraction of 1.0 for which we vary cloud optical thickness, or a cumulus cloud between 910 and 890 hPa with optical thickness of 10 for which we vary the cloud fraction. The state vector includes the main fit parameters p_{mid}, τ_0, A_s (758 nm) and A_s (770 nm).

Results

We simulated reflectance spectra for a number of aerosol optical thicknesses (0.2, 0.5 and 1.0), aerosol mid pressures (800, 700 and 600 hPa) and surface albedos (sea / ocean and vegetated land). We only show results for the aerosol layer at 700 hPa over sea / ocean, which are representative of results for all the other scenarios tested. Cirrus and cumulus cloud particles have a single scattering albedo of 1.0 and a Henyey-Greenstein phase function with asymmetry parameter of 0.8. The fit parameters' *a priori* values are equal to their true values; *a priori* errors for aerosol pressure, optical thickness and surface albedo are the usual 500 hPa, 2.0 and 0.20, respectively. The solar zenith angle is 50° and the viewing direction is nadir.

Figure 29 shows retrieved aerosol pressures for the aerosol layer at 700 hPa over sea / ocean as a function of cirrus optical thickness (left plot) and cumulus cloud fraction (right plot). Retrieved aerosol pressures are biased towards cloud pressures and sometimes retrieval does not even converge. We find larger biases and more non-convergent retrievals for optically thinner aerosol layers and larger separations between cloud layer and aerosol layer. The surface albedo has no pronounced effect on retrieval biases or lack of convergence due to cloud contamination (not shown).

Focusing on the aerosol layer with optical thickness of 0.5, we see that aerosol pressure biases become larger than 100 hPa if the cirrus optical thickness rises above 0.1. We expect that a cirrus optical thickness of 0.1 will be below the detection limit of the VIIRS cloud mask [1]. For the same aerosol layer, aerosol pressure biases become larger than 50 hPa if the cumulus cloud fraction rises above 0.2. Thus, some of the clouds that will typically pass a cloud mask can cause substantial biases in retrieved aerosol pressure.

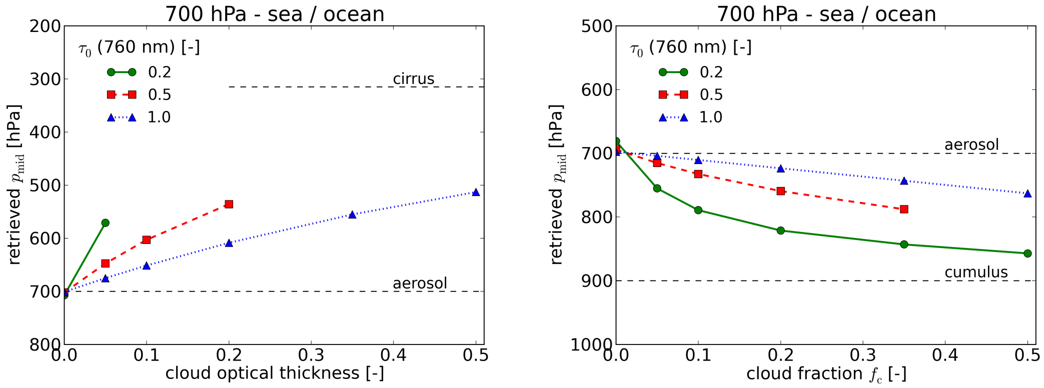

Figure 29: Effect of an unscreened cloud layer on retrieved aerosol pressure for three values of the aerosol optical thickness. Left: cirrus layer between 330 and 300 hPa with cloud fraction 1.0 and varying cloud optical thicknesses; right: cumulus cloud between 910 and 890 hPa with cloud optical thickness of 10 and varying cloud fractions. The aerosol layer is at 700 hPa over sea / ocean. The profile parameterization in retrieval assumes one scattering layer. Missing data points indicate that retrieval does not converge.

7.11 Alternative profile parameterization: aerosol layer with variable pressure thickness

The baseline algorithm assumes a single aerosol layer with a fixed pressure difference between top and bottom of the layer. We also implement alternative profile parameterizations as options to the baseline algorithm. These parameterizations are discussed in Section 5.2.4.6 and illustrated in Figure 9. The purpose of this section is to investigate precision if both mid pressure and pressure thickness are retrieved (Figure 9B). Precision of retrieved top pressure for the boundary layer pollution profile parameterization (Figure 9C) is illustrated in Section 7.6.2.

We compare precision of retrieved mid pressure p_{mid} and pressure thickness Δp for the alternative implementation with precision of retrieved mid pressure p_{mid} for the baseline algorithm. The state vector for the alternative implementation thus contains an additional profile parameter. We also investigate the dependence of precision on the *a priori* error in the surface albedo. The results show that if pressure thickness is included in the fit, precision of retrieved mid pressure hardly deteriorates. We also find that mid pressure is much easier to determine from the measurement than pressure thickness.

Approach

The current implementation of the algorithm with DISAMAR fits top pressure and bottom pressure. For a proper comparison of the alternative profile parameterization with the baseline parameterization, we report errors in mid pressure and pressure thickness, which are calculated from errors in top and bottom pressure. The state vector then basically contains fit parameters p_{mid}, τ_0, A_s (758 nm) and A_s (770 nm) with Δp being added for the alternative implementation.

Results

We simulated reflectance spectra for a number of aerosol optical thicknesses (0.2, 0.5 and 1.0), aerosol mid pressures (800 and 500 hPa) and surface albedos (sea / ocean and vegetated land). We assume a somewhat more realistic pressure thickness of 100 hPa in simulation and retrieval, because the spectral shape of derivatives for mid pressure and pressure thickness can also depend on this parameter.

We show results for two scenarios, which form the extremes between which the results for all other scenarios are. The *a priori* error in the surface albedo is varied between 0.001 and 1.0; *a priori* errors for mid pressure and pressure thickness are 354 hPa and 707 hPa, respectively (errors of 500 hPa for fit parameters top and bottom pressure); and the *a priori* error for aerosol optical thickness is 2.0. The solar zenith angle is 50° and the viewing direction is nadir.

Figure 30 shows precision of retrieved mid pressure and pressure thickness as a function of the *a priori* error in the surface albedo for an aerosol layer with optical thickness of 0.5 at 500 hPa over vegetated land and an aerosol layer with optical thickness of 0.5 at 800 hPa over sea / ocean. The green solid line represents results for the baseline algorithm; red dashed lines indicate results for the alternative profile parameterization.

If pressure thickness is also fitted, the deterioration of precision of retrieved mid pressure is limited and for

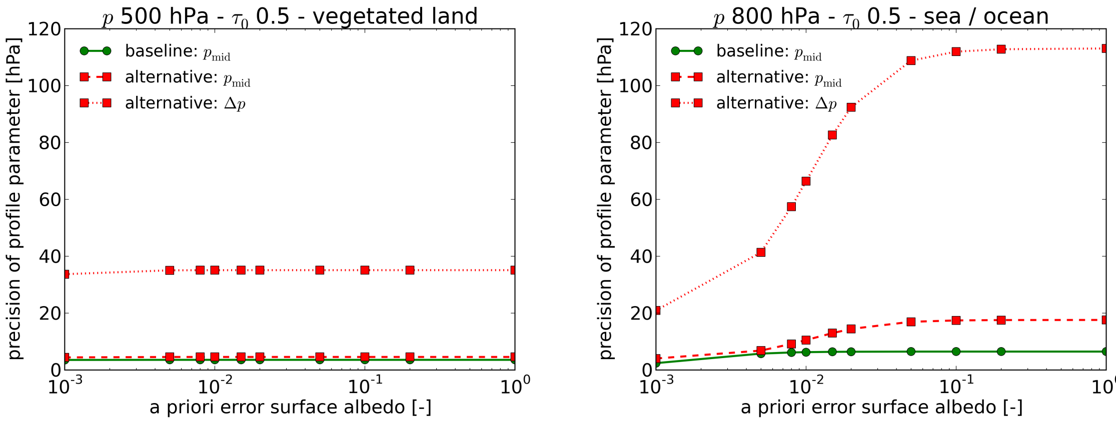

Figure 30: Precision of retrieved profile parameters as a function of the *a priori* error in the surface albedo for the baseline profile parameterization of a layer with fixed pressure thickness and the alternative implementation of a layer with variable pressure thickness. Left: aerosol layer with optical thickness of 0.5 at 500 hPa over vegetated land; right: aerosol layer with optical thickness of 0.5 at 800 hPa over sea / ocean. The baseline algorithm fits mid pressure (green solid line) and the alternative implementation fits mid pressure and pressure thickness (red dashed lines). Note the logarithmic scale of the x-axis.

many scenarios precision of retrieved mid pressure even is the same. Errors in mid pressure and pressure thickness are thus not highly correlated and in this respect it is a viable option to include pressure thickness in the state vector. However, we also see that precision of retrieved pressure thickness is much poorer than precision of retrieved mid pressure, although for some scenarios precision of pressure thickness may still be acceptable (e.g. below 50 hPa).

Over the range of *a priori* errors in the surface albedo, the elevated layers at 500 hPa hardly show an improvement in precision of profile parameters. For the near-surface layer at 800 hPa, precision of pressure thickness starts improving if the *a priori* error becomes smaller than 0.01 to 0.03. Here, accurate *a priori* knowledge of the surface albedo may in principle benefit retrieval, although we do not expect available *a priori* knowledge to be more accurate than this threshold.

7.12 Interference of chlorophyll fluorescence

Terrestrial vegetation exhibits fluorescence in the red and near-infrared wavelength range, which may thus interfere with aerosol retrieval from the O_2 A band. The purpose of this section is to briefly illustrate the effect of chlorophyll fluorescence on aerosol retrieval from the O_2 A band and to show that fluorescence and aerosol parameters can be retrieved simultaneously. A detailed discussion of aerosol retrieval from the O_2 A band in the presence of chlorophyll fluorescence can be found in Sanders and De Haan (2013) [44].

Approach

For an aerosol layer over vegetated land with typical fluorescence emissions, we compare accuracy and precision of retrieved aerosol pressure when fitting fluorescence emissions with accuracy and precision when not fitting emissions. We assume an average fluorescence emission at the O_2 A band of $1.0 \cdot 10^{12}$ photons s^{-1} cm^{-2} sr^{-1} nm^{-1}; as a maximum value we take three times the average fluorescence emission. These values are in agreement with Joiner et al. (2011) [25], although somewhat large compared to Guanter et al. (2012) [18] and Frankenberg et al. (2011) [15]. The state vector contains parameters p_{mid}, τ_0, A_s (758 nm) and A_s (770 nm), while F_s (758 nm) and F_s (770 nm) are added if fluorescence is fitted.

Results

We have simulated retrieval of aerosol layers at a number of different pressures over vegetated land with varying optical thickness. We report results for an aerosol layer at 600 hPa. True values, *a priori* values and *a priori* errors can be found in Table 17. The solar zenith angle is 50° and the viewing direction is nadir.

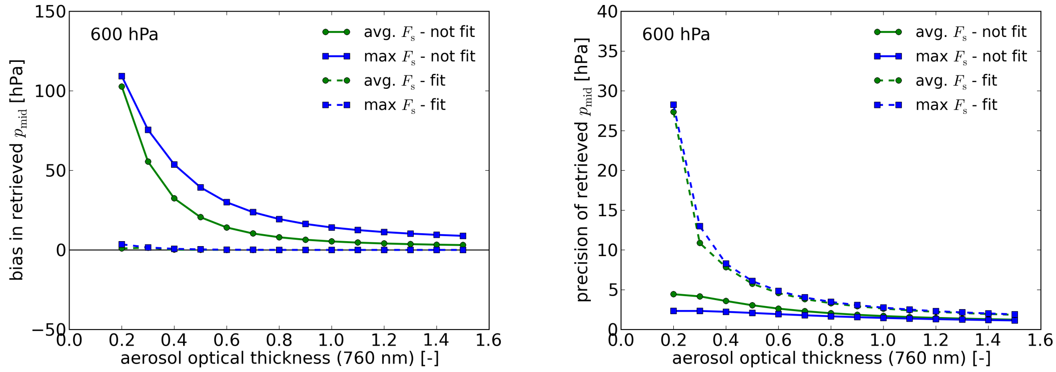

Figure 31: Accuracy (left plot) and precision (right plot) of retrieved aerosol pressure as a function of optical thickness when the vegetated land surface exhibits chlorophyll fluorescence. Solid lines correspond to a retrieval in which fluorescence is present in the simulation but not accounted for in the forward model for retrieval. Dashed lines correspond to a retrieval in which fluorescence emissions are included in the forward model and retrieved simultaneously with aerosol parameters.

Table 17: True values, *a priori* values and *a priori* errors used in the retrieval simulations of Figure 21 investigating the sensitivity of retrieval to the assumed single scattering albedo.

Fit parameter	True value	AP value	AP error (1-σ)
p_{mid}	600 hPa	True	500 hPa
τ_0 (760 nm)	Range: 0.2 – 1.5	True	2.0
A_s (758 nm) – A_s (770 nm)	0.20 – 0.25 (vegetated land)	True	0.2
A_s (758 nm) – A_s (770 nm)	$1.0 \cdot 10^{12}$ – $1.0 \cdot 10^{12}$ 'avg. F_s' $3.0 \cdot 10^{12}$ – $3.0 \cdot 10^{12}$ 'max F_s' photons s^{-1} $cm^{-2}sr^{-1}$ nm^{-1}	0.0–0.0	$1.0 \cdot 10^{12}$ – $1.0 \cdot 10^{12}$ photons s^{-1} $cm^{-2}sr^{-1}$ nm^{-1}

Figure 31 compares accuracy (left plot) and precision (right plot) of retrieved aerosol pressure when fluorescence emissions are fitted and when they are not. We assume fluorescence emissions to be absent a priori. If fluorescence emissions are ignored in the forward model, significant pressure biases occur, particularly for optically thinner layers. If the aerosol layer is placed lower in the atmosphere, we also find that retrieval often does not converge. Hence it is important to take fluorescence emissions into account in retrieval.

When fitting fluorescence emissions, retrievals converge and pressure biases disappear. For small aerosol optical thicknesses, precision of retrieved aerosol pressure deteriorates to some extent. There is of course a trade-off between accuracy and precision. Preliminary tests indicate that retrieval is stable when fitting fluorescence parameters. Even when *a priori* values differ strongly from true values, the true state is retrieved.

One may consider a fast fluorescence retrieval using Fraunhofer lines in a pre-processing step for the actual aerosol height retrieval (cf. [4]). Fluorescence emissions from the Fraunhofer line retrieval may then provide a constraint for the O_2 A band algorithm. However, an a priori fluorescence emission from such a pre-retrieval step also has an associated error (e.g. [4]). Sanders and De Haan (2013) [47] have investigated the dependence of retrieval precision on the a priori error in the fluorescence emission. For the cases considered, they find that precision of retrieved aerosol parameters hardly improves if the *a priori* error is decreased towards values that can typically be associated with a Fraunhofer line retrieval. This then indicates that if the objective of the O_2 A band retrieval is the retrieval of aerosol parameters, precision will hardly benefit from such a pre-retrieval step. Providing a better a priori value in the sense of a starting value for the fit might still help to improve the convergence rate or convergence to the global χ^2-minimum in case of a strongly non-linear forward model. This needs to be further investigated.

7.13 Instrumental errors

In this section we investigate the effect of instrumental errors on retrieval. Instrumental errors most relevant to the ALH algorithm are errors related to the Level-1b stray light correction, wavelength calibration and slit function calibration. We show that biases in retrieved pressure for typical instrument errors can be significant, depending on the scenario.

7.13.1 Stray light

Approach Part of the Level-1b processor is a stray light correction algorithm, which corrects the output of the detector for the stray light signal [RD17]. This correction step will very likely not remove the full stray light signal under all conditions. Here we investigate the effect of uncorrected stray light on retrieval. Since optical paths for the radiance and irradiance are almost identical, we assume the same amount of stray light as a fraction of the respective continuum signal. Stray light is modeled as a spectrally constant additive offset to the radiance and irradiance spectrum. Offsets are defined as percentages of the continuum (ir)radiance at 758 nm. Note that the relative stray light contribution is much larger inside the absorption band. We investigate offsets of 1%, 3% and 5%. The state vector contains fit parameters p_{mid}, τ_0, A_s (758 nm) and A_s (770 nm).

Results We simulated retrievals for an aerosol layer with optical thickness of 0.5 at 700 hPa over sea / ocean and vegetated land); *a priori* errors are the usual 500 hPa, 2.0 and 0.20, respectively. The solar zenith angle is 50° and the viewing direction is nadir.

Table 18 gives pressure biases and optical thicknesses in case of stray light offsets. Within precision margins of retrieved aerosol pressure, pressure biases scale linearly with offsets. For this scenario, a stray light offset of 1% gives a pressure bias of 6 hPa (sea / ocean) or 13 hPa (vegetated land).

Stray light for the radiance is expected to have the largest impact on retrieval, as the contribution is relatively large at strong absorption lines of the O_2 A band. Stray light for the earth radiance can in principle be fitted, but an instrument stray light model is needed in that case. Note that the stray light signal can be strongly dependent on wavelength.

Table 18: Pressure biases and retrieved optical thicknesses in case of additive offsets applied to the radiance and irradiance spectrum. The aerosol layer has an optical thickness of 0.5 and is at 700 hPa over sea / ocean or vegetated land. Stray light offsets are constant with wavelength and they are defined as percentages of the (ir)radiance at 758 nm.

Surface albedo: $\mathbf{A_s}$ (758 nm) – $\mathbf{A_s}$ (770 nm)	**Stray light offset**	**Pressure bias: retrieved - true**	**Pressure precision**	**Retrieved optical thickness**
0.025 – 0.025 (sea/ocean)	+1%	*-6 hPa*	3.9 hPa	0.49
	+3%	*-17 hPa*	3.9 hPa	0.48
	+5%	*-28 hPa*	3.8 hPa	0.47
0.20 – 0.25 (vegetated land)	+1%	*-13 hPa*	5.1 hPa	0.49
	+3%	*-37 hPa*	5.2 hPa	0.48
	+5%	*-61 hPa*	5.2 hPa	0.47

7.13.2 Wavelength calibration

Approach
A wavelength calibration of the solar irradiance measurement is foreseen in the Level-1b processor. The radiance measurement, however, is only assigned a nominal wavelength grid [RD17]. The reason for this is that inhomogeneous illumination of the slit (e.g. partly cloudy scenes) causes the most significant changes to the radiance wavelength scale. An accurate wavelength calibration of the radiance measurement should thus be part of the Level-2 processor, as inhomogeneous slit illumination is an atmospheric effect. Note, however, that inhomogeneous illumination of the slit is not expected for the Aerosol Layer Height algorithm, since the focus of this algorithm are cloud-free scenes

Here we investigate the effect of an error in the nominal wavelength grid for the radiance. The nominal radiance wavelength grid is shifted by 0.005 nm, 0.01 nm and 0.02 nm with respect to the true grid. We remark that the spectral bin size is 0.10 nm, so that a wavelength shift of 0.01 nm or 10% is already quite large. The state vector contains fit parameters p_{mid}, τ_0, A_s (758 nm) and A_s (770 nm).

Results
We simulated retrievals for an aerosol layer with optical thickness of 0.5 at 700 hPa over sea / ocean and vegetated land); *a priori* errors are the usual 500 hPa, 2.0 and 0.20, respectively. The solar zenith angle is 50° and the viewing direction is nadir.

Table 19 gives pressure biases and optical thicknesses in case of wavelength shifts applied to the nominal radiance wavelength grid. Within precision margins of retrieved aerosol pressure, pressure biases scale linearly with offsets. For this scenario, a wavelength shift of 0.005 nm gives a pressure bias of 3 hPa (sea / ocean) or 11 hPa (vegetated land).

Table 19: Pressure biases and retrieved optical thicknesses in case the width of the radiance and irradiance slit functions in the simulation differs from the width of the slit functions assumed in the retrieval. The aerosol layer has an optical thickness of 0.5 and is at 700 hPa over sea / ocean or vegetated land. The FWHM of the radiance and irradiance slit functions in retrieval is 0.5 nm.

Surface albedo: A_s (758 nm) – A_s (770 nm)	**FWHM slit functions in the simulation**	**Pressure bias: retrieved - true**	**Pressure precision**	**Retrieved optical thickness**
0.025 – 0.025 (sea/ocean)	0.51 nm	*-1 hPa*	3.9 hPa	0.50
	0.52 nm	*-2 hPa*	3.8 hPa	0.50
	0.54 nm	*-6 hPa*	3.8 hPa	0.50
0.20 – 0.25 (vegetated land)	0.51 nm	*+3 hPa*	4.9 hPa	0.51
	0.52 nm	*+5 hPa*	4.7 hPa	0.53
	0.54 nm	*+5 hPa*	4.5 hPa	0.55

It is possible to fit the width of the slit function as well as its nominal wavelength (see previous section) in the main algorithm. As an alternative, we may also consider performing the wavelength calibration in a pre-processing step, if this is accurate enough. Removing the wavelength shift from the state vector when performing online radiative transfer calculations will probably increase computation speed.

8 Validation

First validation efforts by Sentinel-5 Precursor (S5p) Mission Performance Centre (MPC) Cal/Val experts and the S5p Validation Team (S5PVT) show that the ALH is stable and shows good overall agreement with Caliop retrievals, with Caliop generally retrieving higher ALH than TROPOMI for ocean scenes. An early example of TROPOMI - Caliop comparison is shown in Fig 32. A statistical pixel-by-pixel comparison of Caliop and S5P layer height retrievals from three desert dust cases and one smoke plume showed good correlation between the retrievals (regression slope 1.00), but on average Caliop retrievals were 0.53 km higher in altitude than S5P ALH [36]. This is likely due to the different sensitivity, which for Caliop is to the top of the plume, while S5P is sensitive to the centroid of the layer altitude. This was confirmed by a study which compared smoke plumes heights over Canada from S5P and those retrieved by Caliop and MISR [17]. The latter uses stereoscopic viewing to retrieve plume top height. The systematic difference between S5P TROPOMI ALH and MISR aerosol plume height is about 600 m. This is again due to differences in the sensitivity of the instruments and the differences in the algorithms (centroid vs. top retrieval).

Over land, TROPOMI ALH becomes unreliable for increasing surface albedo. Consequently, the difference

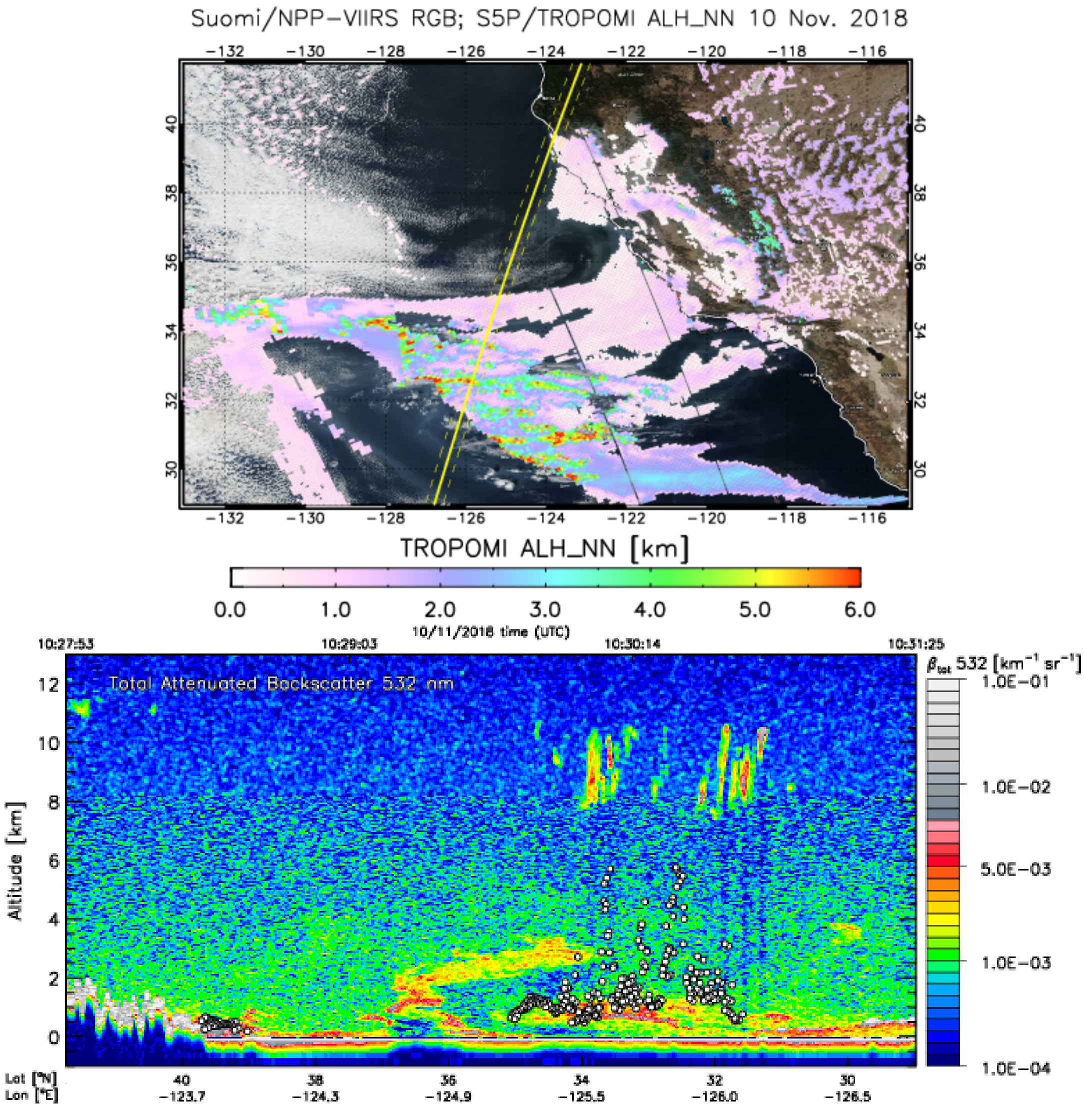

Figure 32: (top) Suomi/NPP VIIRS RGB on 10 Nov. 2018, overlaid with NN ALH. The yellow line depicts the CALIPSO track overpassing that day. The yellow dashed line depict the 20 km range around the CALIPSO track; (bottom) CALIOP Total attenuated backscatter at 532 nm on 10 Nov. 2018 for the track shown by the yellow line in the top panel.

between the plume height observed by TROPOMI and CALIOP depends significantly on the thickness of the plume. Thicker plumes seem to be better captured by TROPOMI and the mean difference reduces with the thickness of the plumes, the mean difference between the TROPOMI and CALIOP mid aerosol layer is just 50 m for very thick plumes (>3 km). The main reason is the insensitivity to the surface bias for thick plume in S5P ALH.

Collocated measurements over selected ground-based lidar sites have confirmed the above analyses. Existing lidar research networks such as the European Aerosol Research Lidar Network (EARLINET) or the GAW Atmospheric Lidar Observation Network (GALION) are available for validation stiudies. E.g. the summer campaign of the PANACEA project was carried out in June and August 2019 in Greece, providing first validations of the TROPOMI ALH with ground-based lidar [35]. The latest ground-based validation was performed over Greece in summer 2023 [34].

These above-mentioned studies and up to date validation results are available in the Routine Operations Consolidated Validation Reports (ROCVR) [RD18] that are accessible through the MPC Validation Data Analysis Facility (VDAF) website [RD19]. The ROCVR reports are issued quarterly and contain the latest validation results.

9 Conclusion and outlook

This Algorithm Theoretical Baseline Document describes the TROPOMI Aerosol Layer Height algorithm and product. The ATBD summarizes the current status and implementation of the algorithm. The forward model, including the atmospheric model and radiative transfer model, as well as the retrieval method and the current state vector composition are described. In addition, validation results and an error analysis illustrate the performance of the current implementation of the algorithm.

The algorithm fits the spectral reflectance at the O_2 A band near 760 nm. The current fit parameters are aerosol layer pressure, aerosol optical thickness and surface albedo. The algorithm assumes that aerosols are uniformly distributed in a single layer with a fixed geometric thickness and a constant aerosol volume extinction coefficient and aerosol single scattering albedo. The reported aerosol layer height is the mid pressure of the layer, additionally reported as the mid height of the layer, converted using a pressure-height profile. Aerosol cases for which this profile parameterization is particularly suited are boundary layer aerosols like sea salt and industrial pollution, and free-tropospheric aerosols such as volcanic ash, desert dust and biomass burning aerosols.

The first verification and validation efforts shows an ALH that was within the requirements over ocean, but not over land. Therefore, the surface albedo is now fitted routinely in the algorithm, showing large improvements over both land and ocean in the test cases. The coming period shall be used to investigate the robustness of this change.

The sensitivity analysis shows that when assuming a perfect forward model, precision of retrieved aerosol mid pressure in both ocean and land scenes is usually well below the target requirement of 50 hPa for optical thicknesses at 760 nm above 0.2. Retrieved aerosol pressure is robust to a model error in the single scattering albedo. The results suggest that retrieved pressure is also robust to a model error in the phase function, particularly over darker surfaces. Retrieved aerosol optical thickness however deviates from its true value and should be understood in this respect as an effective quantity. Fitting the surface albedo helps to compensate for model errors in aerosol optical properties.

The TROPOMI Aerosol Layer Height product has a number of important applications, notably for aviation safety purposes in near real-time, but also for a range of scientific research themes. The same retrieval technique can be used for the Sentinel-4 and Sentinel-5 missions. Further development of the algorithm is ongoing at KNMI.

10 References

[1] S. A. Ackerman, R. E. Holz, R. Frey, E. W. Eloranta, B. C. Maddux, and M. McGill. Cloud detection with modis. part ii: Validation. *Journal of Atmospheric and Oceanic Technology*, 25(7):1073–1086, 2008.

[2] VV Badayev and MS Malkevich. On the possibility of retrieval of aerosol extinction vertical profile using the satellite observation of reflected radiation in the oxygen band 760 nm. *Proc. Acad. Sci. USSR Sec. Atmos. Oceanic Phys*, 14:10221030, 1978.

[3] H. Bovensmann, J. P. Burrows, M. Buchwitz, J. Frerick, S. Noël, V. V. Rozanov, K. V. Chance, and A. P. H Goede. SCIAMACHY: Mission Objectives and Measurement Modes. *J. Atmos. Sci.*, 56(2):127–150, 1999.

[4] M. Buchwitz, M. Reuter, H. Bovensmann, D. Pillai, J. Heymann, O. Schneising, V. Rozanov, T. Krings, J. P. Burrows, H. Boesch, C. Gerbig, Y. Meijer, and A. Löscher. Carbon monitoring satellite (carbonsat): assessment of atmospheric co_2 and ch_4 retrieval errors by error parameterization. *Atmospheric Measurement Techniques*, 6(12):3477–3500, 2013.

[5] A. Butz, A. Galli, O. Hasekamp, J. Landgraf, P. Tol, and I. Aben. Tropomi aboard sentinel-5 precursor: Prospective performance of ch4 retrievals for aerosol and cirrus loaded atmospheres. *Remote Sensing of Environment*, 120:267 – 276, 2012. The Sentinel Missions - New Opportunities for Science.

[6] T. R. Caudill, D. E. Flittner, B. M. Herman, O. Torres, and R. D. McPeters. Evaluation of the pseudo-spherical approximation for backscattered ultraviolet radiances and ozone retrieval. *Journal of Geophysical Research: Atmospheres*, 102(D3):3881–3890, 1997.

[7] Xi Chen, Jun Wang, Xiaoguang Xu, Meng Zhou, Huanxin Zhang, Lorena Castro Garcia, Peter R. Colarco, Scott J. Janz, John Yorks, Matthew McGill, Jeffrey S. Reid, Martin de Graaf, and Shobha Kondragunta. First retrieval of absorbing aerosol height over dark target using tropomi oxygen b band: Algorithm development and application for surface particulate matter estimates. *Remote Sensing of Environment*, 265:112674, 2021.

[8] Stefano Corradini and Marco Cervino. Aerosol extinction coefficient profile retrieval in the oxygen a-band considering multiple scattering atmosphere. test case: Sciamachy nadir simulated measurements. *Journal of Quantitative Spectroscopy and Radiative Transfer*, 97(3):354 – 380, 2006.

[9] J. S. Daniel, S. Solomon, H. L. Miller, A. O. Langford, R. W. Portmann, and C. S. Eubank. Retrieving cloud information from passive measurements of solar radiation absorbed by molecular oxygen and o2-o2. *Journal of Geophysical Research: Atmospheres*, 108(D16), 2003.

[10] J.J. Danielson and D.B. Gesch. Global multi-resolution terrain elevation data 2010 (gmted2010), 2011.

[11] JF De Haan, PB Bosma, and JW Hovenier. The adding method for multiple scattering calculations of polarized light. *Astronomy and Astrophysics*, 183:371–391, 1987.

[12] Gerrit de Leeuw, Thomas Holzer-Popp, Suzanne Bevan, William H. Davies, Jacques Descloitres, Roy G. Grainger, Jan Griesfeller, Andreas Heckel, Stefan Kinne, Lars Klüser, Pekka Kolmonen, Pavel Litvinov, Dmytro Martynenko, Peter North, Bertrand Ovigneur, Nicolas Pascal, Caroline Poulsen, Didier Ramon, Michael Schulz, Richard Siddans, Larisa Sogacheva, Didier Tanré, Gareth E. Thomas, Timo H. Virtanen, Wolfgang von Hoyningen Huene, Marco Vountas, and Simon Pinnock. Evaluation of seven european aerosol optical depth retrieval algorithms for climate analysis. *Remote Sensing of Environment*, 162:295 – 315, 2015.

[13] Oleg Dubovik, Brent Holben, Thomas F Eck, Alexander Smirnov, Yoram J Kaufman, Michael D King, Didier Tanré, and Ilya Slutsker. Variability of absorption and optical properties of key aerosol types observed in worldwide locations. *Journal of the atmospheric sciences*, 59(3):590–608, 2002.

[14] Philippe Dubuisson, Robert Frouin, David Dessailly, Lucile Duforêt, Jean Francois Léon, Kenneth Voss, and David Antoine. Estimating the altitude of aerosol plumes over the ocean from reflectance ratio measurements in the o2 a-band. *Remote Sensing of Environment*, 113(9):1899–1911, 9 2009.

[15] Christian Frankenberg, Joshua B. Fisher, John Worden, Grayson Badgley, Sassan S. Saatchi, Jung-Eun Lee, Geoffrey C. Toon, André Butz, Martin Jung, Akihiko Kuze, and Tatsuya Yokota. New global observations of the terrestrial carbon cycle from gosat: Patterns of plant fluorescence with gross primary productivity. *Geophysical Research Letters*, 38(17), 2011.

[16] Marco Gabella, Vlatcheslav Kisselev, and Giovanni Perona. Retrieval of aerosol profile variations from reflected radiation in the oxygen absorption a band. *Applied optics*, 38(15):3190–3195, 1999.

[17] D. Griffin, C. Sioris, J. Chen, N. Dickson, A. Kovachik, M. de Graaf, S. Nanda, J. P. Veefkind, E. Dammers, C. A. McLinden, and P. Maker. The 2018 fire season in north america as seen by tropomi: aerosol layer height validation and evaluation of model-derived plume heights. *Atmos. Chem. Phys.*, 19, 2019.

[18] Luis Guanter, Christian Frankenberg, Anu Dudhia, Philip E. Lewis, Jos'E g'Omez Dans, Akihiko Kuze, Hiroshi Suto, and Roy G. Grainger. Retrieval and global assessment of terrestrial chlorophyll fluorescence from gosat space measurements. *Remote Sensing of Environment*, 121:236 – 251, 2012.

[19] O. Hasekamp and R. Siddans. Chapter 8: Aerosols. in: Camelot task 3 report – retrieval simulations, j.p. veefkind (ed.). *RP-CAM-KNMI-033, issue 1*, 30 November 2009.

[20] Otto Hasekamp, Andre Galli, Haili Hu, Paul Tol, Jochen Landgraf, and Andre Butz. Algorithm theoretical baseline document for sentinel-5 precursor methane retrieval. Technical report, SRON, 2015.

[21] A. Hollstein, R. Lindstrot, and J. Fischer. Retrieval of aerosol vertical profile from top of atmosphere and high spectral resolution radiance measurements in the o2 a band. *Technical note within the ESA project FLUSS.*, 2012.

[22] Joop W Hovenier, Cornelis VM van der Mee, and Helmut Domke. *Transfer of polarized light in planetary atmospheres: basic concepts and practical methods*, volume 318. Springer Science & Business Media, 2014.

[23] Paul Ingmann, Ben Veihelmann, Jörg Langen, Daniel Lamarre, Hendrik Stark, and Grégory Bazalgette Courrèges-Lacoste. Requirements for the gmes atmosphere service and esa's implementation concept: Sentinels-4/-5 and -5p. *Remote Sensing of Environment*, 120:58 – 69, 2012. The Sentinel Missions - New Opportunities for Science.

[24] L.K. Jänicke, R. Preusker, N. Docter, and J. Fischer.

[25] J. Joiner, Y. Yoshida, A. P. Vasilkov, Y. Yoshida, L. A. Corp, and E. M. Middleton. First observations of global and seasonal terrestrial chlorophyll fluorescence from space. *Biogeosciences*, 8(3):637–651, 2011.

[26] R. A. Kahn and J. Limbacher. Eyjafjallajökull volcano plume particle-type characterization from space-based multi-angle imaging. *Atmospheric Chemistry and Physics*, 12(20):9459–9477, 2012.

[27] Ralph A. Kahn, Yang Chen, David L. Nelson, Fok-Yan Leung, Qinbin Li, David J. Diner, and Jennifer A. Logan. Wildfire smoke injection heights: Two perspectives from space. *Geophysical Research Letters*, 35(4), 2008.

[28] R. B. A. Koelemeijer, P. Stammes, J. W. Hovenier, and J. F. de Haan. A fast method for retrieval of cloud parameters using oxygen A-band measurements from GOME. *J. Geophys. Res.*, 106(D04):3475–3490, 2001.

[29] RBA Koelemeijer, JF De Haan, and P Stammes. A database of spectral surface reflectivity in the range 335–772 nm derived from 5.5 years of gome observations. *Journal of Geophysical Research: Atmospheres*, 108(D2), 2003.

[30] Alexander A Kokhanovsky and Vladimir V Rozanov. The determination of dust cloud altitudes from a satellite using hyperspectral measurements in the gaseous absorption band. *International Journal of Remote Sensing*, 31(10):2729–2744, 2010.

[31] GAA Koppers, J Jansson, and DP Murtagh. Aerosol optical thickness retrieval from gome data in the oxygen a-band. *ESA SP*, pages 693–696, 1997.

[32] Jochen Landgraf, Otto P Hasekamp, Michael A Box, and Thomas Trautmann. A linearized radiative transfer model for ozone profile retrieval using the analytical forward-adjoint perturbation theory approach. *Journal of Geophysical Research. D. Atmospheres*, 106:27, 2001.

[33] L. Lelli, A. Kokhanovsky, V. Rozanov, M. Jaeger, and J. Burrows. Retrieval of aerosol layer height in the oxygen a-band: case studies using synthetic and multiple remote sensing data. *EGU General Assembly 27 April – 2 May 2014, EGU2014-4092-2*, 2014.

[34] K. michailidis, M.-E. Koukouli, D. Balis, J. P. Veefkind, M. de Graaf, L. Mona, N. Papagianopoulos, G. Pappalardo, I. Tsikoudi, V. Amiridis, E. Marinou, A. Gialitaki, R.-E. Mamouri, A. Nisantzi, D. Bortoli, M. João Costa, V. Salgueiro, A. Papayannis, M. Mylonaki, L. Alados-Arboledas, S. Romano, M. R. Perrone, and H. Baars. Validation of the tropomi/s5p aerosol layer height using earlinet lidars. *Atmospheric Chemistry and Physics*, 23(3):1919–1940, 2023.

[35] K. Michailidis, N. Siomos, D Balis, M. E. Koukouli, K. A Voudouri, O. Tuinder, G. Tilstra, P. Wang, M. de Graaf, and J. P. Veefkind. Validation of tropomi's/s5p and gome-2/metop aerosol height products using the elevated height obtained from thessaloniki lidar station during panacea campaign, 2019.

[36] S. Nanda, M. de Graaf, J. P. Veefkind, M. Sneep, M. ter Linden, J. Sun, and P. F. Levelt. Validating tropomi aerosol layer height retrievals with caliop data. *Atmos. Meas. Tech. Disc.*, 19(19), 2019.

[37] C. W. O'Dell, B. Connor, H. Bösch, D. O'Brien, C. Frankenberg, R. Castano, M. Christi, D. Eldering, B. Fisher, M. Gunson, J. McDuffie, C. E. Miller, V. Natraj, F. Oyafuso, I. Polonsky, M. Smyth, T. Taylor, G. C. Toon, P. O. Wennberg, and D. Wunch. The acos co_2 retrieval algorithm – part 1: Description and validation against synthetic observations. *Atmospheric Measurement Techniques*, 5(1):99–121, 2012.

[38] S. S. Park, J. Kim, Y. Cho, H. Lee, J. Park, D.-W. Lee, W.-J. Lee, and D.-R. Kim. Retrieval algorithm for aerosol effective height from the geostationary environment monitoring spectrometer (gems). *Atmospheric Measurement Techniques Discussions*, 2023:1–40, 2023.

[39] C. Popp, P. Wang, D. Brunner, P. Stammes, Y. Zhou, and M. Grzegorski. Meris albedo climatology for fresco+ O_2 a-band cloud retrieval. *Atmos. Meas. Tech.*, 4:463–483, 2011.

[40] M. Reuter, M. Buchwitz, O. Schneising, J. Heymann, H. Bovensmann, and J. P. Burrows. A method for improved sciamachy co_2 retrieval in the presence of optically thin clouds. *Atmospheric Measurement Techniques*, 3(1):209–232, 2010.

[41] Clive D Rodgers. *Inverse methods for atmospheric sounding: theory and practice*, volume 2. World scientific, 2000.

[42] Vladimir V. Rozanov and Alexander A. Kokhanovsky. Semianalytical cloud retrieval algorithm as applied to the cloud top altitude and the cloud geometrical thickness determination from top-of-atmosphere reflectance measurements in the oxygen a band. *Journal of Geophysical Research: Atmospheres*, 109(D5), 2004.

[43] David A. Salstein, Rui M. Ponte, and Karen Cady-Pereira. Uncertainties in atmospheric surface pressure fields from global analyses. *Journal of Geophysical Research: Atmospheres*, 113(D14), 2008.

[44] A. F. J. Sanders and J. F. de Haan. Retrieval of aerosol parameters from the oxygen A band in the presence of chlorophyll fluorescence. *Atmospheric Measurement Techniques*, 6(10):2725–2740, October 2013.

[45] A. F. J. Sanders, J. F. de Haan, M. Sneep, A. Apituley, P. Stammes, M. O. Vieitez, L. G. Tilstra, O. N. E. Tuinder, C. E. Koning, and J. P. Veefkind. Evaluation of the operational aerosol layer height retrieval algorithm for sentinel-5 precursor: application to o_2 a band observations from gome-2a. *Atmospheric Measurement Techniques Discussions*, 8(6):6045–6118, 2015.

[46] AFJ Sanders, JF de Haan, M Sneep, A Apituley, P Stammes, MO Vieitez, LG Tilstra, CE Koning, and JP Veefkind. Evaluation of the operational aerosol layer height retrieval algorithm for sentinel-5 precursor: application to o 2 a band observations from gome-2a. *Atmospheric Measurement Techniques*, 8(11):4947–4977, 2015.

[47] A.F.J. Sanders, O. Vieitez, and P. Stammes. Aeropro technical note tn3: Theoretical baseline description of the aerosol profile retrieval algorithm concept. *ESA ITT AO/1-7017/11/NL/MP, version 1.0,*, 14 March 2013.

[48] S Sanghavi, JV Martonchik, J Landgraf, and U Platt. Retrieval of the optical depth and vertical distribution of particulate scatterers in the atmosphere using o 2 a-and b-band sciamachy observations over kanpur: a case study. *Atmospheric Measurement Techniques*, 5(5):1099–1119, 2012.

[49] R. Siddans, B.G. Latter, and B.J. Kerridge. Study to consolidate the uvs mission requirements for the oxygen a-band. *EUMETSAT Contract No. EUM/CO/05/1411/SAT, version 1.2*, 24 May 2007.

[50] Christopher E. Sioris and Wayne F. J. Evans. Impact of rotational raman scattering in the o2a band. *Geophysical Research Letters*, 27(24):4085–4088, 2000.

[51] Maarten Sneep. Analysis of the transistion to the small pixel operational settings on nrti data. Technical report, KNMI, 2019.

[52] L. G. Tilstra, M. de Graaf, V. Trees, P. Litvinov, O. Dubovik, and P. Stammes. A directional surface reflectance climatology determined from tropomi observations. *Atmos. Meas. Tech. Discuss.*, *submitted*, 2023.

[53] L. G. Tilstra, O. N. E. Tuinder, P. Wang, and P. Stammes. Surface reflectivity climatologies from uv to nir determined from earth observations by gome-2 and sciamachy. *Journal of Geophysical Research: Atmospheres*, 122(7):4084–4111, 2017.

[54] H. Tran, C. Boulet, and J.-M. Hartmann. Line mixing and collision-induced absorption by oxygen in the a band: Laboratory measurements, model, and tools for atmospheric spectra computations. *J. Geophys. Res.*, 111(D15), August 2006.

[55] H. Tran and J.-M. Hartmann. An improved O2 A band absorption model and its consequences for retrievals of photon paths and surface pressures. *J. Geophys. Res.*, 113(D18):D18104, September 2008.

[56] B. van Diedenhoven, O. P. Hasekamp, and I. Aben. Surface pressure retrieval from SCIAMACHY measurements in the O₂ A Band: validation of the measurements and sensitivity on aerosols. *Atmospheric Chemistry and Physics*, 5(8):2109–2120, August 2005.

[57] S. Vandenbussche, S. Kochenova, A. C. Vandaele, N. Kumps, and M. De Mazière. Retrieval of desert dust aerosol vertical profiles from iasi measurements in the tir atmospheric window. *Atmospheric Measurement Techniques*, 6(10):2577–2591, 2013.

[58] A. Vasilkov, J. Joiner, and R. Spurr. Note on rotational-raman scattering in the o_2 a- and b-bands. *Atmospheric Measurement Techniques*, 6(4):981–990, 2013.

[59] J. P. Veefkind, I. Aben, K. McMullan, H. Förster, J. de Vries, G. Otter, J. Claas, H. J. Eskes, J. F. de Haan, Q. Kleipool, M. van Weele, O. Hasekamp, R. Hoogeveen, J. Landgraf, R. Snel, P. Tol, P. Ingmann, R. Voors, B. Kruizinga, R. Vink, H. Visser, and P. F. Levelt. TROPOMI on the ESA Sentinel-5 Precursor: A GMES mission for global observations of the atmospheric composition for climate, air quality and ozone layer applications. *Remote Sensing of Environment*, 120:70–83, May 2012.

[60] P. Wang, O. N. E. Tuinder, L. G. Tilstra, M. de Graaf, and P. Stammes. Interpretation of FRESCO cloud retrievals in case of absorbing aerosol events. *Atm. Chem. Physics*, 12(19):9057–9077, 2012.

[61] Y. Yoshida, Y. Ota, N. Eguchi, N. Kikuchi, K. Nobuta, H. Tran, I. Morino, and T. Yokota. Retrieval algorithm for co_2 and ch_4 column abundances from short-wavelength infrared spectral observations by the greenhouse gases observing satellite. *Atmospheric Measurement Techniques*, 4(4):717–734, 2011.